
SpannEnD 2.0 – Stress model Germany

Further development of geomechanical-numerical modelling to characterize the tectonic stress state for the final disposal of radioactive waste in Germany

Interim Report 09/2023

Spannungsmodell Endlagerung Deutschland (SpannEnD 2.0), Zwischenbericht 09/2023, Weiterentwicklung geomechanisch-numerischer Modellierungen zur Charakterisierung des tektonischen Spannungszustandes für die Endlagerung radioaktiver Abfälle in Deutschland

Projektträger/project executing organisation : Bundesgesellschaft für Endlagerung (BGE)

Projektlaufzeit/project duration: 04/2022 – 03/2026

Förderkennzeichen/support code: FEWFuE-22-01-JS

Karsten Reiter¹

Luisa Röckel²

Sophia Morawietz^{3,4}

Steffen Ahlers¹

Victoria Kuznetsova¹

Moritz Ziegler^{3,5}

Tobias Hergert²

Andreas Henk¹ (Coordination)

Oliver Heidbach^{3,4}

Birgit Müller²

Frank Schilling²

¹ Institute of Applied Geosciences , Technische Universität Darmstadt, 64287 Darmstadt, Germany

² Institute of Applied Geosciences , Karlsruhe Institute of Technology, 76131 Karlsruhe, Germany

³ Helmholtz Centre Potsdam, GFZ German Research Centre for Geosciences, 14473 Potsdam, Germany

⁴ Institute of Applied Geosciences , Technical University of Berlin, 10587 Berlin, Germany

⁵ School of Engineering and Design, Technical University of Munich, 80333 Munich, Germany

November 20, 2023

Abstract

The project SpannEnD 2.0 is the follow-up project to the SpannEnD project, which was successfully completed in 2022. It was initiated to gain a better understanding of the spatial variability of the 3D stress field in the German crust. During the project, a stress magnitude database for Germany and surrounding regions was established and a geomechanical model of the region was created and calibrated against these magnitude data. In addition, the model results were transferred to a fault data set to estimate the reactivation potential of existing faults. Based on the results of the SpannEnD project, the SpannEnD 2.0 project will both continue and deepen these topics and add new focal points. The following is a brief overview of the individual topics covered to date.

Stress magnitudes database: The database collects stress magnitudes for Germany and neighbouring regions. Based on the first version with 568 data sets, 429 new data sets could be added, mainly from the greater Ruhr area. Currently, the latest data from northern Switzerland are being incorporated. This is a unique dataset that contains magnitudes of S_{hmin} as well as S_{Hmax} magnitudes. In addition, work is being done to integrate the magnitude database into the World Stress Map database.

Stress model Germany: The focus of the current work is on incorporating existing regional structural geological models to refine and correct the geometry. These more detailed models allow the use of significantly more lithological units. Thus, geomechanical material properties for up to 155 different lithologies are now considered.

Slip Tendency Analysis: Based on the geomechanical model of Germany, the failure potential on faults is investigated. For this purpose, a database of available fault geometries was created. Regions for which many fault geometries are available are analysed separately. This is the case for the North German Basin, the Ore Mountain region, the Upper Rhine Graben and the Molasse Basin. For regions without data, stereoplots are available to derive the failure potential for all orientations.

Sub-modelling technique: The test of transferring the stress state to smaller models with a higher numerical and lithological resolution shows that the model results strongly depend on the variability of the Young's modulus; results are over- or underestimated accordingly. An approach with generation of substitute calibration data in the larger-scale model for subsequent use in the smaller-scale model in identical lithological units proved to be the most suitable. The initial stress state used for geomechanical models affects the resulting stress state away from the location of calibration data, with more realistic results obtained when deep rather than near-surface stress magnitude data are used. Greater uncertainties are to be expected at material transitions.

Scale dependence of mechanical material parameters: Three different methods for upscaling mechanical parameters or for fitting to the model scale have been investigated so far: empirical correlation based on engineering geological rock mass classifications, Discrete Fracture Network (DFN) models and Synthetic Rock Mass (SRM) models. In particular, upscaling using the DFN approach is promising, as the method provides spatially varying, optionally isotropic or anisotropic values for the Young's modulus and the Poisson ratio for scale-dependent parameterisation of geomechanical models.

Model region sub-area 001: The Setup of the model for sub-area 001 Opalinus Clay is still in an early phase. To gain a better understanding of the subsidence history of the Opalinus Clay in the

region, a subsidence analysis was carried out.

Model region sub-area 009: Since sub-area 009 is very large, the Ore Mountains region was selected, from which a consistent structural geological model is available. A geomechanical model was created, which is significantly better discretised around the region next to the KTB well, as several stress data are available here for calibration.

Calibration tool FAST Calibration v2.0: Geomechanical models are calibrated against stress magnitude data. With the help of the FAST Calibration tool, the optimal displacement boundary conditions for the best-fit model can be determined based on only three test runs of the model. The extension of the tool also allows the calibration of multi-level sub-models.

Kurzfassung

Das Projekt SpannEnD 2.0 ist das Folgeprojekt des Projektes SpannEnD, welches 2022 erfolgreich abgeschlossen wurde. Dieses wurde initiiert, um ein besseres Verständnis der räumlichen Variabilität des 3D Spannungsfeldes in der Erdkruste Deutschlands zu erlangen. Im Zuge des Projektes wurde eine Spannungsmagnitudendatenbank für Deutschland und umgebende Regionen aufgebaut und ein geomechanisches Modell der Region erstellt, das an diesen Daten kalibriert wurde. Zusätzlich wurden zur Abschätzung des Reaktivierungspotentials existierender Störungen die Modellergebnisse auf Störungsdatensätze übertragen. Auf den Ergebnissen des SpannEnD Projektes aufbauend werden im Projekt SpannEnD 2.0 sowohl diese Themen fortgesetzt und vertieft als auch neue Schwerpunkte hinzugefügt. Im Folgenden wird ein kurzer Abriss der bisher durchgeführten Arbeiten gegeben.

Spannungsmagnituden-Datenbank: Die Datenbank sammelt Spannungsmagnituden für Deutschland und benachbarte Regionen. Aufbauend auf der ersten Version mit 568 Datensätzen konnten 429 neue Datensätze vor allem aus dem Großraum des Ruhrgebietes hinzugefügt werden. Derzeit werden neueste Daten aus der Nordschweiz eingearbeitet. Dabei handelt es sich um einen einmaligen Datensatz, der neben Magnituden von S_{hmin} auch S_{Hmax} Magnituden enthält. Zusätzlich wird an der Integration der Datenbank in die World Stress Map Datenbank gearbeitet.

Spannungsmodell Deutschland: Der Fokus der derzeitigen Arbeiten liegt auf der Einarbeitung existierender regionaler strukturgeologischer Modelle, um die Geometrie zu verfeinern und zu korrigieren. Diese detaillierteren Modelle erlauben es, deutlich mehr lithologische Einheiten zu verwenden. So werden nun geomechanische Materialeigenschaften für bis zu 155 unterschiedliche Lithologien berücksichtigt.

Slip Tendency Analyse: Basierend auf dem geomechanischen Modell von Deutschland wird das Versagenspotential an Störungen untersucht. Dafür wurde eine Datenbank der verfügbaren Störungsgeometrien erstellt. Regionen, für die viele Störungsgeometrien verfügbar sind, werden vertiefend separat analysiert. Dies ist der Fall für das Norddeutsche Becken, die Erzgebirgsregion, den Oberrheingraben und das Molassebecken. Für Regionen ohne Daten stehen Stereoplots zur Verfügung, um das Versagenspotential für alle Störungsorientierungen ableiten zu können.

Submodellierungstechnik: Der Test des Übertrags des Spannungszustandes auf kleinere Modelle mit einer höheren numerischen und lithologischen Auflösung zeigt, dass die Modellergebnisse stark von der Variabilität des E-Moduls abhängen; Ergebnisse werden entsprechend über- bzw. unterschätzt. Ein Ansatz mit Generierung von Ersatzkalibrierungsdaten im grossräumigeren Modell zur nachfolgenden Nutzung im kleinräumigeren Modell in identischen lithologischen Einheiten erwies sich als am geeignetsten. Der initiale Spannungszustand, der für geomechanische Modelle verwendet wird, wirkt sich auf den resultierenden Spannungszustand abseits der Lokation von Kalibrierungsdaten aus, wobei realistischere Ergebnisse erzielt werden, wenn tiefe statt oberflächennahe Spannungsmagnitudendaten Verwendung finden. Größere Unsicherheiten sind an Materialübergängen zu erwarten.

Skalenabhängigkeit von mechanischen Materialparametern: Drei verschiedene Verfahren zur Aufskalierung von mechanischen Parametern bzw. zur Anpassung an den Modellmaßstab wurden bislang untersucht: empirische Korrelation auf der Basis von ingenieurgeologischen Gebirgsklassifikationen, Discrete Fracture Network (DFN) Modelle und Synthetic Rock Mass (SRM) Modelle.

Insbesondere die Aufskalierung mittels des DFN-Ansatzes ist vielversprechend, da die Methode räumlich variierende, wahlweise isotrope oder anisotrope Werte für den Gebirgs-E-Modul und die Gebirgs-Querdehnungszahl zur skalenabhängigen Parametrisierung geomechanischer Modelle liefert.

Modellregion Teilgebiet 001: Die Erstellung des Modells für das Teilgebiet 001 Opalinuston ist noch in einer frühen Phase. Um ein besseres Verständnis der Versenkungsgeschichte des Opalinustons in der Region zu erlangen, wurde eine Subsidenzanalyse durchgeführt.

Modellregion Teilgebiet 009: Da das Teilgebiet 009 sehr groß ist, wurde die Erzgebirgsregion ausgewählt, von der ein konsistentes strukturgeologisches Modell zur Verfügung steht. Es wurde ein geomechanisches Modell erstellt, welches in der Region der Kontinentalen Tiefbohrung (KTB) deutlich besser diskretisiert ist, da hier mehrere Spannungsdaten für die Kalibrierung vorhanden sind.

Kalibrierungstool FAST Calibration v2.0: Geomechanische Modelle werden an Spannungsmagnitudendaten kalibriert. Mit Hilfe des Werkzeuges FAST Calibration können auf der Basis von nur drei Testläufen des Modells die optimalen Verschiebungsrandbedingungen für das Best-fit Modell ermittelt werden. Die Erweiterung des Werkzeuges ermöglicht auch das Kalibrieren von mehrstufigen Submodellen.

Contents

Abstract	i
Kurzfassung	iii
1 Introduction	1
2 Enhancements of the Germany stress model (AP1)	3
2.1 Determination of stress magnitudes and status of the stress data compilation Germany	3
2.1.1 Introduction	3
2.1.2 Loading methods to determine S_{hmin} and S_{Hmax} magnitudes	4
2.1.3 Relief Methods	12
2.1.4 Other Methods	15
2.1.5 Frictional Limit as Upper Bounds of Stress Magnitudes	15
2.1.6 Stress Information Database of Germany and Adjacent Regions	16
2.1.7 Abbreviations	18
2.2 Structural diversification of the geomechanical model for Germany	19
2.2.1 Introduction	19
2.2.2 Database	19
2.2.3 Technical implementation	22
2.2.4 Outlook	24
2.3 Slip Tendency Analysis	25
2.3.1 Material	25
2.3.2 Slip Tendency Calculation	27
2.3.3 Results and Discussion	28
3 Development of the submodelling workflow (AP2)	37
3.1 Development of submodelling techniques to link different model scales	37
3.1.1 Purpose and challenges of submodelling	37
3.1.2 Submodelling technique for consistent stress transfer between models	38
3.1.3 On the influence of initial stress on final stress in geomechanical models	40
3.1.4 Conclusions	44
3.2 Development of modelling techniques to adapt mechanical properties to the model scale	45
3.2.1 Rock mechanical parameters	45
3.2.2 Estimates based on rock mass classification schemes	45
3.2.3 Estimates from Discrete Fracture Network (DFN) models	46
3.2.4 Estimates based on Synthetic Rock Mass (SRM) models	50
3.2.5 Preliminary conclusions and next steps	51
3.3 Preparation of the geomechanical model sub-area 001	53
3.3.1 Extent of sub-area 001 and available data for modelling	53
3.3.2 Subsidence Analysis of the sub-area 001	55
3.4 Preparation of the geomechanical model for sub-area 009	59

4 Calibration data and exploration programmes (AP3)	65
4.1 Preparation of the tool FAST Calibration v2.0	65
Bibliography	69
List of Figures	IX
List of Tables	XI

1 Introduction

The acronym **SpannEnD** stands for **S**pannungsmodellierung **E**ndlagerung **D**eutschland and expresses that geomechanics must be considered for final disposal and thus the site search for a deep geological repository for high-level radioactive waste. Geomechanics, or the stress field, plays a role for various search criteria that directly or indirectly involve stability issues. This concerns, for example, the constructional feasibility, the hydraulic permeability of the host rock, the self-sealing capacity, the damage zone in the vicinity of the underground structures, the occurrence of earthquakes or the potential reactivation of faults as migration paths for fluids and radionuclides.

The first phase of the SpannEnD project, funded by the German Federal Ministry for Economic Affairs and Energy, lasted from 2018 to 2022, during which basic work was carried out (Reiter et al., 2022). This can be continued in the current phase, SpannEnD 2.0. The most important milestones of SpannEnD were the creation of the first database of stress magnitudes from Germany and the surrounding area (Morawietz et al., 2020), the first geomechanical model covering the whole of Germany (Ahlers et al., 2021, 2022), and the first large-scale analysis of slip tendency (Röckel et al., 2022), based on the geomechanical model. In addition, work was done on sub-modelling techniques, on the scaling of rock parameters and on the further development of modelling techniques.

The following report provides an overview of the work carried out so far in the project SpannEnD 2.0. The structure of the document is based on the work packages (AP) of the project outline. In the first work package, the project aims to further develop and provide an improved geomechanical-numerical stress model for Germany that incorporates geological models and rock mechanics data and is calibrated and validated with stress observations. This stress model of Germany can be used, among other things, for subspatial and large-scale regional comparisons, but also provides the necessary boundary conditions for more detailed regional and site models. Suitable sub-modelling techniques for consistent linking of the different model scales will be further developed in a second work package and verified by application to sub-area 001 and a sub-area of sub-area 009. In the third work package, the various measurement methods for determining stress variables will be evaluated and generally applicable recommendations for optimising exploration programmes regarding the parameterisation and calibration of the geomechanical-numerical modelling will be developed.

2 Enhancements of the Germany stress model (AP1)

2.1 Determination of stress magnitudes and status of the stress data compilation Germany

2.1.1 Introduction

Physically, stress is defined as an external force acting on a plane. Thus, it has SI units of force per area (N/m^2) which is commonly referred to as Pascal (Pa). To describe the stress state at a point, the Cauchy stress tensor σ with nine components is used. It consists of three forces that act on three planes that are perpendicular to each other (Fig. 2.1a). Due to the symmetry of the stress tensor one can always rotate the coordinate system in such a way that the three forces are perpendicular to the sides (Fig. 2.1b). This is a so-called principal axis system with three principal stresses. Regardless of their orientation in space, the largest principal stress is labelled as S_1 , the intermediate principal stress as S_2 and the smallest principal stress as S_3 (Fig. 2.1b). In geosciences it is often assumed that the vertical stress S_V is a principal stress. With this assumption the maximum and minimum horizontal stress $S_{H\max}$ and $S_{H\min}$, respectively, are principal stresses as well (Fig. 2.1c). This simplified stress tensor has only four unknowns: The orientation of $S_{H\max}$ and the magnitudes of $S_{H\min}$, $S_{H\max}$ and S_V . Note, that due to convention principal stress orientations of S_1 , S_2 and S_3 are not fixed in space, but can change abruptly by 90° (Fig. 2.1e).

In the following subsections we use the terminology of the so-called reduced stress tensor as this is also used in throughout the literature. However, it should be noted that for the estimation of stress magnitudes, the Hydraulic Fracturing (HF) tests indeed measure the smallest principal stress S_3 and the Sleeve Reopening (SR) test allows to derive S_1 or S_2 , depending on which of these two stresses is close to the $S_{H\max}$ orientation (Fig. 2.1e).

An overview of the methods for determination of individual components of the stress tensor is presented below. All methods except HF tests do not measure stress directly but use indirect observations of strain. Thus, we avoid using the term stress measurement but use instead the term stress indicator. A graphical overview of the stress indicators is shown in Fig. 2.2. For more technical and physical details, there are extensive review literature and textbooks e.g., Amadei and Stephansson (1997); Cornet (2015); Schmitt et al. (2012); Zang and Stephansson (2010); Zoback (2007).

A number of methods that are not presented in Fig. 2.2 are suitable for determining the stress orientation by means of the $S_{H\max}$ orientation. These include earthquake fault plane solutions, geological indicators as well as the orientation of borehole breakouts and drilling-induced tensile fractures that are observed using caliper logs as well as acoustic, electrical, or optical imaging methods. These methods are explained in the mentioned textbooks and review article but are not further discussed in this document. Here we focus on the methods that give information on the stress magnitudes of $S_{H\min}$ and $S_{H\max}$. The magnitude of the vertical stress S_V can be estimated from

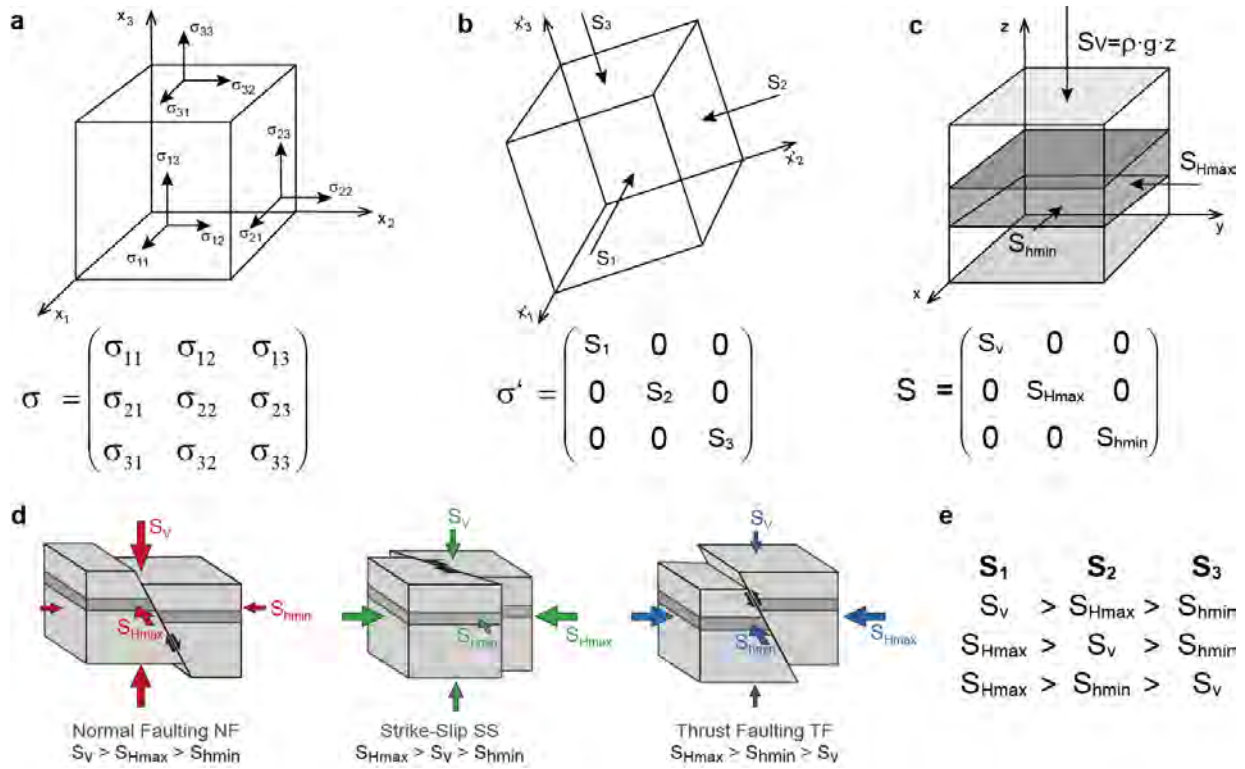


Figure 2.1: Definition of the stress tensor and the tectonic stress regime. a) The stress tensor at a point is described as three forces acting on three perpendicular faces of an infinitely small cube. b) Due to the stress tensor symmetry a coordinate system exists where the three forces are perpendicular to the three cube faces. In this principal axis system, the remaining three forces are called principal stresses. c) Assuming that the vertical stress $S_v = \rho g z$ is a principal stress (ρ = density, g = gravitational acceleration, z = depth), the minimum and maximum horizontal stresses S_{Hmin} and S_{Hmax} , respectively, are principal stresses as well. d) The stress regime is defined by the magnitude of the three principal stresses S_{Hmax} , S_{Hmin} and S_v . e) Note that S_1 , S_2 and S_3 change their orientation abruptly with respect to a geographical coordinate system when the stress regime changes.

the overburden load with relative great precision. If borehole measurements are available, density logs can be used to integrate their values over depth. If measured data are not available, bulk density is usually assumed based on stratigraphic information and rock sample measurements. However, in cases of shallow depth and high topography, the assumption that the S_v is a principal stress is generally not valid which is in particular the case for shallow measurements in mountainous regions (Evans et al., 1989; Figueiredo et al., 2014; Savage et al., 1985; Warpinski and Teufel, 1991).

2.1.2 Loading methods to determine S_{Hmin} and S_{Hmax} magnitudes

In loading methods such as hydraulic fracturing, sections of approximately one meter with no pre-existing fractures at the borehole wall are subjected to steadily increasing fluid pressure. This makes it possible to infer the minimum principal stress S_3 or at least its lower limit. If the minimum

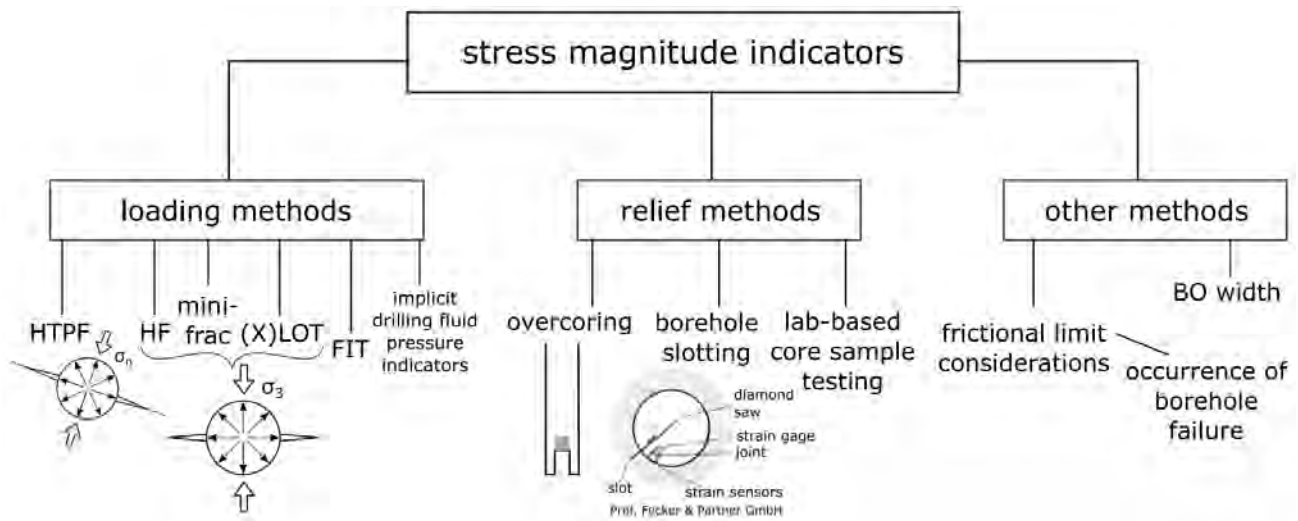


Figure 2.2: Stress magnitude indicators. Abbreviations: HF - hydraulic fracturing, HTPF - hydraulic testing of pre-existing fractures, (X)LOT - (extended) leak-off testing, FIT - formation integrity testing, BO- borehole (wellbore edge) breakout, σ_n - normal stress, S_3 - minimum principal stress.

principal stress is horizontal S_3 is equal (or is close to) S_{hmin} . In the case of a thrust faulting stress regime, however, S_3 is equal to S_V and therefore measures in most cases only the overburden load. Under specific conditions one can still measure S_{hmin} in thrust faulting stress regime, i.e. when $S_{hmin} > S_V$, but this is ambitious and needs expert elicitation of the pressure curves (Desroches et al., 2021).

Often, pressure tests are performed for the purpose of drilling safety, optimising the drilling process, and maintaining wellbore stability rather than for deriving stress data. The rock volume for which the hydraulic test provides valid data is directly related to the test duration and the amount of fluid injected. Sometimes it can be constrained from drilling logs. In general, classical interpretations of stress tests assume that the borehole axis is parallel to one of the principal stresses. Too much deviation invalidates the classical method of interpreting test results (Haimson and Cornet, 2003; Schmitt and Haimson, 2017). Therefore, boreholes used for classical approaches to stress determination by loading tests should be vertical or at least subvertical, or more generally aligned along a principal stress axis. In deviating scenarios, special inversion methods must be used.

2.1.2.1 Leak-off Tests and Formation Integrity Tests

Leak-off tests (LOT) and formation integrity tests (FIT) are commonly used in the hydrocarbon industry to estimate the upper limit of mud weight that can be used in drilling without fracturing the borehole wall. As shown in Fig. 2.3 b, the tests are conducted in an open hole several meters long below the casing shoe (Addis et al., 1998; White et al., 2002). During the course of a LOT, the mud pressure is increased until the pressure build-up deviates from a linear trend, indicating fluid loss into the rock. This is interpreted to be due to the development of a small tensile fracture (Bell, 1996). However, there is evidence that shear failure could also be triggered by fluid pressure

increase (Chan et al., 2014; Couzens-Schultz and Chan, 2010; Zhang et al., 2011). However, the conventional assumption is that these are tensile failures. Leak-off pressure (LOP) is determined from the shape of the pressure curve (White et al., 2002).

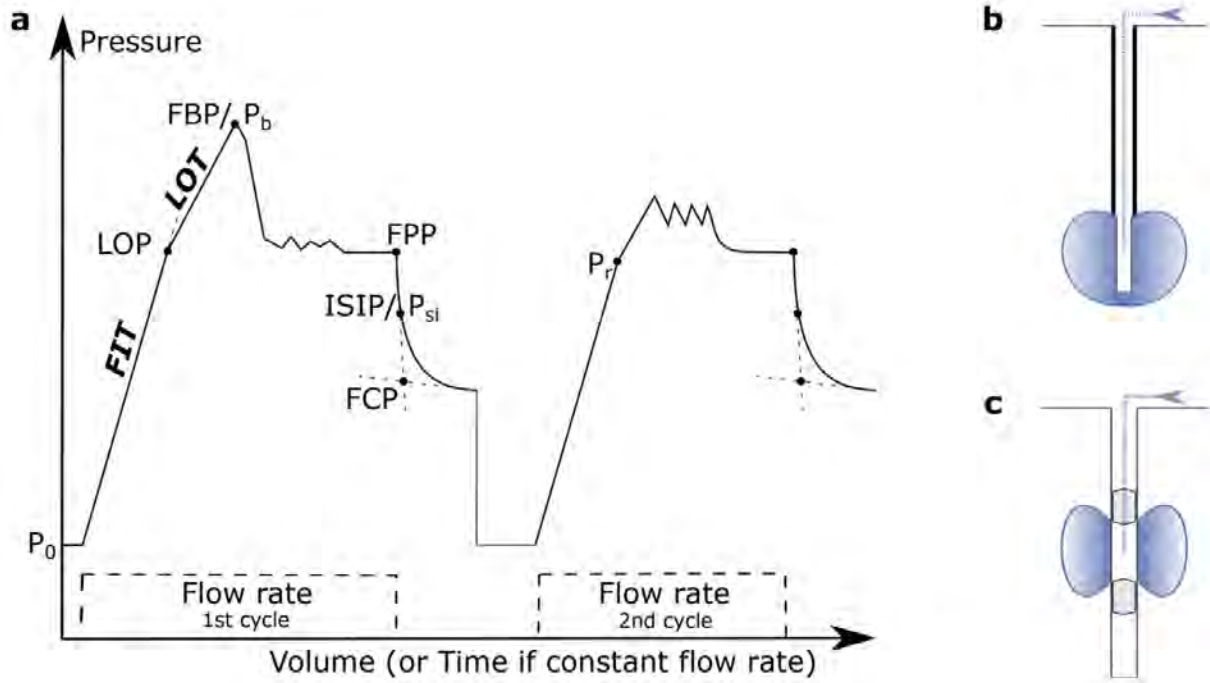


Figure 2.3: Hydraulic pressure curves. a) Schematic pressure curve of fluid injection tests (after White et al., 2002). FIT marks the stage in which the pumping is ceased in case of formation integrity tests, LOT marks the corresponding stage for leak-off tests. The continued curve is valid for hydraulic fracturing, mini-fracs and extended leak-off tests (XLOT). The pressure values to be picked are abbreviated as follows: LOP leak-off pressure, FBP/ P_b formation breakdown pressure, FPP formation propagation pressure, ISIP/ P_{si} instantaneous shut-in pressure, FCP fracture closure pressure, P_r reopening pressure. P_0 is the pore pressure prior to pumping. b) Schematic setup of (X)LOTs and FITs at the uncased bottom section of a borehole. c) Schematic setup of hydraulic fracturing and mini-frac procedures in a packed borehole section.

XLOTs are more comprehensive and longer (extended) leak-off tests in which pumping continues beyond the leak-off pressure (LOP) and are performed primarily to determine the fracture closure pressure (FCP). An XLOT consists of at least one complete cycle of leak-off, formation failure, fracture propagation, shut-in, and fracture closure (Addis et al., 1998; Bell, 1996; Kunze and Steiger, 1991; Li et al., 2009; White et al., 2002). Fig. 2.3a shows a schematic representation of an XLOT pressure curve, where the section during which simple LOTs are stopped is also marked. Depending on the type of test (LOT or XLOT), the leak-off pressure (LOP), the fracture propagation pressure (FPP), the instantaneous shut-in pressure (ISIP), or the fracture closure pressure (FCP) are used to derive the S_{hmin} magnitude (see Fig. 2.3a). In general, LOP is the least reliable for estimating S_{hmin} and tends to slightly overestimate S_{hmin} (Bell, 1996; Breckels and van Eekelen, 1982). However, when XLOT data are available, both FCP and ISIP can be used to provide more reliable information for deriving

the S_{hmin} magnitude (Addis et al., 1998; Enever et al., 1996; White et al., 2002). In particular, FCP information from repeated cycles is more reliable than that from the first cycle because second- or third-cycle FCP values have less influence of rock tensile strength and therefore provide a more accurate estimate of S_{hmin} (Bell, 1996). Traditional approaches to determining FCP include the double tangent method (e.g., Enever and Chopra, 1986) and square root time analysis (Guo et al., 1993).

It is now more common to use a G-function analysis (Castillo, 1987) or another time-based derivation method. Which strategy is appropriate, depends largely on the permeability of the rock formation under study of Schmitt and Haimson (2017). They also provide a more comprehensive review of strategies for extracting S_{hmin} from pressure curves. Different methods can generate different values using the same initial data. However, White et al. (2002) and Zoback et al. (2003) found that there is little difference between LOP, FPP, and ISIP and that all can serve as a proxy for S_{hmin} . Raaen et al. (2006) disagree with this assumption, at least when high accuracy is required. It is common practice to consider the LOP as an upper limit for S_{hmin} . Since S_{hmin} corresponds to the pressure required to reopen a pre-existing fracture, LOTs can only provide a rough estimate that is unadjusted for rock strength exceeded. A detailed comparison of LOTs and XLOTs is provided by Addis et al. (1998). They conclude that an XLOT provides much better data compared to a LOT, and therefore recommend the former for estimating stress magnitudes.

If fluid injection is stopped before the LOP is reached (cf. Fig. 2.3a), this is called a FIT or limit test (Zoback, 2007). The original purpose of FITs is to test whether the open hole section can stably withstand the additional pressures encountered during drilling and production. The FIT values most likely yield only lower limits of S_{hmin} , except at very high tensile strengths, because the test is stopped before a fracture is initiated. Since the uncertainties in the derived stress determination are large, FITs should only be used for a lower limit of S_{hmin} magnitude value when no other information is available. It should be noted that FITs are different from DFIT (Diagnostic Fracture Injection Test), which we discuss in the section 2.1.2.3 on Micro-Hydraulic Fracturing (MHF) Tests.

2.1.2.2 Hydraulic-Fracturing-Tests

In hydraulic fracturing tests, a section of the borehole is sealed by packers (Haimson and Cornet, 2003; Schmitt and Haimson, 2017), as shown in Fig. 2.3c. Fluid pressure is increased to the point of leakage, and rock stresses are derived from pressure curves, from which characteristic values must be taken for this purpose (Fig. 2.3a). These values are the breakdown pressure P_b , the reopening pressure P_r and the shut-in pressure P_{si} . P_b is defined analogously to FBP and P_{si} analogously to ISIP, only the common nomenclature varies within the literature. For an estimate of S_{hmin} magnitude assuming initially intact rock, both P_{si} and FCP are used. P_{si} is the pressure immediately after shut-in and higher than FCP. It is considered an upper limit for the S_{hmin} magnitude value (English et al., 2017). Although it is common to equate P_{si} directly with S_{hmin} (e.g., Haimson and Cornet, 2003), it is recommended to use FCP as an estimate of S_{hmin} because FCP is the pressure that opposes fracture closure and therefore tends to be equal to or slightly lower than S_{hmin} (Schmitt and Haimson, 2017).

2.1.2.3 Micro-Hydraulic Fracture-Tests

In contrast to HF tests, Micro-Hydraulic Fracture (MHF) tests are only short duration fracking operations performed to establish small fractures in reservoirs. Because only a small amount of water is injected, it should be noted that only small volumes of rock are affected. MHF tests are explicitly used to estimate the S_{hmin} magnitude.

In the petroleum industry, the acronym DFIT (Diagnostic Fracture Injection Test) has also been established to refer to virtually any test in which stresses are estimated regardless of procedure or geometry (Schmitt and Haimson, 2017). Sometimes this term is used synonymously with MHF tests, or referred to as mini-fall-off, injection fall-off test, or fracture calibration test (Wang and Sharma, 2017). They were developed specifically for unconventional hydrocarbon exploration and involve extensive and closely timed post-shut-in pressure monitoring. However, DFITs typically use only a single pressure build-up cycle and are often performed through perforated casing. Careful attention must therefore be paid to the actual procedure used to determine if it is suitable for stress state interpretation.

2.1.2.4 Hydraulic Tests on Pre-existing Fractures

An alternative approach to fracturing intact rock to estimate stress magnitudes is the HTPF method (Hydraulic testing of pre-existing fractures; Cornet, 1986). To solve the given inverse problem, fractures with different orientations are opened selectively in several sub-tests. Since a single test reproduces the normal stress on the particular fracture under investigation, a best-fit solution of the 3-D stress tensor can be derived from at least six sub-tests on different, non-parallel fractures. Additional test runs should be sought to better represent uncertainties. The method is applicable to all well orientations and is also independent of pore pressure effects and determination of material properties. A clear advantage over classical HF is that the complete 3-D stress tensor can be determined. In addition, it is possible to combine HF and HTPF when the borehole is vertical. In such cases, the S_{hmin} magnitude can be obtained from the HF test, while three to four HTPF runs are sufficient to determine the magnitudes of S_{Hmax} and S_v without having to consider pore pressure or tensile strength (Haimson and Song, 1993). Ask (2017) presented a wire-line logging tool for hydraulic determination of rock stress in narrow boreholes as a fairly recent technical development that combines the HTPF method with HF testing and sleeve fracturing (see Section 2.1.2.5) to determine the 3-D stress tensor. The system is expected to provide reliable results with low measurement uncertainties and has been successfully tested (Ask, 2017).

2.1.2.5 Sleeve Fracturing

In addition to MHF tests the use of "dry" fracture-opening methods can help to improve the reliability of the S_{hmin} measurement and S_{Hmax} determination (Desroches et al., 2021; Stephansson, 1983). This is done in two ways: Upstream of the MHF, pre-treatment of the borehole section with a third, centrally placed packer can provide a more controlled fracture initiation (step 1 in Fig. 2.4) that is not influenced by the packers bounding the section and avoids propagation of the hydro-frac under the lower packer and into the open borehole (packer bypass) (cf. Detournay and Carbonell, 1997). (The rock can also be fractured at a lower failure pressure than hydraulic fracturing, which can be

particularly useful for testing in stiff formations where classic straddle packers have limitations). The fracture can penetrate deeper into the formation through the hydraulic opening in the next step (step 2 in Fig. 2.4).

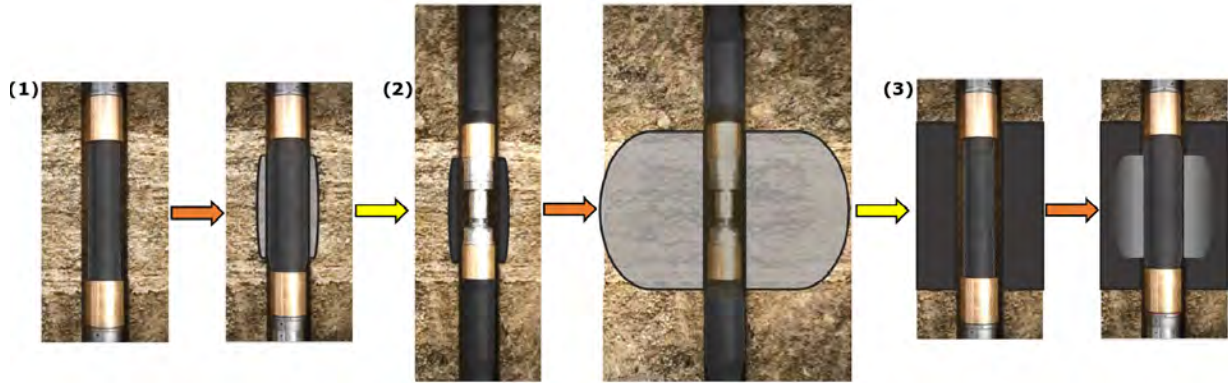


Figure 2.4: Combination of Micro-Hydraulic Fracturing (MHF) and Sleeve Fracturing (SR) methods. (1) Dry fracture initiation (SR), (2) hydraulic fracturing (MHF), and (3) Dry Sleeve Reopening, (figure taken from Desroches et al., 2021).

After HF treatment, sleeve reopening can again be used (step 3 in Fig. 2.4) to constrain the S_{Hmax} magnitude, although this requires estimating the fluid pressure P_f within the fracture as additional quantitative information, which in principle cannot actually be measured (Desroches et al., 2021).

$$P_{SR} = 3 |S_{hmin}| - |S_{Hmax}| - P_f. \quad (2.1)$$

P_{SR} (Eq. 2.1) is the re-opening pressure of the induced fracture in the course of sleeve reopening (SR). According to Desroches and Kurkjian (1999), to estimate P_f , it is necessary to diagnose whether a mudcake is impeding connectivity into the formation; in this case, P_f would correspond to reservoir pressure. In the presence of a permeable and unsealed formation, on the other hand, there would be a tendency toward hydrostatic pressure or initial mud pressure. The consecutive steps of the method are illustrated in Fig. 2.4, which are 1.) dry fracture initiation (sleeve fracturing), 2.) hydraulic fracture opening, and 3.) dry sleeve reopening. This can be done by a combination of a classical double packer and a single packer (e.g., Mishra et al., 2011), or with a specially designed three-packer system in which the apparatus does not have to be repositioned in the course of the three steps mentioned (cf. Desroches et al., 2021).

2.1.2.6 Stress Orientations from MHF Tests

Before using the packer apparatus for the stress tests, images of the borehole wall are usually taken in order to select a suitable borehole section. The stress orientation is determined following the pressure measurements required for the magnitude determination. For this purpose, the imaging instrument is used a second time to check whether and where new fractures have developed. The orientation of the fractures produced can be interpreted in terms of stress orientation: If a pair of opposite tensile fractures parallel to the borehole has been generated, the fracture azimuth is interpreted as S_{Hmax} orientation (cf. Fig. 2.2).

2.1.2.7 Uncertainties in Loading Methods

In particular, the derivation of stress magnitudes from pressure curves from a borehole section that is not specifically sealed with packers at the top and bottom results in various uncertainties: In the absence of a preliminary exploration of the borehole wall, e.g., in the (X)LOT method, it is not ensured that a new fracture is induced and not only that an already existing fracture is opened. Since the latter is not necessarily aligned with S_{hmin} , this can lead to an overestimation of the S_{hmin} magnitude. In addition, the geometry of the wellbore bottom can influence the fracture initiation process in that an initially horizontal fracture can be induced (Haimson and Fairhurst, 1969) before reorienting to the vertical direction according to the S_{Hmax} orientation prevalent in the reservoir (Li et al., 2009). Furthermore, when shear occurs, the LOP underestimates the S_{hmin} magnitude (Couzens-Schultz and Chan, 2010).

Since even in borehole sections beyond the bottom of the borehole, induced fractures are not always perpendicular to S_{hmin} but may be influenced by pre-existing planes of weakness such as natural fractures. According to the MHF method, prior borehole imaging is therefore essential to verify the validity of the fracture under investigation. However, induced fractures can also twist and bend (tortuosity), especially when S_{hmin} and S_v are close to each other, so that the stress state varies significantly with distance from the borehole wall. On the other hand, this implies that although the stress state near the borehole may initially influence fracture initiation, once the fracture has propagated away from the borehole, the undisturbed stresses reassert themselves and control the orientation of the fracture (Warren and Smith, 1985). This, in turn, suggests that pressure records are generally useful for making inferences about the S_{hmin} magnitude. However, if it is uncertain whether a normal faulting stress regime prevails, e.g., at shallow depths, but also in areas generally unexplored with respect to stress, one should always check whether the S_{hmin} magnitude value derived from the pressure records approximates the calculated vertical stress of the overburden. In such cases, S_3 should not be equated with S_{hmin} , as it may actually be S_v .

The literature contains further references to uncertainties in stress determination using loading methods and, in some cases, approaches to reducing them. For example, Liu et al. (2018) showed that FBP decreases with increasing stress magnitude ratio S_{Hmax}/S_{hmin} . They also investigated the effects of oriented perforations that deviate from the S_{Hmax} orientation and found that FBP increases with larger orientation deviations. For fluid injection methods, procedures with multiple consecutive cycles are generally preferable to single injection tests because the interpretation of the pressure curve is more reliable in terms of both fracture initiation effectiveness and quantification of characteristic values. Haimson and Cornet (2003) recommend performing at least three pressurization cycles at the same flow rate. In addition, downhole pressure measurements are preferable to recording pressure at the ground surface (where the hydrostatic pressure of the downhole fluid would have to be added; Zoback, 2007), although for tests at depths up to 500 m in hard rock with low permeability, recording at the surface is sufficient (Schmitt and Haimson, 2017). Li et al. (2009) pointed out that interpretation of pressure test results is complicated by the use of non-Newtonian drilling fluid, which is common in XLOTs. Wellbore deflection and azimuth also affect LOT results, making individual LOTs generally unreliable for determining stress magnitude in inclined wells. However, when multiple LOTs are available within the same stress environment, inversion methods can improve the derivation of S_{hmin} magnitude (Aadnøy, 1990). Furthermore, which formula and strategy is appropriate in a given case depends on the geologic setting of the study area. Therefore, the analytical correlation

between pressure values and stress magnitudes remains difficult to validate because there is no universal solution, especially with respect to the estimation of S_{Hmax} magnitude.

2.1.2.8 Challenges to Estimate the S_{Hmax} magnitude

The determination of the S_{Hmax} magnitude has been a topic of debate among experts for decades. Following the pioneering work of Hubbert and Willis (1957), several authors such as Scheidegger (1962), Kehle (1964), Haimson and Fairhurst (1967) and Fairhurst (1964) further developed the concept of hydraulic fracturing to derive the S_{hmin} and S_{Hmax} magnitudes from P_{si} , P_r , P_b , P_0 and the tensile strength assuming an intact, homogeneous and elastic rock. Since then, the concept has been further developed, challenged or extended by various authors. Aspects considered include the influence of fracking fluid viscosity and injection rate (Guo et al., 1993), determination and interpretation of P_r (Bredehoeft et al., 1976; Ratigan, 1992; Rutqvist et al., 2000), differences between successive injection cycles (Bredehoeft et al., 1976; Hickman and Zoback, 1983; Rutqvist et al., 2000), an integration of Biot's poro-elastic theory (Haimson, 1968; Schmitt and Zoback, 1989), and aspects of fracture mechanics (Abou-Sayed et al., 1978; Rummel et al., 1986).

According to the conventional approach to calculating S_{Hmax} magnitude by Bredehoeft et al. (1976), the tensile strength of the rock is determined as the difference between the failure pressure, P_b , and the reopening pressure, P_r . This is to avoid uncertainties resulting from laboratory tests to determine the tensile strength. Ito et al. (1999) cite two sources of error associated with the method proposed by Bredehoeft et al. (1976). First, it does not consider the penetration of fluid pressure into the fracture before reopening. To address this, Ito et al. (1999) propose a modified equation. Second, the actual reopening pressure is systematically overestimated from the borehole pressure records. This discrepancy becomes greater the greater the hydraulic compliance of the test equipment (hydraulic compliance; the ability to accommodate sudden changes in external pressure load), so Ito et al. (1999) suggest reducing the flow rate by several orders of magnitude compared to conventional HF systems if the goal is also to determine S_{Hmax} magnitude. In shallow depth tests, this requires only minor changes to the system, but in deep wells it is recommended that flow measurements be made directly at the well packers in the process (Ito et al., 1999). Evans et al. (1989) further pointed out the difficulties in determining P_r when $S_{Hmax} > 2S_{hmin} - P_0$, where P_0 is the ambient pore pressure before pumping. Further discussion of the issue can be found in Zoback (2007). For example, in tests using perforated well casings, the physical conditions used to derive S_{Hmax} magnitude from pressure curves are invalid because fracture initiation is not determined by the stress concentration around the wellbore (Zoback, 2007). A brief summary of the calculation of S_{Hmax} magnitude can be found in the methods paper by Haimson and Cornet (2003).

In general, the calculation of S_{Hmax} magnitude involves geomechanical assumptions and several read-off pressure curve values as intermediate results, each of which is subject to uncertainty. Consequently, the result is associated with a large overall uncertainty. In addition, there are potentially other sources of error due to inadequately accounted for pore pressure effects (Haimson and Cornet, 2003). In addition, third-party data publications are often incomplete in terms of physical and geological assumptions, measurement curves, pressure values, and quantitative uncertainties of measurements. When interpreted retrospectively, it is therefore all the more difficult to quantify the overall uncertainties. In any case, the estimation of the S_{Hmax} magnitude is subject to larger uncertainties than that of the S_{hmin} magnitude.

2.1.3 Relief Methods

The basic principle of relief methods is to relieve a rock sample by removing the surrounding volume and recording its deformation response (Ljunggren et al., 2003). These methods include overcoring (Hast, 1958; Leeman, 1964, 1968), borehole logging (Becker and Werner, 1994; Bock and Foruria, 1984), and tests on core samples in the laboratory (Strickland and Ren, 1980; Teufel, 1983; Yamamoto et al., 1990). Given the expected scatter of small-scale tests, as in the case of unloading methods, it is reasonable and even desirable to consider multiple tests to infer the stress state at a given location. However, it should be noted that in order to combine test results, the validity of the continuity hypothesis must be ensured, which requires detailed knowledge of the local geology (Ask, 2017).

2.1.3.1 Overcoring Methods

In overcoring, strain sensors are attached to the in-situ sample prior to drilling to measure the strain resulting from mechanical decoupling (Hast, 1958; Leeman, 1964, 1968). With knowledge of the elastic rock properties, the full 3-D stress tensor can be calculated from the strain values of a single set of measurements. A variety of strain gauges are used to perform over-drill tests. For example, Fig. 2.5 shows the steps of a single measurement with a Borre probe (Sjöberg et al., 2003; Sjöberg and Klasson, 2003). However, the underlying physical principle and thus the general sequence of the procedure applies regardless of the manufacturer: After drilling a pilot hole, strain gauges are bonded to the rock that has not yet been dissolved. In the next step, the measuring cell is over-drilled with a larger drill bit, which effectively relieves the stresses acting on the rock. Strains are measured before, during and after overcoring. From the strains, the in-situ stress state is calculated assuming continuous, homogeneous, isotropic and linear elastic rock behaviour. The required elastic rock properties, namely Young's modulus and Poisson's ratio, are usually determined at the measurement site by biaxial testing. During a measurement campaign, several measurements are usually made in the close-up range of typically 0.5–1.0 m in order to form more meaningful average values. The resulting oriented stress tensor can be transformed into any coordinate system (Sjöberg et al., 2003).

2.1.3.2 Borehole Slotter

A borehole slotter probe is a device that provides in-situ stress relief without over-drilling (Bock and Foruria, 1984). In this method, a strain sensor records signals while and after a saw blade cuts a slot in the borehole wall (Becker and Werner, 1994). This method is limited to dry, shallow boreholes and also requires independently obtained information on the elastic properties of the rock (Bock, 1993). Although it is no longer widely used and is not suitable for deeper explorations it is mentioned here because there have been several applications in Germany and Switzerland, the data from which can be encountered in appropriate research.

2.1.3.3 Tests on Core Samples in the Laboratory

The components of the in-situ stress tensor can also be derived from measurements of the deformation behaviour of drill core samples in the laboratory, where there are methods with or without a reloading of the rock samples.

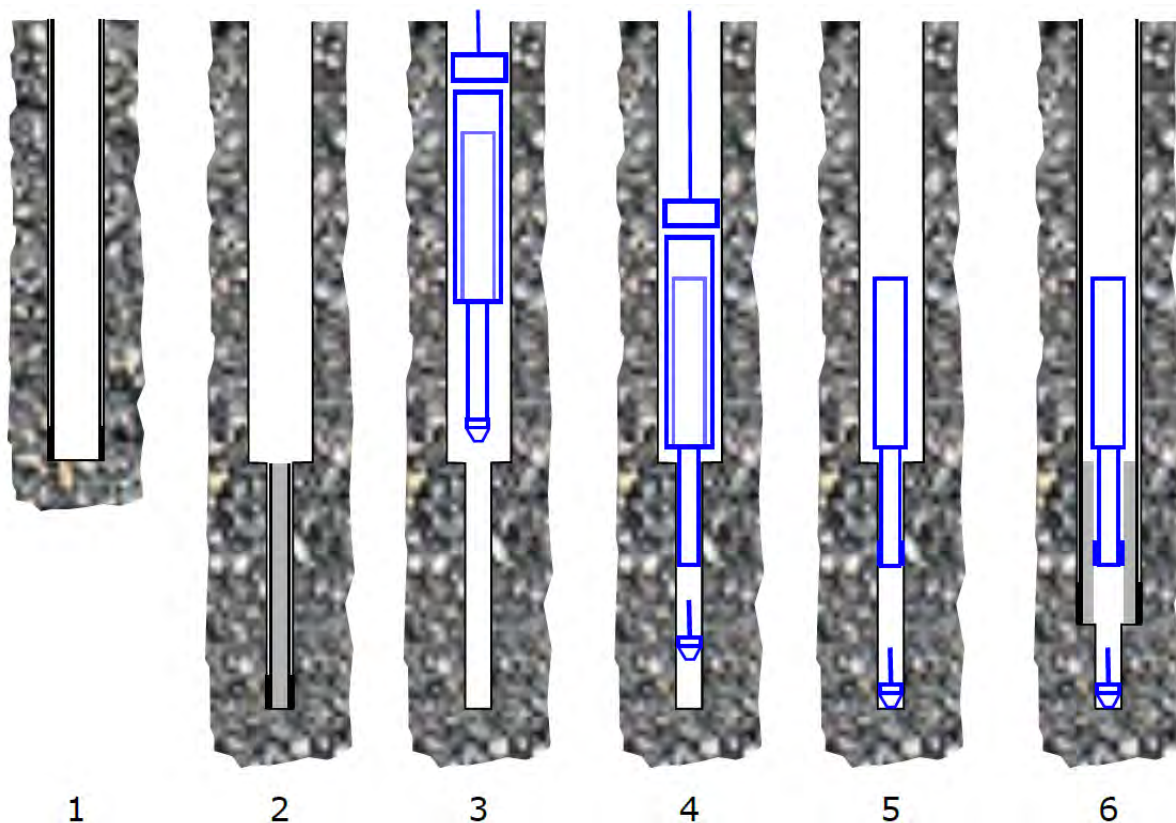


Figure 2.5: Implementation of the overcoring method on the example of the Borre probe (Sjöberg and Klasson, 2003); the principles can be applied to any overcoring method (Sjöberg et al., 2003). Figure and description were adapted from Sjöberg et al. (2003). (1) Drill main borehole (76 mm diameter) to measurement depth. Grind borehole bottom using a planning tool. (2) Drill pilot hole (36 mm diameter) and recover the core for appraisal. Flush the borehole to remove drill cuttings. (3) Apply glue to strain gauges. Insert the probe with installation tool into hole. (4) Let the probe tip with strain gauges enter the pilot hole. Release the probe from installation. A compass released at the same time is recording the installed probe orientation. Gauges are bonded to the pilot hole wall. (5) Pull out installation tool and retrieve to surface. The probe is bonded in place. (6) Allow glue to harden overnight. Then overcore the probe and record strain data using the built-in data logger. Break the core and recover it to the surface.

A method without reloading is called anelastic strain recovery (ASR) and measures the strains on oriented cores to derive the magnitudes of S_{hmin} and S_{Hmax} from the principal strain magnitudes. To do this, S_v from the surcharge and Poisson's ratio must first be determined. Unlike overcoring, the measuring instruments are installed only after the stress has been relieved (Teufel, 1983; Teufel and Warpinski, 1984). Thus, a subcomponent of ASR can still be determined that is sufficient for stress magnitude determination if (1) the rock is homogeneous and linearly viscoelastic, (2) the viscoelasticity of the rock can be characterised by a viscoelastic parameter, (3) the Poisson's ratio is not time-dependent, and (4) the in-situ stresses are instantaneously relieved. In the case of

transversely isotropic cores, at least one additional viscoelastic parameter is required (Blanton, 1983). A relatively new approach without reloading, but providing only the differential stress ($S_{Hmax}-S_{Hmin}$), is diametrical core deformation analysis (DCDA; Funato and Ito, 2017). In this method, strains are determined using an optical micrometre. Although this method does not provide isolated information on the principal stress magnitudes, it can be used to determine the S_{Hmax} magnitude if the S_{Hmin} magnitude is known, e.g., from a hydraulic fracturing test near the original position of the core sample. As with all approaches to strain analysis, the elastic modulus and Poisson's ratio must be determined, and the rock must meet the requirements of homogeneity, isotropy, and linear elasticity (Funato and Ito, 2017).

Core sample-based reloading methods use microfractures generated by stress relief during core removal. The density of microfractures is assumed to be proportional to the stresses relieved along the corresponding directions. How these fractures close under different pressure applications in the laboratory is investigated. The basic principles were described by Strickland and Ren (1980). Different approaches to their implementation are explained in the following paragraphs.

In wave velocity analysis (WVA), the anisotropic acoustic wave velocities are measured in oriented samples (Braun et al., 1998; Ren and Hudson, 1985). Directional ultrasonic waves are induced to measure the wave travel time through the oriented rock sample under increased isotropic loading. The anisotropy of the wave velocity is due to the orientation of micro tensile fractures, which in turn correlates with the in-situ stress state from which the sample was extracted. The minimum of the wave velocity is oriented along S_{Hmin} .

Yamamoto et al. (1990) developed the deformation rate analysis (DRA) method, which uses cycles of uniaxial compression application to define a strain difference function. This axial stress function is obtained by subtracting the axial strains from different loading cycles. The in-situ stresses are estimated from the gradient changes of the strain difference functions.

In differential strain analysis (DSA), released rock samples are isotropically compressed. The pressure is increased in a stepwise manner. The applied load corresponding to the vertical in situ stress, the in-situ pore pressure, and the Poisson's ratio are required to derive the in-situ stress magnitudes (Widarsono et al., 1998).

2.1.3.4 Uncertainties in Relief Methods

When measurements are performed in the context of construction projects such as tunnel excavations, the results should be interpreted with particular caution. Although this is not only true with respect to unloading methods, these are used particularly frequently in the civil engineering context. Because free surfaces of structural measures in the subsurface disturb the stress state, measurements taken directly behind a tunnel wall are not reliable indicators of the undisturbed stress state. Brady and Brown (2006) assume a zone of influence of 5 times the radius of the cavity in the case of a circular shape.

Since the assumption of ideal rock behaviour (continuous, homogeneous, isotropic, and linear-elastic or linear-viscoelastic) is rarely fully satisfied, errors inevitably occur. A study by Amadei and Stephansson (1997) showed that the expected inaccuracy of overcoring results is at least 10–20% even under near-ideal rock conditions. Leijon (1989) showed that the absolute scatter in overcoring data from hard rock is ± 2 MPa, implying that overcoring results at shallow depths, where stress magnitudes are low, are particularly uncertain in relative terms. In addition, Irvin et al. (1987)

pointed out the possible occurrence of boundary yield, i.e., mechanical yielding at the interface between the borehole and the measuring cell. This can lead to a significant increase of the stress magnitude aligned parallel to the borehole. Therefore, they recommend performing measurements in two orthogonal boreholes at one location.

Relief methods derive stresses from small-scale strains, so their results generally depend heavily on the accuracy of the corresponding measurements (Bertilsson, 2007; Hakala, 2007; Hakala et al., 2003). Ask (2003) indicates that adhesion between sensors and rock sample, temperature effects, and the determination of elastic parameters are measurement-related uncertainties. Furthermore, Ask particularly criticises the potentially improper handling and the quality of the adhesive used to attach the sensors to the rock. Not only when overcoring, but in general, temperature control is a critical measure to avoid large inaccuracies. Poorly performed biaxial tests can also lead to biased results if the stress calculation depends on the determined rock properties (Ask, 2003). If there are inaccuracies or ambiguities regarding the fulfilment of the theoretical assumptions or if the results are contradictory, Ask (2017) recommends using other stress indicators to compare data to decide which data can be trusted.

According to Widarsono et al. (1998), the DSA method should only be used under the assumption that all microfractures present in a tested specimen have developed due to stress relief, or at least that all microfractures already present do not significantly affect the measured deformation. In addition, they indicate that grain size heterogeneities have a strong influence on the orientation of microfractures formed by stress relief. This remark applies to all methods based on the study of microfractures due to stress relief.

2.1.4 Other Methods

2.1.5 Frictional Limit as Upper Bounds of Stress Magnitudes

Assuming that the earth's crust is penetrated by pre-existing faults that are optimally aligned in the prevailing stress field, and further assuming that these faults are at their frictional limit, the magnitude ratio of the maximum and minimum principal stresses is given by

$$\frac{\sigma_1}{\sigma_3} = \frac{S_1 - P_P}{S_3 - P_P} = [(\mu^2 + 1)^{1/2} + \mu]^2 \quad (2.2)$$

where μ denotes the friction coefficient (Jaeger et al., 2011; Sibson, 1974). If the stress regime is known and S_V is assumed to be a principal stress, upper bounds can be estimated for the S_{hmin} magnitude in the case of a thrust faulting stress regime or for the S_{Hmax} magnitude in the case of a normal faulting stress regime. In the case of a strike-slip stress regime where S_V is the mean principal stress, further assumptions or information are required. In this case, the stress state can be constrained with a so-called stress polygon (Schoenball et al., 2018; Zoback et al., 2003; Zoback, 2007). Here, additional information, e.g., from FITs or LOTs, can be included to further constrain the upper and lower limits of the horizontal principal stresses.

Since the friction limit approach is based on a number of simplifying assumptions and knowledge of the friction coefficient (μ), its reliability is more limited compared to stress magnitudes derived from the indicators described in the previous sections. Moreover, it provides only upper limits of possible ranges of values. An implementation of the friction limit approach supported by empirical

information is possible by including borehole failure observations (borehole breakouts, BOs; drilling-induced tensile fractures, DIFs; see next subsection) in combination with rock strength. These additional data can also be integrated into a stress polygon and allow the S_{Hmax} magnitude to be constrained even in deviated wells when S_{Hmin} is already known (Moos and Zoback, 1990; Peška et al., 1995; Schoenball and Davatzes, 2017; Valley and Evans, 2007).

2.1.5.1 Borehole Breakouts and Drilling Induced Tensile Fractures

While the orientation of BOs indicates the orientation of S_{Hmin} (cf. Fig. 2.2), the opening width of the wellbore edge breakouts can be analysed to infer the ratio of stress magnitudes. Thus, if the S_{Hmin} magnitude is already known, the S_{Hmax} magnitude can be estimated if a wellbore failure is observed within the same lithologic layer and rock strength information is also available (Barton et al., 1988; Lee and Haimson, 1993; Shen, 2008; Vernik and Zoback, 1992). Shen (2008) used numerical modelling to establish a quantitative relationship between BO expression and stress magnitudes. However, this is only valid for isotropic rock behaviour with assumptions on rock compressive strength, elastic parameters, and friction coefficients. In addition, the analytical result is highly dependent on the failure criteria used (Valley and Evans, 2019). In addition, this method assumes that the exact mud weight conditions at the time of BO formation are known, whereas in practice the exact time of BO formation and thus the exact mud weight in the borehole are rarely known. The method also assumes that BOs are initiated by the bottom hole or other downhole tools during drilling, reaming, or run-in, do not change further thereafter, and there are no chemical or thermal effects on downhole stresses or strength at the borehole margin. Therefore, it should be noted that although the discussed BO-width method is supported by numerical and laboratory models under strictly controlled conditions, in practice it may have numerous sources of error or invalid assumptions. This leads to high uncertainties, which is why the majority of industry professionals and practitioners do not use this method. Moreover, through practical experience, they have found that the results of interpreting the BO width usually lead to a S_{Hmax} estimate that is significantly higher than that of other methods.

Therefore, rather than using BO width to determine an accurate value, it is considered more reliable to use the presence or absence of BOs in a borehole to constrain the S_{Hmax} magnitude. This is done by calculating the approximate minimum value of S_{Hmax} magnitude required for a BO to occur. Thus, the presence of BOs indicates that this threshold corresponds to a lower bound for the S_{Hmax} magnitude, while the absence of BOs indicates that this threshold represents an upper bound. An analogous procedure is used for DIFs. In the absence of more explicit data, well failure observations can thus serve as a supplement to, for example, the friction limit considerations discussed in the previous subsection. Furthermore, they can be used to validate numerical stress models and thus reduce the uncertainties of the model results.

2.1.6 Stress Information Database of Germany and Adjacent Regions

The orientation of the stress tensor is classically expressed by stress maps that show the orientation of S_{Hmax} . This parameter has been compiled systematically by the World Stress Map (WSM) Project following a quality ranking for the data that result from a wide range of stress indicators. For Germany and adjacent regions, Reiter et al. (2015, 2016) published the subset that has been integrated later

in the WSM database release 2016 (Heidbach et al., 2018). These data are public and available via the WSM website and its interface CASMO (Create A Stress Map Online www.world-stress-map.org/casmo).

The first compilation of stress magnitude data for Germany and adjacent regions has been published by Morawietz et al. (2020) including a newly developed quality ranking scheme for stress magnitude data. In this first database that is publicly available 568 data records are provided. To extend this database 429 HF tests were reanalysed in the greater Ruhr valley area and added to the new stress magnitude database. Detailed description and the data themselves are published by Kruszewski et al. (2022) following the quality assignment published by Morawietz et al. (2020).

Current activities focus on 183 stress magnitude data records derived from MHF and SR tests in eight boreholes in Northern Switzerland (NAGRA borehole campaign). These data are a unique data set of top quality and represent a benchmark of stress magnitude data. Since we participated with the measurement campaign in detail we are convinced – assuming that only boreholes are available to determine the stress state in the geological subsurface – that MHF in combination with SR tests are the best option. Design, execution and analysis should be carried out by experienced specialists. This is the best and only option to receive the best possible results of stress magnitudes that are absolutely essential for the calibration of geomechanical models. With reference to Desroches et al. (2021), we also pass on the recommendation to perform rebounding tests, which where appropriate to better constrain fracture closure pressure, among other things. This supports in particular the calculation of S_{Hmax} based on SR tests. It is also clear from the latter point that explicit expert knowledge based on experience is necessary, in particular for the determination of reliable S_{Hmax} magnitudes.

So far the stress magnitude data are available only as electronic supplements of the cited publications, but we are currently working on an update of the World Stress Map database in order to integrate also stress magnitude data records and make this data set available via the WSM website. Furthermore, we are currently expanding the CASMO service to also visualise the stress magnitude data on the stress map service of the WSM as well as pore pressure data in collaboration with the two complementary projects GoEffective and World Pressure Map.

2.1.7 Abbreviations

3-D	Three dimensional
ASR	Anelastic strain recovery
BO	Borehole breakout
DCDA	Diametrical core deformation analysis
DFIT	Diagnostic Fracture Injection Test
DIF	Drilling induced tensile fracture
DRA	Deformation rate analysis
DSA	Differential strain analysis
FBP	Formation breakdown pressure
FCP	Fracture closure pressure
FIT	Formation Integrity Test
FPP	Formation propagation pressure
HF	Hydraulic Fracturing
HTPF	Hydraulic testing of pre-existing fractures
ISIP	Instantaneous shut-in pressure (equals P_{si})
LOP	Leak-off pressure
LOT	Leak-Off test
MHF	Micro Hydraulic Fracturing
OC	Overcoring
WVA	Wave velocity anisotropy
XLOT	Extended Leak-off test
P_0	Pore pressure before pumping
P_b	breakdown pressure
P_f	Fluid pressure in the fracture
P_r	Reopening pressure
P_{si}	Shut-in pressure (equals ISIP)
P_{SR}	Re-Opening pressure during Sleeve Reopening
S_{Hmax}	Maximum horizontal stress
S_V	Vertical stress
S_{hmin}	Minimum horizontal stress
μ	Static friction coefficient
ρ	Rock density
S_1	Largest principal stress
S_2	Intermediate principal stress
S_3	Minimum principal stress
g	Gravitational acceleration
z	True vertical depth

2.2 Structural diversification of the geomechanical model for Germany

2.2.1 Introduction

The new geomechanical-numerical model of Germany has the same dimensions as the two previous versions of Ahlers et al. (2021, 2022) and also the workflow (Fig. 2.6) was essentially not changed (details see chapter 2.2.3). The main improvement is the implementation of 20 3-D geological models for a new stratigraphic subdivision of the sedimentary unit in the centre of the model (details see chapter 2.2.2), which was based before on the 3-D-Deutschland model (Anikiev et al., 2019). Following the workflow in Fig. 2.6, the first step, the creation of the model geometry has been completed. The result is a model with 93 formation interfaces, the topography, and the model base at 100 km depth. In total 155 units are defined by these 95 surfaces.

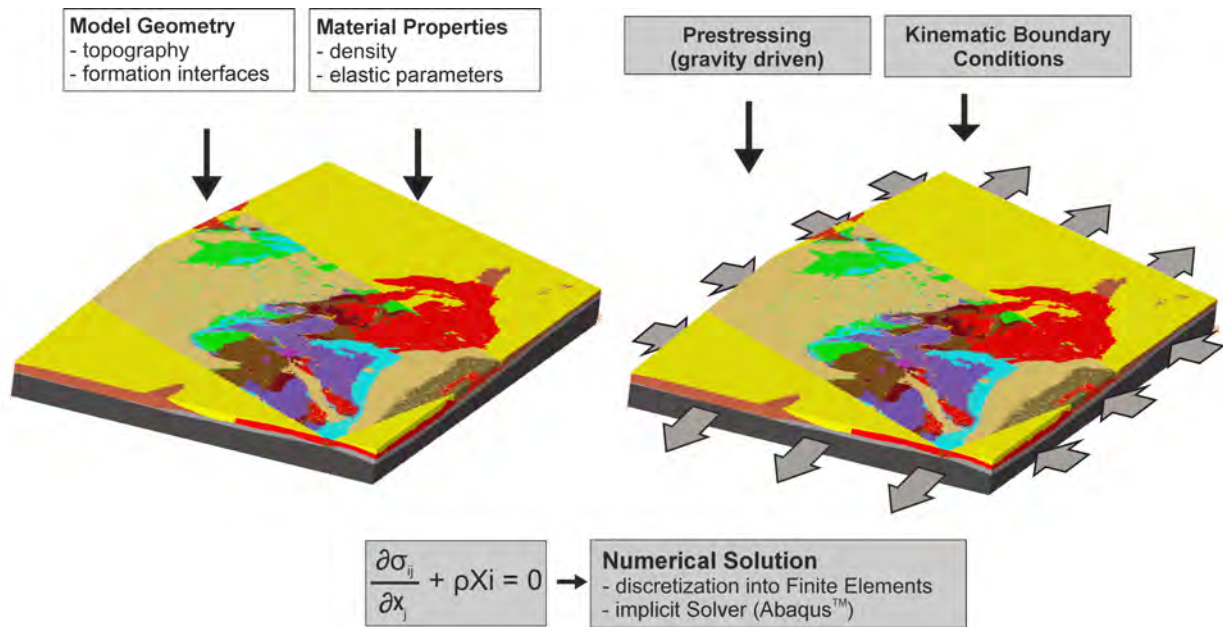


Figure 2.6: General workflow of 3-D geomechanical-numerical modelling. First, a model geometry is created, then it is discretized and parameterised with rock properties. An appropriate initial stress state is defined for the final model and then kinematic boundary conditions (right figure) are applied. The partial differential equation of the equilibrium of forces in 3-D is solved using the FEM: σ_{ij} stress tensor, x_j Cartesian coordinates, ρ density, and x_i body forces. (Ahlers et al., 2021)

2.2.2 Database

The model geometry is essentially based on 23 3-D geological models: Three large-scale models (Fig. 2.7, A-C) of Maystrenko and Scheck-Wenderoth (2013) (A), Anikiev et al. (2019) (B) and Tašárová et al. (2016) (C) and 20 smaller models (Fig. 2.7, 1-20). The three large-scale models

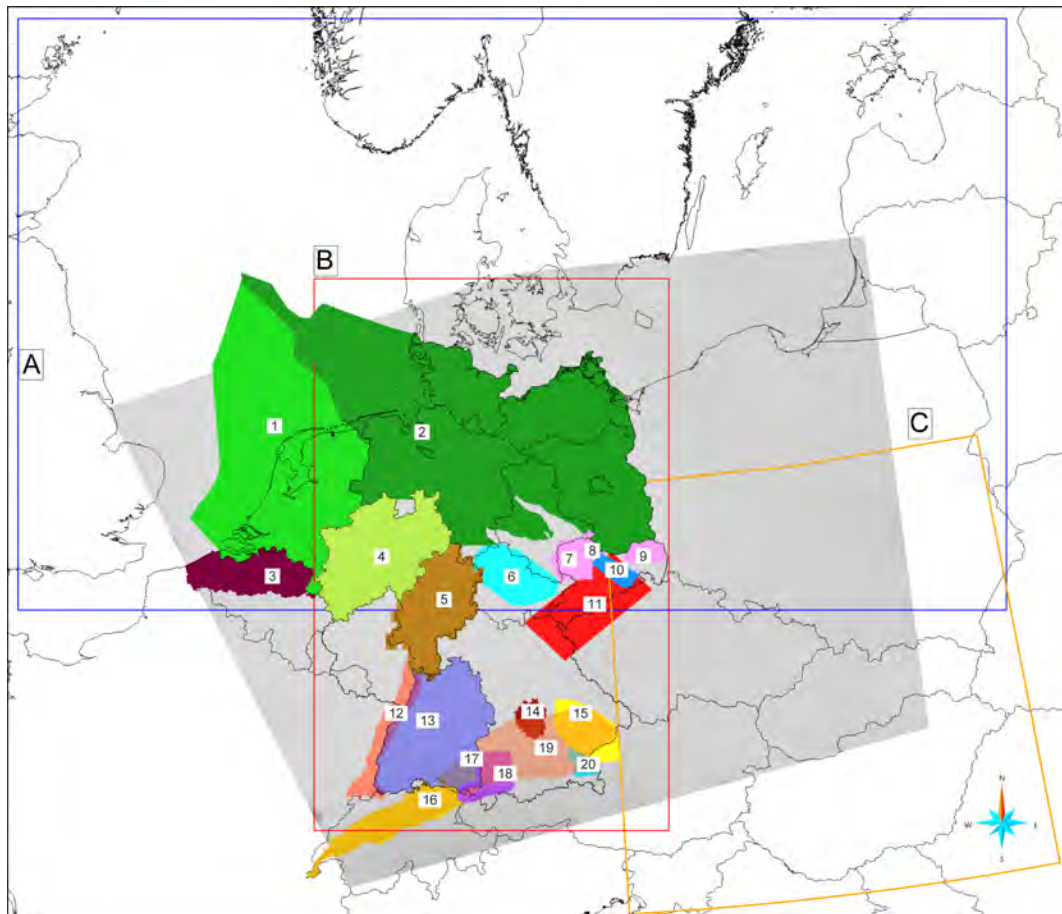


Figure 2.7: Overview of 3-D geological models implemented in the new geomechanical-numerical model: A: Central European Basin System model (Maystrenko and Scheck-Wenderoth, 2013), B: 3-D-Deutschland (Anikiev et al., 2019), C: Central Europe model (Tašárová et al., 2016); 1: DGM-Deep V5 on- and offshore (Geological Survey of the Netherlands, 2019), 2: TUNB (BGR et al., 2022), 3: G3Dv3 (Deckers J. et al., 2019), 4: NRW-Landesmodell (Geologischer Dienst Nordrhein-Westfalen, 2014), 5: Hessen 3D 2.0 (Bär et al., 2021), 6: 3-D model 'Thüringer Becken' (TLUBN, 2014), 7: Geological 3-D model 'NW-Sachsen' (Görne, 2011), 8: Geological 3-D model 'Zwischengebiet' (Görne, 2012a), 9: Geological 3-D model 'Niederlausitz' (Görne and Geißler, 2015), 10: Geological 3-D model 'Elbtalzone' (SLULG, 2012), 11: 3-D model of the Erzgebirge (Kirsch et al., 2017), 12: GeORG (GeORG-Projektteam, 2013), 13: Landesmodell Baden-Württemberg (Rupf and Nitsch, 2008), 14: Geological 3-D model 'Region Ingolstadt' (Ringseis et al., 2020), 15: Geological 3-D model 'Niederbayern' (Donner, 2020), 16: GeoMol geological model 2019 (Swisstopo, 2019), 17: GeoMol pilot area Lake Constance - Allgäu (Baden-Württemberg) (GeoMol LCA-Projectteam, 2015a), 18: GeoMol pilot area Lake Constance - Allgäu (Bavaria) (GeoMol LCA-Projectteam, 2015b), 19: GeoMol Framework model (Bavaria) (GeoMol Team, 2015), 20: GeoMol pilot area Upper Austria – Upper Bavaria (Bavaria) (GeoMol UA-UB-Projectteam, 2015).

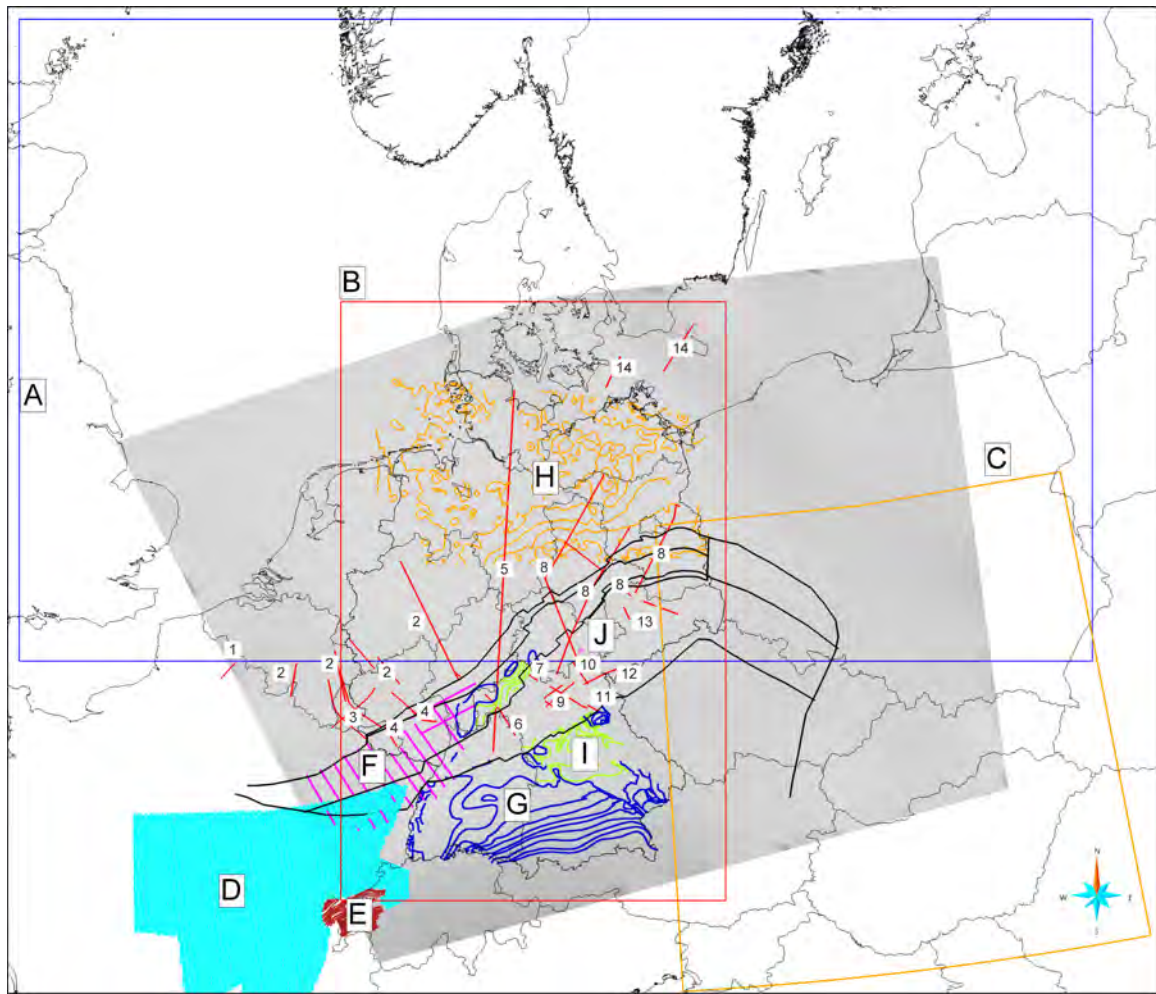


Figure 2.8: Data used for construction of the top of the crystalline basement: A: Maystrenko and Scheck-Wenderoth (2013), B: Anikiev et al. (2019), C: Tašárová et al. (2016), D: Hurtig et al. (1992), E: Sommaruga (1999), F: Korsch and Schäfer (1995), G: Reinhold (2005), H: Lindner et al. (2004), I: Bayerisches Landesamt für Umwelt (2022), J: Hrubcová et al. (2005). 1: Cazes et al. (1985), 2: Oncken et al. (2000), 3: Schintgen (2015), 4: Meschede and Warr (2019), 5: Blundell et al. (1992), 6: Reichert (1988), 7: Heinrichs et al. (1994), 8: Reinhold (2005), 9: Fazlikhani et al. (2022), 10: DEKORP Research Group (1987), 11: Guy et al. (2011), 12: DEKORP Research Group et al. (1994), 13: Enderle et al. (1998), 14: Bachmann et al. (1999), Variscan zones (bold black lines) based on Reinhold (2005), Linnemann and Romer (2010) and Prijac et al. (2000).

are mainly used for the deeper crustal structure, whereas the smaller models are used for the stratigraphic subdivision of the sedimentary unit. The area with a high stratigraphic resolution was extended beyond Germany to Switzerland, Netherlands and Flanders due to the availability of geological models and stress measurements which might be used for the final model calibration (e.g., TNO, 2014; NAGRA, 2001). In addition to these models further data were used for the topography (Danielson and Gesch, 2011), the bathymetry (GEBCO Bathymetric Compilation Group, 2022), the

north Bavarian part (Bayerisches Landesamt für Umwelt, 2022; Fazlikhani et al., 2022), the top of the lower crust (Gajewski et al., 1987; Grad et al., 2009b; Janik et al., 2011; Ustaszewski, 2004; Valasek and Mueller, 1997) and the Mohorovičić Discontinuity (Grad et al., 2009a; Wagner et al., 2012).

As for the previous models, an important task was the creation of the Top of the crystalline basement since this is an important mechanical boundary. However, it is often not resolved in the implemented models. All additional data used for this construction are displayed in Fig. 2.8.

2.2.3 Technical implementation

2.2.3.1 Stratigraphic correlation and unit definition

Due to the heterogeneous definition and implementation of formation interfaces within the models used, the first step was the correlation of equal defined formation interfaces. In total 93 formations have been chosen. These include almost all formation interfaces defined in the individual models, with a few exceptions, e.g., tectonic units from the Erzgebirgs model (Kirsch et al., 2017), whose stratigraphic correlation with other horizons is difficult. Together with the topography and the base of the model defined at 100 km depth, 75 horizons are defined in the final geometry model. Due to the spatial inhomogeneous resolution of the formation interfaces, a unit between two formation interfaces is not always defined equally. An example is shown by a sketch in Fig. 2.9: Model A contains three formation interfaces: Top of the Jurassic, Top of the Middle Jurassic and Base of the Jurassic, model B contains also two of these three formations interfaces (Top of the Jurassic, Base of the Jurassic), however 4 units are needed to define proper material properties later on: Upper Jurassic, Middle Jurassic, Lower Jurassic and an undifferentiated Jurassic unit. Therefore, 155 different units are defined in the final geometry model.

Model A	Model B
Upper Jurassic	Jurassic (undifferentiated)
Middle Jurassic	
Lower Jurassic	

Figure 2.9: Sketch: Definition of four units (blue boxes) by three formation interfaces (red bold lines). Detailed description see text.

2.2.3.2 Point cloud model

The next step after correlation is the build up of the model geometry. Due to the size of the model area, the inhomogeneous input data, and the task of keeping the model up to date with new data during the project, no 'classical' geometrical model was created, but only point clouds projected onto the input data. Exceptions are the Mohorovičić Discontinuity, Top of the Lower Crust and Top of the Crystalline Basement. The concept of this 'point cloud model' is explained below:

The first step is the creation of a point data set with a resolution of 1×1 km. This point data set is then projected onto a surface. The example in Fig. 2.9 (1) shows the projection onto topography. For an underlying formation interface (Fig. 2.10, yellow line), the data set projected onto the topography is copied and then projected onto the deeper formation interface. Afterwards, the projected data set is shifted 0.1 m downwards. This is necessary to avoid duplicate points that are defined at the same location but belong to different layers. This is not necessary if a layer is continuous (yellow layer), but it is necessary for layers where this is not the case, e.g. because they basset (orange layer). At the later model resolution (≈ 35 m vertical) a deviation of the point data set from the original layer surface of 0.1 m is negligible. An advantage of the used concept is that two overlapping models do not have to be cut, which can take several hours per formation interface depending on the model resolution. In such a case, the projection is staggered (Fig. 2.10 (3) and (4)). First, the copied point data set is projected onto the layer that has the lowest reliability, in this case the purple one (3), then in a second step the projection is done onto the more reliable layer, in this case the pink layer (4). The order of projection is determined according to various criteria, e.g. the year of publication, the model resolution, etc.

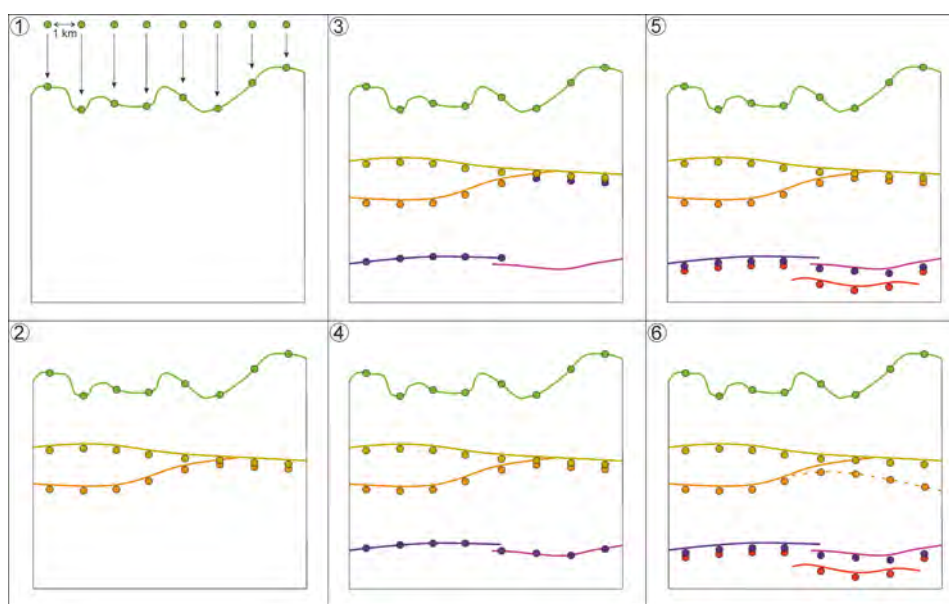


Figure 2.10: Concept of a 'point cloud model'. Detailed description see text.

Another advantage is the integration of models that contain only locally occurring layers or resolve layers that are not defined in other models (Fig. 2.10 (5)). In such a case, information can be taken over 1 to 1, which can be an advantage for a further use of the geological model for sub-models. The biggest advantage of the 'point cloud model', however, is the possibility to quickly integrate new or changed data into the existing model. Fig. 2.10 (6) shows the example of an adapted layer (dashed orange line). In such a case, the existing point data set can be re-projected. Afterwards, any overlaps with underlying point data sets are checked with a script and adjusted if necessary.

2.2.4 Outlook

The next step is the grouping of units based on mechanical properties and on their thickness distribution, since a unit can only be fully represented mechanically in the model if there are at least three element layers. The number of units that will be parameterised with individual units in the final model is probably 50. The following steps correspond to the workflow (Fig. 2.6). First, the model is discretised and then parameterised. Then an initial stress state is defined, and the final calibration is performed using stress data. The expected resolution of the model will be $4 \times 4 \text{ km}^2$ laterally and up to $\approx 35 \text{ m}$ vertically (Tab. 2.1). The lateral resolution will be homogeneous throughout the model and vertical resolution will decrease with depth. In total, the discretised model will contain 13 million hexahedral elements and will require $\approx 2 \text{ TB}$ of RAM.

Table 2.1: Planned model dimensions.

Lateral resolution	$4 \times 4 \text{ km}^2$
Vertical resolution	min. 35 m (increasing with depth)
Rock units	50
Elements (Hexahedral)	13,000,000
Used RAM	2 TB

2.3 Slip Tendency Analysis

2.3.1 Material

The fault reactivation potential assessment is conducted using 3D fault geometries from 3D geological models and stress results from the geomechanical-numerical model of Germany by Ahlers et al. (2022). The fault geometries are taken from several geological models. A list of models used for the fault reactivation potential assessment is given in Tab. 2.2. The faults provided by the models are shown in Fig. 2.11.



Figure 2.11: Map view of all the faults available in the models of the federal states.

Table 2.2: Listing of available geological models and the areas they cover.

Model	Covered Area	Source
3-D Model des Erzgebirges	Ore Mountains, Fichtel Mountains, Vogtland	Kirsch et al. (2017)
Geologisches Landesmodell Baden-Württemberg	Baden-Württemberg	Rupf and Nitsch (2008)
GeoMol Baden-Württemberg	South-east Baden-Württemberg	GeoMol LCA-Projectteam (2015b)
GeoMol Bayern	South Bavaria	Diepolder et al. (2015)
GeoORG	Upper Rhine Graben	GeORG-Projektteam (2013)
Hessen 3-D	Hesse	Bär et al. (2021)
Modelle des Tiefen Untergrundes Sachsen	Saxony	Domínguez-Gonzalez and Andreani (2013), Domínguez-Gonzalez and Andreani (2015a), Domínguez-Gonzalez and Andreani (2015b), Domínguez-Gonzalez and Andreani (2015c), Domínguez-Gonzalez and Andreani (2015d), Görne and Steinborn (2007), Görne (2010a), Görne (2010b), Görne (2012a), Görne (2012b), Görne and Steinborn (2014), Görne and Wener (2015), Kogan et al. (2009), Unger and Rommel (2020), Unger and Thiele (2020)
TUNB	Brandenburg, Bremen, Mecklenburg- Western Pomerania, Lower Saxony, Saxony-Anhalt, Schleswig-Holstein	BGR et al. (2022)
Thüringer Becken Modell	Thuringia	TLUBN (2014)

The fault data are available in the GOCAD format (.ts). For some models, each fault geometry has been stored in a separate file. For a subset of these faults, the names of the faults are used in the file name. This allows the identification of every single one of these faults, for example if the reactivation potential of a specific fault is of interest. However, not for all faults names have been defined in the file names or elsewhere. In these cases, there is no identification of the faults possible besides by location and geometry.

Fairly large parts of Germany are covered by geological models, but there are still some major blank areas on the map. Areas without fault data include Rhineland-Palatinate, Saarland and northern Bavaria. Furthermore, while there are faults available for all of Baden-Württemberg provided by the *Landesmodell Baden-Württemberg*, these faults only extend vertically and do not reflect the true geometry of the faults. The faults are included in the fault reactivation potential calculation, but not considered in the subsequent analysis. Some sub-regions of Baden-Württemberg are covered by the *GeORG* and *GeoMol* models.

While for some areas no models are available at all, some areas are covered by multiple models. This is particularly true for the parts of northern Germany that are covered by the *TUNB* model. While other models such as the *GTA3D* model are available for parts of this area, only the *TUNB* geometries are used. This is in order to avoid having multiple geometries for the same faults. Since the faults in the *TUNB* model are not individually named, a comparison on name basis with other models is not possible. As the *TUNB* model, published in 2021, is very recent it has been chosen as the default model for North Germany. The *3D Modelle des Erzgebirges* model covers the same area as parts of the *Modelle des Tiefen Untergrundes Sachsen* model. Since for both models each fault is named individually, a comparison between the two fault sets is possible. Duplicate faults have been removed. In case of differing geometries, the spatially more extensive one was retained.

2.3.2 Slip Tendency Calculation

The provided fault geometries are converted from the *.ts data type to the *Abaqus*TM input file format that is required for the slip tendency calculation in the *GeoStress* add-on (Heidbach et al., 2020) for *Tecplot 360 EX*TM. During this conversion, files containing multiple faults are split into files containing only one single fault, a transformation to UTM32N is performed for faults with different systems and all faults are remeshed to have a uniform element size of 200 m. This step is important to ensure that faults or segments with a very fine resolution will not be over-represented in the subsequent analysis. Finally, some minor adjustments are made to the *.inp files to assure their compatibility with *GeoStress*. In order to automate the slip tendency calculation in *GeoStress*, a script in *Matlab* was written that generates a macro for the calculation of the slip tendency of every fault file. The entire process of the slip tendency calculation is set up in a semi-automatic way that only requires the manual transfer of files and the manual start of the different scripts and programs. With these scripts the quick calculation of the slip tendency of any new fault geometries in the commonly used *GoCAD* file format or with the improved stress model is possible. The workflow is visualized in Fig. 2.12.

The *GeoStress* add-on calculates the normalised slip tendency by mapping the stresses of the model onto the faults, calculating the shear and normal stresses τ and σ_n using the respective fault geometries and by normalising the resulting slip tendency to a predefined friction angle. However, since there are basically no friction data available for the highly diverse faults, a normalisation to a friction angle is not advisable in the given case. Instead, the influence of the pore pressure on the slip tendency is considered. Since the Germany model does not include pore pressure and pore pressure data in Germany are generally not widely available, the pore pressure (p_0) throughout Germany is assumed to be hydrostatic and calculated by Eq. 2.3, where g is the gravitational acceleration, ρ is the density of the water ($\rho = 1000 \text{ kg/m}^3$) and TVD is the true vertical depth. The effective normal stress (σ'_n) is calculated by Eq. 2.4. Finally, the slip tendency factoring in the pore pressure (T_{Seff}) is calculated by Eq. 2.5.

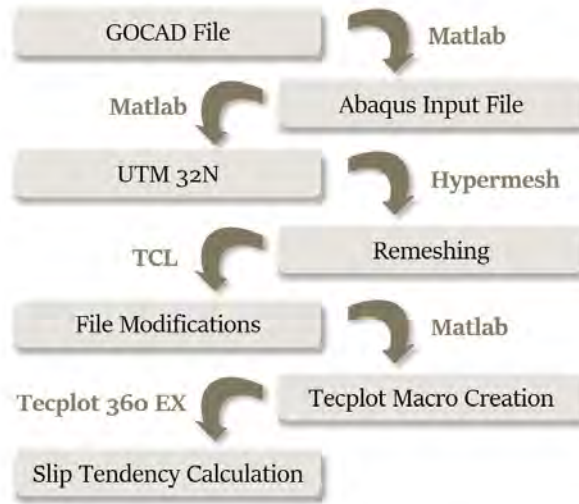


Figure 2.12: An overview over the workflow transforming the original fault geometries in the GOCAD file format to *.txt files in an Abaqus™ input file format style using the ETRS 1989 UTM32N coordinate system for the slip tendency analysis in Tecplot 360 EX™.

$$p_0 = TVD \cdot \rho \cdot g \quad (2.3)$$

$$\sigma'_n = \sigma_n - p_0 \quad (2.4)$$

$$T_{Seff} = \frac{\tau}{\sigma'_n} \quad (2.5)$$

2.3.3 Results and Discussion

An overview of the resulting T_{Seff} is given in Fig. 2.13, where the available faults are colour-coded by their respective T_{Seff} values. T_{Seff} ranges mainly between 0 and 0.7 peaking at values of 1 and greater. As the results are not normalised to a friction angle or coefficient of static friction, it is important to keep in mind that the results only allow for a comparison between different regions and faults. However, a conclusion on the absolute reactivation potential cannot be drawn from the values of the slip tendency without normalisation. For example, a fault with a T_{Seff} value of 0.5 would be considered to be likely reactivated if its coefficient of static friction was 0.4 but it would be considered stable if its coefficient of static friction was 0.7. Furthermore, the currently used Germany model is intended to be a stepping stone in a sequence of models of increasing resolution. The more local models will provide a more accurate prediction of the stress state and will therefore improve the reliability of the slip tendency prediction.

Four regions were chosen for a more detailed analysis that are indicated in Fig. 2.13: the Upper Rhine Graben (URG), the North German Basin (NGB), Saxony and the Ore Mountains and the Molasse Basin. A summary of the characteristics of these regions is provided in the following sub-chapters.

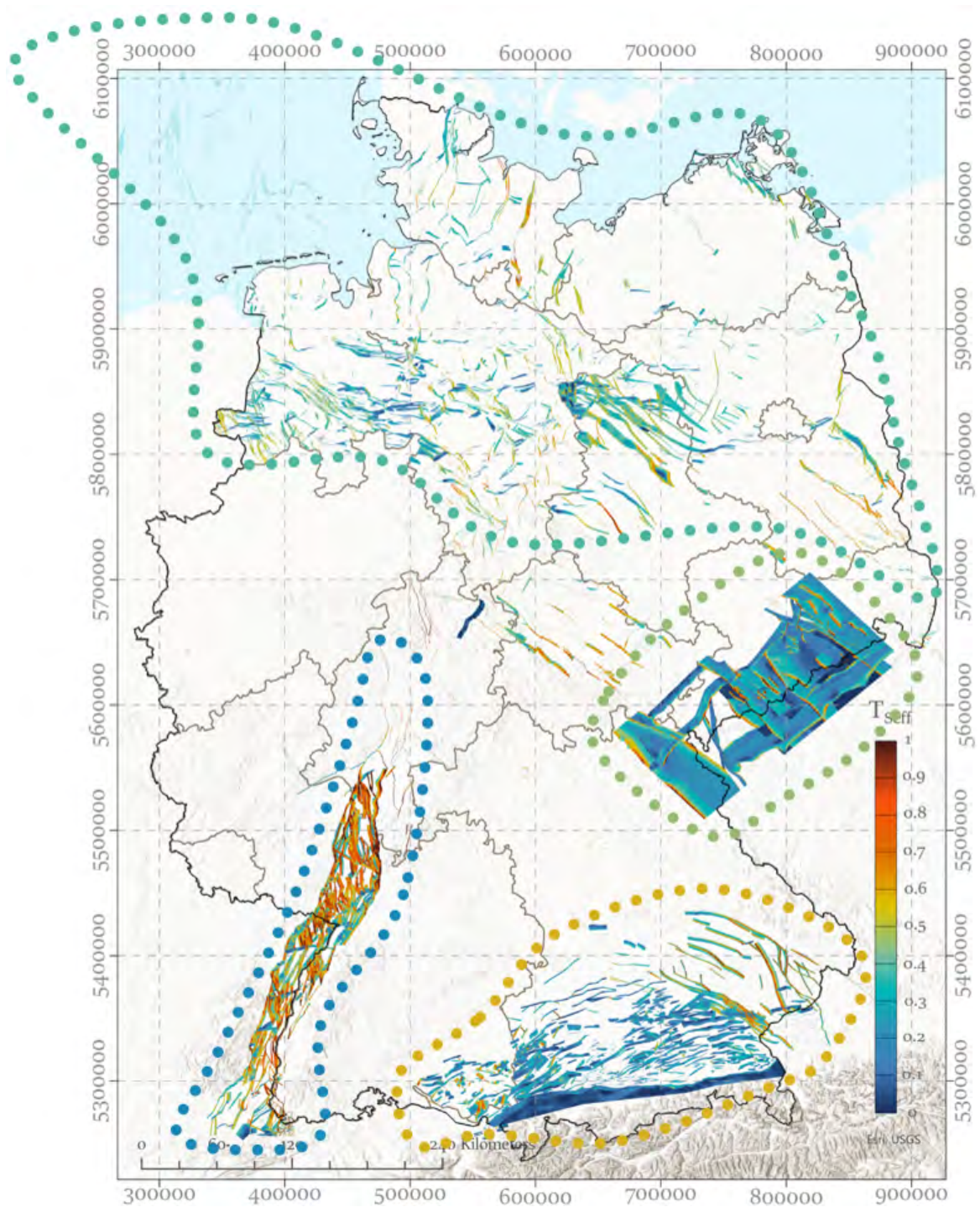


Figure 2.13: The faults of the federal state models are displayed in a top down view and colour-coded by their T_{Seff} . Vertical faults, such as the ones in the *Landesmodell Baden-Württemberg* do not show up in this view. The dotted lines indicate the sub-regions, shown in Figs. 2.14, 2.15, 2.16 and 2.17.

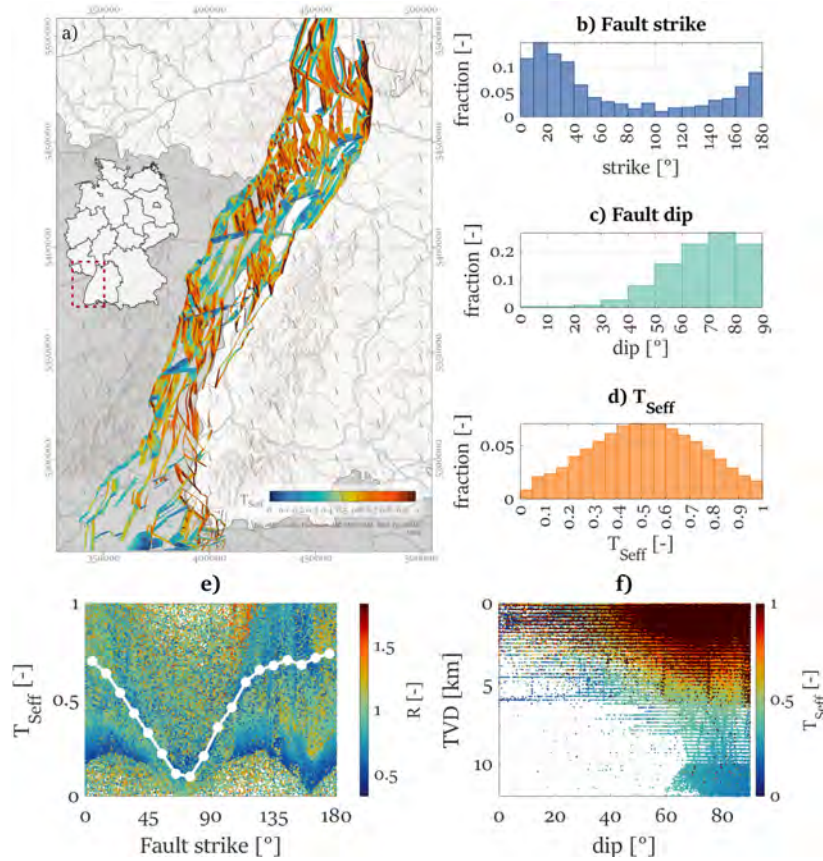


Figure 2.14: a) The map shows the faults of the GeORG model color-coded by their T_{Seff} value. Additionally, S_{Hazi} is indicated by the rotated line symbols. The line symbols are color-coded by the S_{Hazi} value; b) Histogram of the fault strike of the GeORG faults; c) Histogram of the fault dip of the GeORG faults; d) Histogram of the T_{Seff} values of the GeORG faults; e) Scatter plot showing T_{Seff} as a function of fault strike for the GeORG faults, the white line indicates the median of T_{Seff} ; f) Scatter plot showing fault dip with depth (TVD) color-coded by T_{Seff} for the GeORG faults.

2.3.3.1 Slip tendency of the Upper Rhine Graben

For the URG, 640 faults of the GeORG model have been analysed and are shown in Fig. 2.14 a. The faults of the GeORG model mainly strike in N–S to NNE–SSW and NNW–SSE direction (Fig. 2.14 b) and dip relatively steeply with dips mainly ranging between 60° and 90° (Fig. 2.14 c). The URG is the region with the overall highest fault reactivation potential. The histogram of the T_{Seff} values in this region shows a symmetric distribution of values with a peak for $T_{Seff} = 0.5$ (Fig. 2.14 d), indicating an overall high reactivation potential for this area when compared to the other regions.

T_{Seff} is the overall highest for N–S striking and NW–SE to NNW–SSE striking faults. Fig. 2.14 e shows T_{Seff} as a function of the fault strike. Plotted alongside is the median T_{Seff} in 10° strike intervals. For faults with the aforementioned strikes, the median T_{Seff} exceeds 0.6. In contrast, faults striking in ENE–WSW to E–W direction show the overall lowest reactivation potential in the URG region with a median T_{Seff} lower than 0.2. Comparing Fig. 2.14 b and e the overall high predicted

reactivation potential of the URG can at least in part be easily explained by the fact that in the URG most faults are striking in a (sub-) optimal direction for fault reactivation.

T_{Seff} overall decreases with increasing depth as shown in Fig. 2.14 f. The Fig. scatters the true vertical depth (TVD) of the data points against the dip of the respective data points. The plot is color-coded by T_{Seff} , illustrating which dip angles are especially susceptible to fault reactivation. The overall T_{Seff} is considerably higher in the uppermost 6 km than in the deeper parts. The range of fault dips in which T_{Seff} values of 0.6 and higher commonly occur decreases from 40–90° in the topmost 2 km to 60–90° at 6 km depth. At deeper depth, faults almost exclusively dip with 60°–90°.

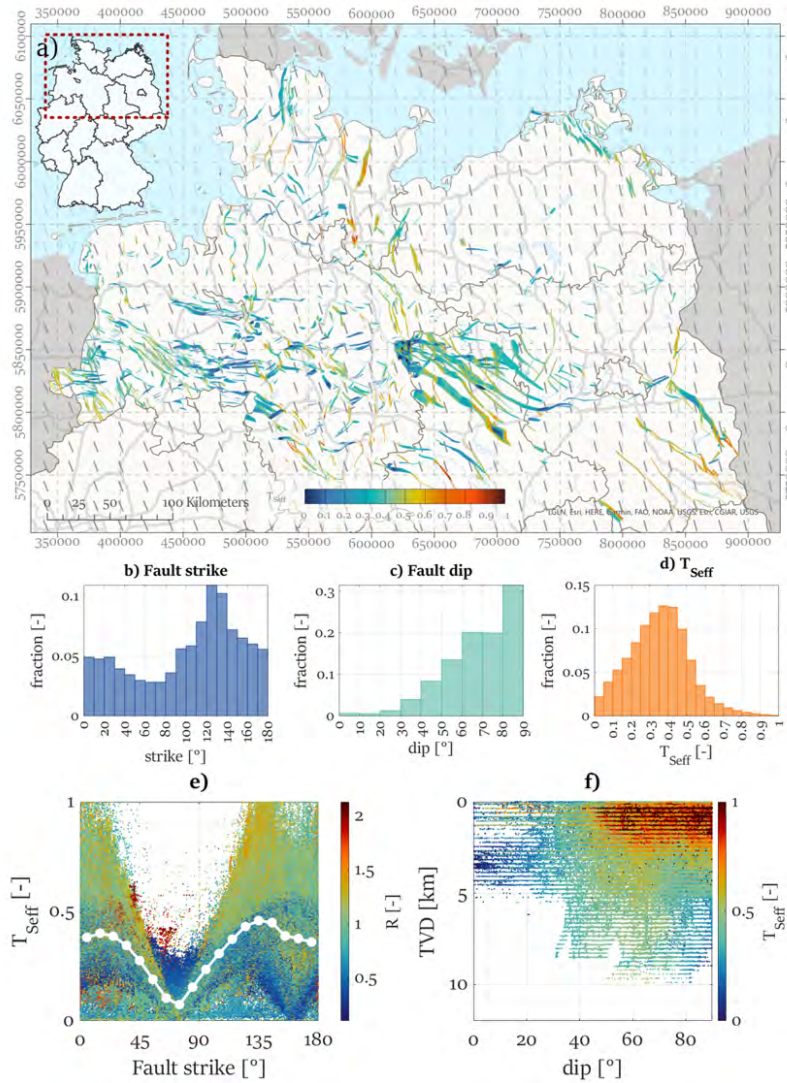


Figure 2.15: The map shows the faults of the *TUNB* model color-coded by their T_{Seff} value. Additionally, S_{Hazi} is indicated by the rotated line symbols; b) Histogram of the fault strike of the *TUNB* faults; c) Histogram of the fault dip of the *TUNB* faults; d) Histogram of the T_{Seff} values of the *TUNB* faults; e) Scatter plot showing T_{Seff} as a function of fault strike for the *TUNB* faults, the white line indicates the median of T_{Seff} ; f) Scatter plot showing fault dip with depth (TVD) color-coded by T_{Seff} for the *TUNB* faults.

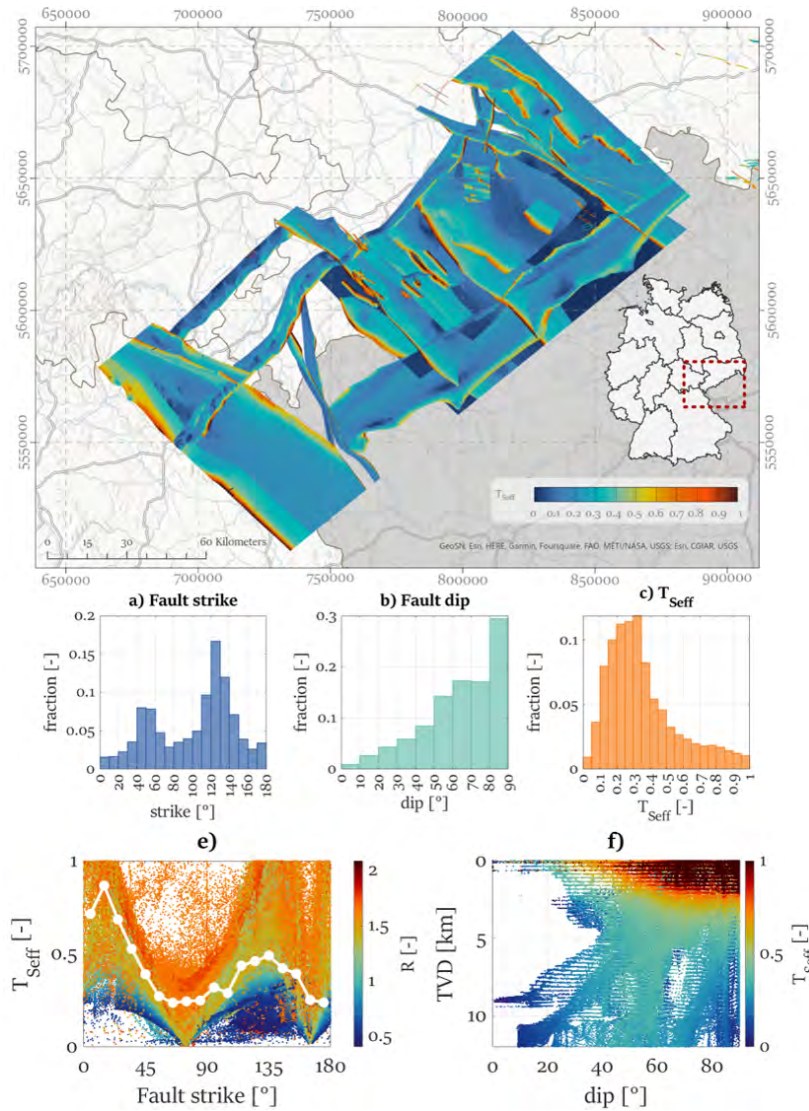


Figure 2.16: The map shows the faults of the Saxony & the Ore Mountains model color-coded by their T_{Seff} value. Additionally, S_{Hazi} is indicated by the rotated line symbols; b) Histogram of the fault strike of the Saxony & the Ore Mountains faults; c) Histogram of the fault dip of the Saxony & the Ore Mountains faults; d) Histogram of the T_{Seff} values of the Saxony & the Ore Mountains faults; e) Scatter plot showing T_{Seff} as a function of fault strike for the Saxony & Ore Mountains faults, the white line indicates the median of T_{Seff} ; f) Scatter plot showing fault dip with depth (TVD) color-coded by T_{Seff} for the Saxony & Ore Mountains faults.

2.3.3.2 Slip tendency of the North German Basin

An overview over the T_{Seff} in the NGB is given in Fig. 2.15 a. The strike pattern in the NGB is more diverse than in the URG with a majority of faults striking in NW–SE direction and secondarily striking in NNW–SSE to NNE–SSW direction (Fig. 2.15 b). The majority of faults dips between 60° and 90°

with less than 20% of faults showing a shallower dip (Fig. 2.15 c). The histogram of the T_{Seff} values (Fig. 2.15 d) shows a right-skewed bell shape peaking at a T_{Seff} value of 0.35. Only very few fault segments reach a T_{Seff} of 0.6 and higher, indicating an overall considerably lower fault reactivation potential for the NGB than for the URG, which fits to the observed seismicity. Faults striking in NW–SE direction show the overall highest median T_{Seff} (Fig. 2.15 e), followed by NNW–SSE to NNE–SSW striking faults. ENE–WSW striking faults have the overall lowest median T_{Seff} values. T_{Seff} values of 0.6 and higher mainly occur above 4 km. Between 6 and 10 km depth, the median T_{Seff} increases again, mainly due to the fact that fewer very low T_{Seff} values occur in this depth range than at shallower depths. The optimal dip angle for fault reactivation shifts from 50–90° in the topmost 2 km to 45–70° between 3 and 6 km depth (Fig. 2.15 f). However, results for greater depth are uncertain, as fault orientation is less diverse there.

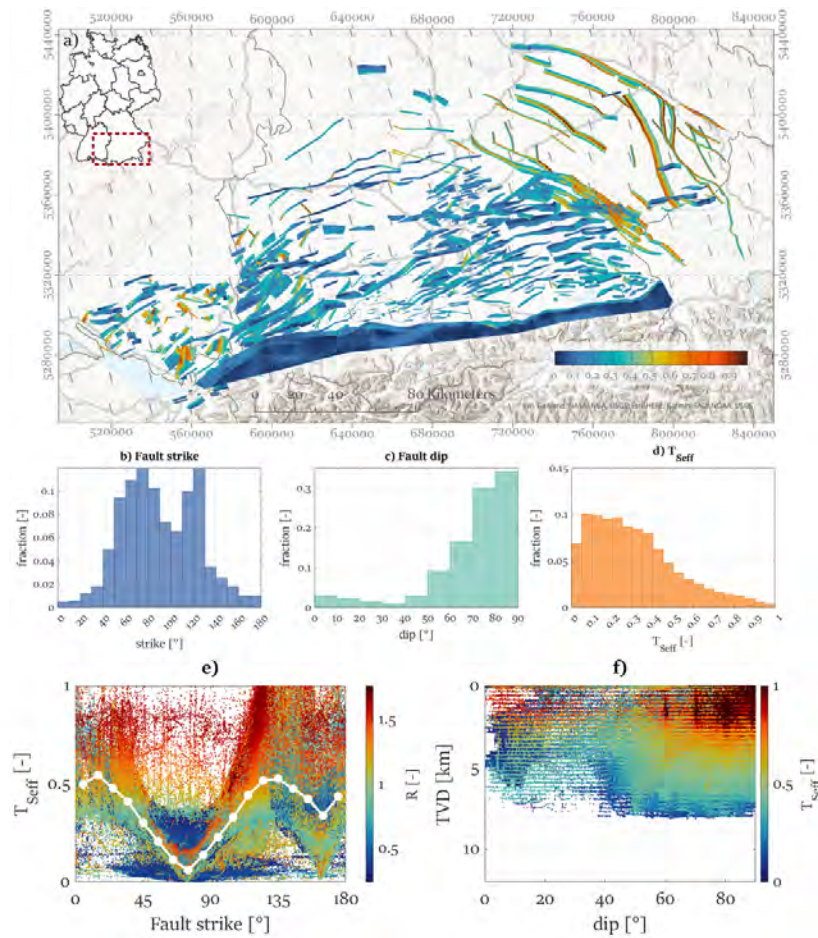


Figure 2.17: The map shows the faults of the Molasse Basin color-coded by their T_{Seff} value. Additionally, S_{Hazi} is indicated by the rotated line symbols; b) Histogram of the fault strike of the Molasse Basin faults; c) Histogram of the fault dip of the Molasse Basin faults; d) Histogram of the T_{Seff} values of the Molasse Basin faults; e) Scatter plot showing T_{Seff} as a function of fault strike for the Molasse Basin faults, the white line indicates the median of T_{Seff} ; f) Scatter plot showing fault dip with depth (TVD) color-coded by T_{Seff} for the Molasse Basin faults.

2.3.3.3 Slip tendency of Saxony & the Ore Mountains

An overview over T_{Seff} of the Saxony and Ore Mountains faults is given in Fig. 2.16 a. Subfigures b to f only contain data up to depths of 12 km to ensure consistency with the other regions where faults have only been implemented to a maximum depth of 12 km and to avoid distortion of the statistic results due to the very large, subhorizontal detachment at 16 km depth.

The two predominant strike directions of the faults are NE–SW and NW–SE (Fig. 2.16 b) and 30% of faults dip at around 90° with another 50% dipping between 50° and 80° (Fig. 2.16 c). Similarly to the NGB, the histogram of the T_{Seff} values (Fig. 2.16 d) shows a right-skewed bell shape peaking at a T_{Seff} value of 0.35. N–S to NNE–SSW striking faults show the highest fault reactivation potential in this region with the median T_{Seff} peaking at almost 1 for $10\text{--}20^\circ$ striking faults. For Saxony and the Ore Mountains, T_{Seff} is considerably higher for the N–S to NNE–SSW striking faults than for the NNW–SSE striking faults (Fig. 2.16 e). This is a unique feature of the Saxony and Ore Mountains region when compared to the other regions. T_{Seff} is the highest within the uppermost 2 km for $50\text{--}90^\circ$ dipping faults and overall decreases with increasing depth. Furthermore, the optimal dip range for fault reactivation shifts to $30\text{--}60^\circ$ with increasing depth (Fig. 2.16 f).

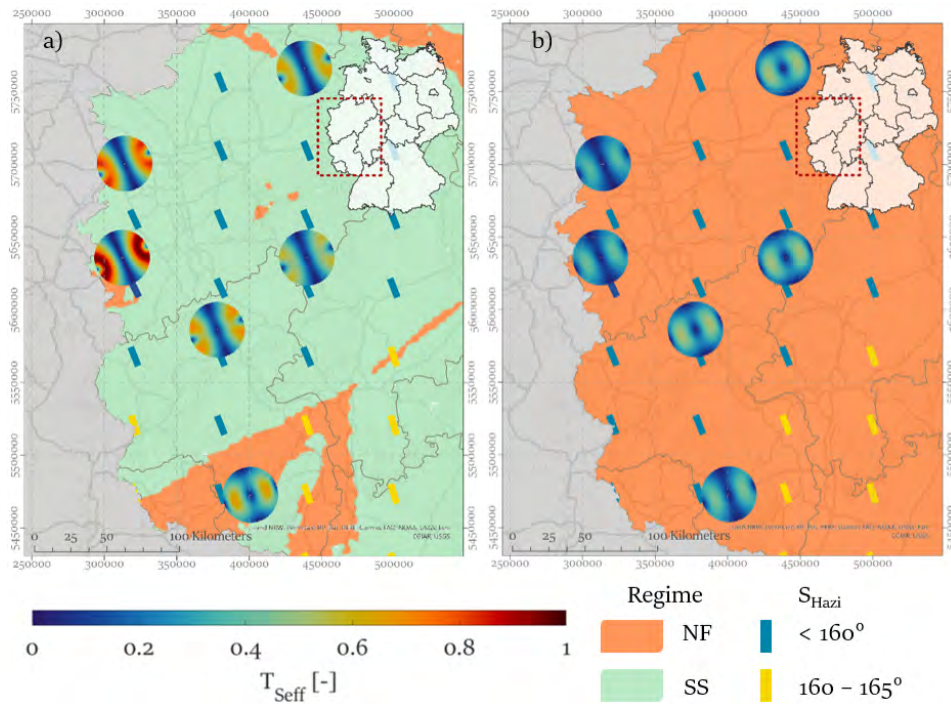


Figure 2.18: Stereoplots of the potential at a) 2000 m and b) 8000 m depths for the Rhineland-Palatinate and North Rhine-Westphalia area are plotted at the location where the stress data for the calculation has been picked. The stress regime is indicated by the orange or green shading and S_{Hazi} is shown by the rotated bars.

2.3.3.4 Molasse Basin

An overview over the T_{Seff} of Molasse Basin faults is given in Fig. 2.17 a. There are two dominant general strike directions present with most faults in the western and central parts of the Molasse Basin striking in NE–SW to ENE–WSW direction and the majority of faults in the eastern part striking in NW–SE direction (Fig. 2.17 b). The dip of the faults in the Molasse Basin in general is quite steep with a majority of faults dipping between 70° and 90° (Fig. 2.17 c).

Faults striking in NNE–SSW and NW–SE direction show the overall highest median T_{Seff} with values at 0.5 (Fig. 2.17 e). In these directions, R values (defined as S_1/S_3) mainly are in excess of 0.7. ENE–WSW striking faults have the overall lowest median T_{Seff} values. The R values for faults of this strike mainly range between 0 and 0.5. T_{Seff} values of 0.6 and higher mainly occur within the uppermost 4 km with the overall T_{Seff} strongly decreasing from 2 km TVD downwards (Fig. 2.17 f).

2.3.3.5 Areas without sufficient fault data

For the federal states of Saarland, Rhineland Palatinate and North Rhine Westphalia as well as parts of Baden-Württemberg and Bavaria no reliable fault geometries are available. For these areas slip tendency stereoplots can be calculated. These plots show the slip tendency under a given stress state for every possible strike and dip combination. The strike/dip combination is represented by the fault normal, and the slip tendency is represented by the colour-code of the plot. These plots allow to identify, not only the magnitude of the reactivation potential of different areas but also the most critical fault orientations and dips in these areas. Examples of such plots are shown in Fig. 2.18 for Saarland, Rhineland Palatinate and North Rhine Westphalia.

3 Development of the submodelling workflow (AP2)

3.1 Development of submodelling techniques to link different model scales

3.1.1 Purpose and challenges of submodelling

The large-scale Germany model (Ahlers et al., 2021, 2022) developed within the SpannEnD project integrates available stress information and provides a first-order prognosis on the 3D stress state in the subsurface of whole Germany. In the course of analysing the geomechanical suitability of particular regions of Germany or of specific candidate sites for a repository for nuclear waste it is advantageous to use the results from the Germany model as stress data are generally sparse. This implies that stress from a larger-scale model needs to be transferred to a smaller-scale model, and the technique to accomplish this task is submodelling.

Finite element software packages offer a standardised concept of submodelling that can be applied in two different ways. The first option is to extract the modelled displacements in the larger-scale model at the location of the boundary nodes of the small-scale model and use these displacements as boundary conditions to drive the small-scale model. This implies that in the first place only the displacement field of the large-scale model is transferred to the small-scale model which indirectly considers stress directions but not absolute stresses. This approach has been successfully used to model the velocity field, stress orientations and tectonic regime in areas of high tectonic activity such as northwest Anatolia (Hergert and Heidbach, 2010) and eastern Tibet (Li et al., 2021). However, in areas of low deformation rates this approach is not properly applicable as uncertainties of deformation rates are often greater than the deformation rates themselves and cannot be expected to represent remanent stresses from the geological history. In the second option the stress field resulting from the large-scale model is extracted at the location of the boundaries of the small-scale model and these stresses are applied as loads acting on the boundary faces of the small-scale model. Thus, actual stresses are transferred between the models. However, this approach has turned out problematic for models in geoscience context where on a large-scale an equilibrium of gravity and tectonic forces needs to be found.

Transferring stress consistently between models in geoscience context involves several challenges that are not addressed in the outlined standard approaches. In general, the small-scale model has higher numerical resolution (i.e. smaller element size) than the large-scale model but it also comprises more detail of the lithological units (i.e. more units with variable rock parameters). For example, the Germany model considers Jura as one single unit whereas a local model would discriminate the limestone dominated units of the Upper Jura from clay bearing units in the Middle Jura. Particularly important is that the stiffness of units containing stress magnitude data for calibration are both represented in the large-scale and small-scale model.

3.1.2 Submodelling technique for consistent stress transfer between models

The herein addressed submodelling procedure is to create two successively calibrated models – one large-scale model with coarse resolution (root model) and one local model with fine resolution (branch model). Fig. 3.1 gives a schematic impression of the approach and the assignment of terms. Structural features and stress magnitude measurements recorded during further exploration of the target area can be implemented into the model due to the simplified mesh regeneration. Even a new target area within the root model space can be implemented in the workflow easily by introducing an additional branch model. One root model may include several target areas and can therefore be reused for more than one project.

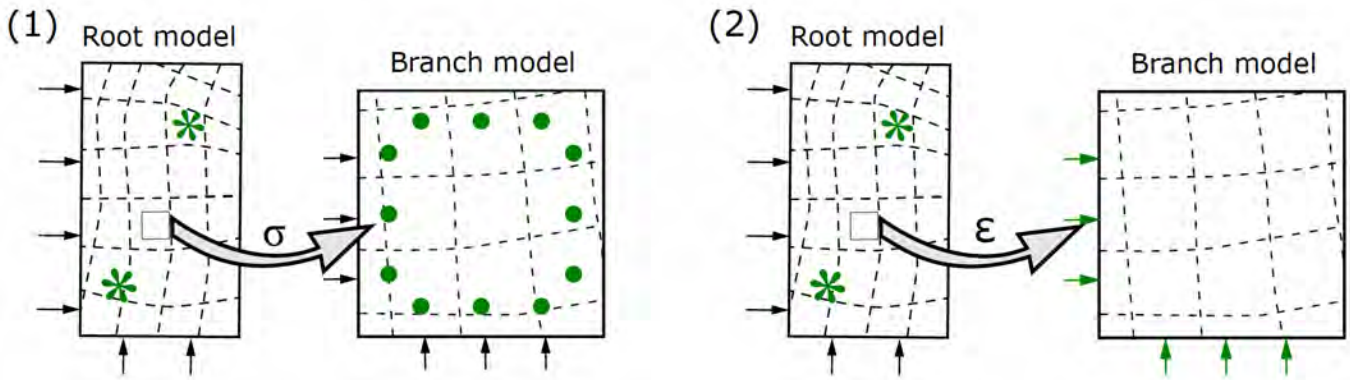


Figure 3.1: Clarification of the terms root model and branch model as well as the competing calibration approaches. Stress measurement data is available only in the root model (star symbols). For the calibration of the branch model, which covers a section of the root model area, either (1) synthetic data is used extracted from the result of the root model calibration (dots) or (2) the displacements (arrows) applied to the model boundaries are downscaled according to the reduced edge length of the model space.

The remaining question how to make the data from the large model space usable for the local model is investigated here. Aim of the work documented in the following is to address this question by systematically investigating to what extent the transfer of boundary conditions from large and coarse models to smaller-scale models with finer resolution via (1) the calibration on synthetic data obtained through the root model calibration is equally valid or in certain cases superior to (2) simple downscaling of the displacements determined by the model-scale ratio. These two competing techniques (Fig. 3.1) are compared for their implications and results in this study.

As a basis for the investigations, we use the tool FAST Calibration (Ziegler and Heidbach, 2021) that offers both an automatic calibration of the stress state and a basic submodelling approach. However, we improve the available tool by an implementation of a “lithology-check”. This is required to ensure that the lithologies in the root model and branch model at the location and depths of a synthetic calibration point are actually identical. Only then, the submodelling approach is valid and can be applied. This extension to the tool will be part of the upcoming new version of FAST Calibration.

In order to compare the accuracy of the different multistage calibration approaches, the results of the FAST multistage tool on the one hand and a simple downscaling of the displacement magnitude

to the size of the branch model on the other hand are each compared to the result of a fully resolved regional reference model (Fig. 3.2).

The modelling results show differences in stress magnitudes of ≤ 2.1 MPa or $< 2.3\%$, which is in all cases negligibly small considering the expected uncertainties introduced by influences and unknowns in cases of real measurement and model conditions, which mean considerably larger uncertainty ranges. The maximum differences between the model results A and B are smaller than the respective differences between the reference model ref and the results of A and B respectively. This is a result of analogous boundary effects since the results of the two multistage approaches behave very similarly near the edges of the branch model area. This shows that the FAST multistage approach works at least equivalently well to an expansion-scaled displacement transfer. Quantitatively, the FAST approach is even superior, with consistently smaller deviations to a reference scenario compared to the downscaling approach.

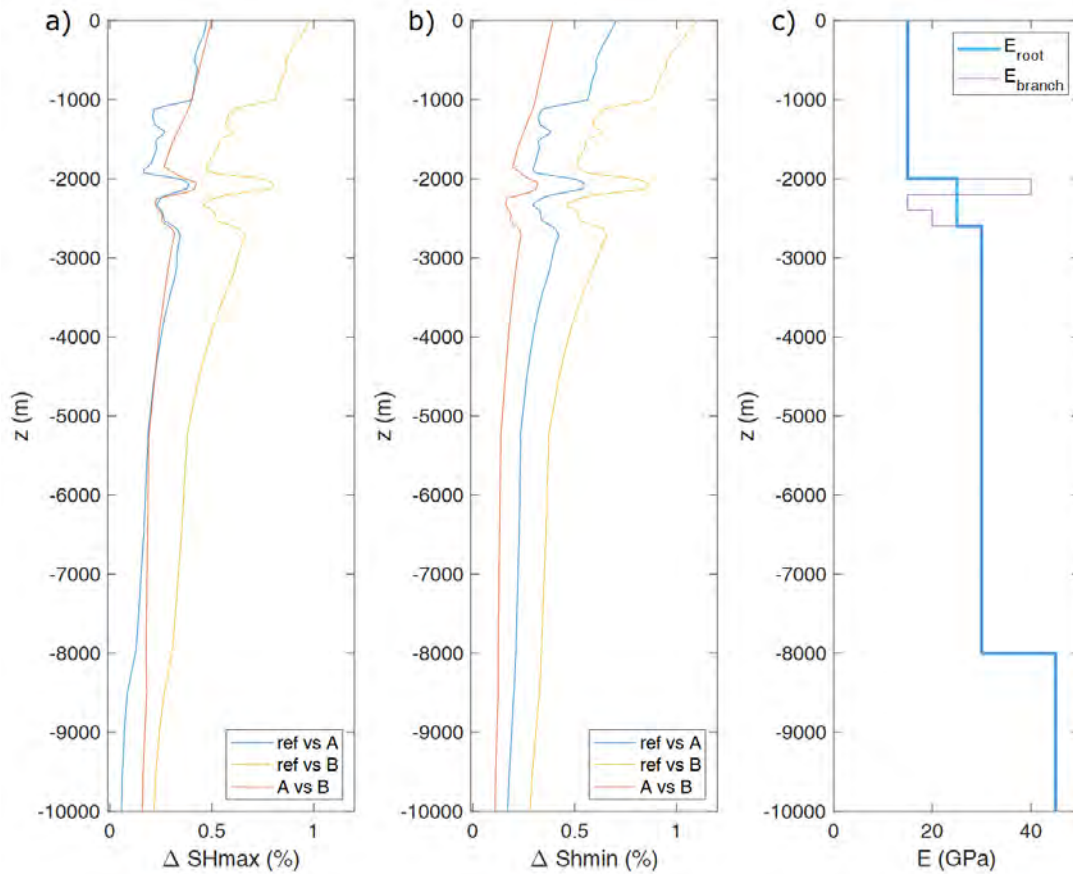


Figure 3.2: Vertical profile of relative stress differences between the fully resolved reference model (ref) and the results of the FAST multistage calibration approach (A) and the displacement transfer from a coarser root model (B) at the X-Y-position at the centre of the model extension ($X=0$ m, $Y=0$ m). The relative differences are generally decreasing with depth. The influence of the deviations in Young's modulus between the root and the branch model is evident in all curves. a) Differences in S_{Hmax} magnitude. b) Differences in S_{hmin} magnitude. c) Variation of the Young's modulus with depth.

The deviations between reference and branch model are variable with depth (Fig. 3.2). Since the Young's moduli of the lithologies defined in the model geometry are known, the following relationship can be established:

The multistage results consistently overestimate the stress magnitudes, with higher deviations for higher Young's modulus contrasts between the better resolved layers in the branch model and the coarse layer of the root model. Thus, if the Young's modulus is set too high, the resulting stress is also an overestimation of the actual stress magnitudes. Further information on submodelling using the FAST calibration tool is given in section 4.1.

3.1.3 On the influence of initial stress on final stress in geomechanical models

In this section a side aspect of numerical geomechanical models in general is addressed that touches both the large-scale and the small-scale model. It has been shown that a two-step approach is suitable for modelling the three-dimensional stress state at depth (e.g. Hergert and Heidbach, 2011). In the first step a reference stress state (McGarr, 1988; Zang and Stephansson, 2010) is established that accounts for the body force of gravity and ensures a realistic ratio of horizontal to vertical stress (Fig. 3.3 a). In the second step, this reference stress state is included in an undeformed model as an initial stress state and tectonic forces causing horizontal differential stress are introduced in addition to gravity. Omitting the first step would lead to very large compaction of an initially stress-free model due to gravity and would require very large horizontal compression since gravity under uniaxial strain conditions would result in a vertical stress far exceeding the horizontal stresses (Hergert and Heidbach, 2011). The initial stress avoids large deformation in the model and the original (observed) geometry of interfaces, structures etc. is maintained.

There is no general rule on how exactly the initial stress state is to be defined. If calibration data exist, the combination of initial stress and subsequent application of tectonic forces via displacement boundary conditions should yield the stress state at the location of the data. In the context of submodelling this implies that an initial stress state needs to be defined separately for both, the large-scale model, and the small-scale model. In this section it is investigated whether and how the choice of initial stress affects the final stress state in areas of the model domain where field data are lacking (Hergert et al., 2023).

A simple generic cubic-shaped numerical three-dimensional model is considered consisting of three horizontally layered units with increasing Young's modulus (E) with depth (Fig. 3.3 b). Poisson's ratio (ν) and density (ρ) are assumed as constant for all three units. The base of the cube is free to move horizontally but constrained vertically.

In this study different initial stresses are tested which are generated by applying different Poisson's ratios ($\nu=0.25, 0.35, 0.45$ and 0.495) in the first modelling step in which gravity acts under uniaxial-strain conditions (Fig. 3.3 a). Note, that these values are different from the actual Poisson's ratio ($\nu=0.25$) assumed for the rock that is applied in the second step. The higher Poisson's ratios in the first step are applied only to generate higher ratios of horizontal to vertical stress in the initial stress by exploiting the Poisson effect.

Horizontally directed displacement boundary conditions are applied at the vertical boundaries to account for tectonic stress (Fig. 3.3 b and second step in Fig. 3.3 a). Gravity acts as a body force. The finite element software package Simulia AbaqusTM is used.

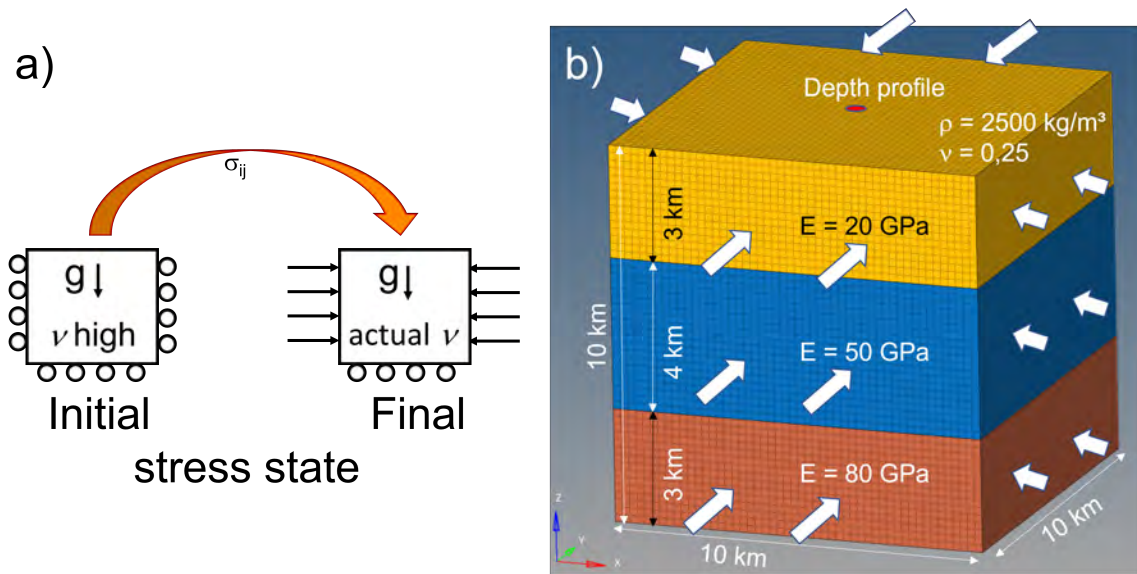


Figure 3.3: a) Sketch showing a two-step approach to model absolute stresses. In a first step an initial stress state is established which is then included in an undeformed model that is subject to tectonic forces. b) Geometry, dimensions, rock properties (E , ν , ρ), boundary conditions and depth profile at the centre of the generic numerical model.

In a first test an arbitrary calibration data set is assumed at 5 km depth at the centre of the model (minimum horizontal stress $S_{Hmin} = 90$ MPa, maximum horizontal stress $S_{Hmax} = 140$ MPa and vertical stress $S_v = 123$ MPa, which corresponds to the weight of the overburden at the assumed density of 2.5 g/m^3). Fig. 3.4 shows the final stress paths matching the data for the four different initial stress states. The initial stress states for the four cases are given by the blue line in Figs. 3.4 a–d and by the Poisson's ratios in the lower left used to generate these initial stresses. Different displacement boundary conditions given in the upper part of Figs. 3.4 a–d are necessary to match the data.

Although in all four cases the calibration data are matched, stress paths for S_{hmin} and S_{Hmax} differ from each other above and below the depth at which the data were determined. The larger initial horizontal stress (or ν used to generate initial stress), the higher the depth gradient of horizontal stresses, the smaller horizontal differential stress and the smaller the steps in stress paths at the interfaces between the units (Figs. 3.4 a–d). In the two cases with higher initial stress ($\nu = 0.45$ and 0.495) tectonic regime is strike-slip over the whole depth range whereas in the two cases with lower initial stress ($\nu = 0.25$ and 0.35) sections with normal faulting tectonic regime appear above the interfaces and reverse faulting near the surface. The latter two cases also show relatively high magnitudes of horizontal stress at the surface whereas the former two show negative S_{hmin} magnitudes at the surface. The surface magnitudes may not necessarily be a criterion to evaluate which case is the most realistic one since in reality rock is often unconsolidated, highly fractured and weathered near the surface and plastic material behaviour does play a role. Fig. 3.4 e shows the final stress paths of all four cases together which reveals that the deviations between the different cases are largest at the interfaces of the units and in each of the units there is one depth at which all of the cases yield the same result. The differential stresses at these depths ($S_d = 20, 50$ and 80 MPa) correspond to the Young's moduli of these units ($E = 20, 50$ and 80 GPa).

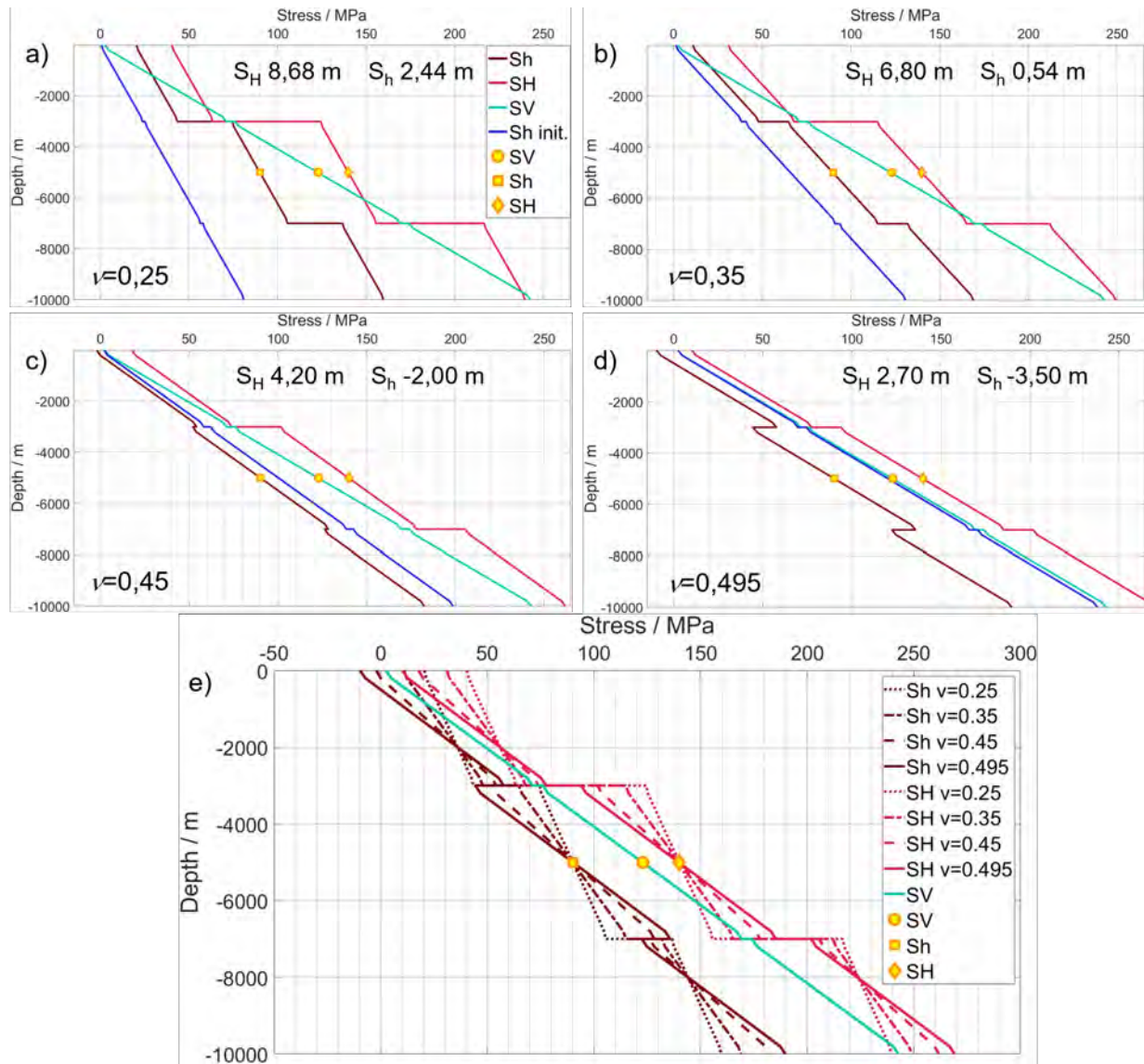


Figure 3.4: Depth profiles of final stress matching the calibration data at 5 km depth for four different initial stress states given by the Poisson's ratios in the lower left of a)-d) applied in the first step of Fig. 3.3 a) and displayed by the blue line in a) to d). Displacement boundary conditions necessary to match the calibration data are given in the upper part of a) to d). e) shows the paths of final stress for the individual cases altogether.

Sets of calibration data at other depths and in other units have been tested as well (Fig. 3.5). If stress data at 1 or 4 km depth are matched there is no longer one distinct depth in the lower unit at which final stress is independent on the choice of initial stress (Fig. 3.5 a and b). For data at 1 km depth this also applies for the middle unit. In addition, deviations in final stress for the different initial stresses become increasingly larger with depth. Contrarily, if deep calibration data at 8 km depth are matched the variability in final stress due to the choice of initial stress is smaller (Fig. 3.5 c).

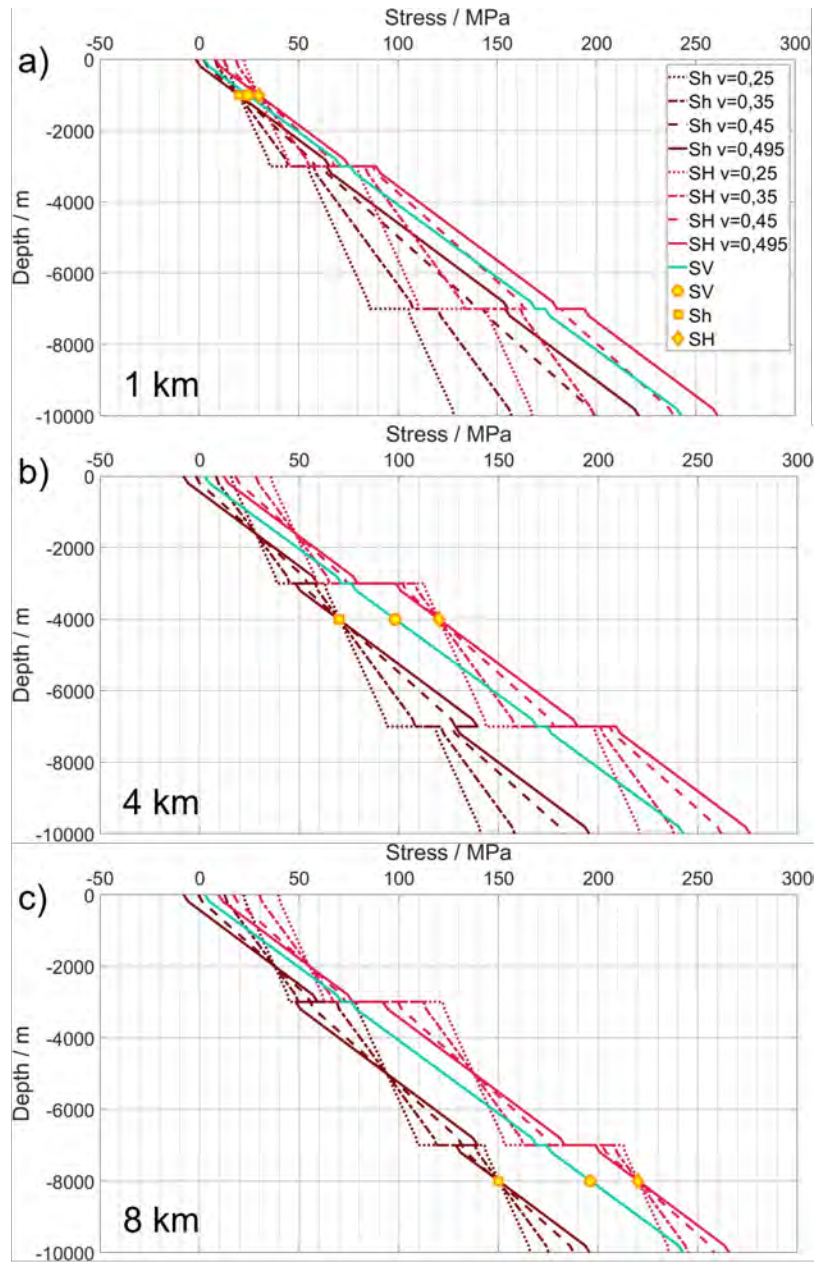


Figure 3.5: Depth of calibration data. a) 1 km, b) 4 km, c) 8 km.

Another case has been considered in which displacement boundary conditions are not uniformly distributed over depth but linearly increase with depth (Fig. 3.6). Independently on the applied initial stress final stress is the same over the whole depth section of the middle unit containing the calibration data (Fig. 3.6 a). However, final stress differs among the considered initial stresses in the upper and lower units. Vertical stress and horizontal stress paths in the lower unit increase no longer linearly with depth which may be caused by bending of the model domain due to the non-uniform boundary conditions as indicated by the vertical displacement in Fig. 3.6 b.

Further tests have been performed addressing the Young's modulus, Poisson's ratio and density of

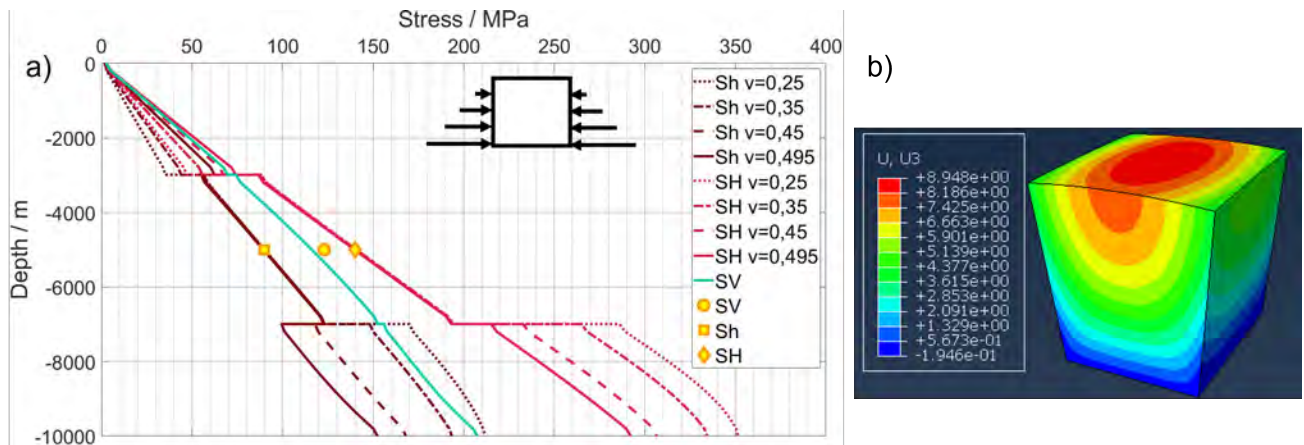


Figure 3.6: Depth-dependent boundary conditions for four different initial stresses. a) Final stress profiles. b) Vertical displacements resulting from the applied boundary conditions.

the three units, also dipping interfaces between the units and a tectonic fault have been considered. A change in Young's modulus in the upper and lower units hardly affects the stress state in the middle unit containing the calibration data. An increase of Young's modulus in the upper or lower unit lowers the distinct depth at which there is no influence of initial stress on final stress. Reducing the Young's modulus in these units lifts that depth.

Tests with two or three sets of calibration data in different units have been analysed as well. Matching several sets of calibration data at the same time puts stronger requirements on model parameters, e.g., using unit-dependent initial stress (different ν for individual units in the first step in Fig. 3.3 a), unit-dependent displacement boundary conditions or non-elastic material behaviour. This raises the question to what extent data should or need to be matched since the calibration data as well as the rock properties do have uncertainties.

3.1.4 Conclusions

- The final stress state in data-calibrated models depends on the choice of initial stress for areas in which no data exist => Location-dependent prediction quality of stress
- Largest deviations in final stress due to choice of initial stress expected at interfaces between units
- Stress data from greater depth are more valuable for calibration purposes than shallow ones
- Simultaneous fitting of several data sets evokes the consideration of uncertainties in stress data and rock properties

3.2 Development of modelling techniques to adapt mechanical properties to the model scale

3.2.1 Rock mechanical parameters

Geomechanical modelling usually utilises static rock mechanical parameters from laboratory measurements (e.g., Young's modulus and Poisson's ratio from uniaxial and triaxial tests to describe the elastic material behaviour) for the numerical simulations. The specimens used for the test have a size of a few centimetres to a few decimetres. However, already at these dimensions, a scale dependence can be observed, for example, a decrease of the Young's modulus with increasing specimen size (e.g. Jamshidi, 2014). In contrast, the computational cells of geomechanical models typically have edge lengths ranging from tens of meters to a few kilometres (depending on whether it is a local, regional or Germany-wide model). At this scale, due to vertical and lateral changes in material parameters, as well as inhomogeneities such as fractures, it cannot be assumed that the mechanical parameters from the laboratory are representative for a computational cell. Thus, modelling techniques have to be developed to adapt material properties to model scale and size of the finite elements, respectively.

This problem is well known in engineering geology and geotechnics, which differentiate between rock and rock mass ("Gesteins(Fels-)mechanik" and "Gebirgsmechanik"): In addition to the intact rock, inhomogeneities like fractures and bedding planes must also be considered in terms of their spatial position and mechanical properties, since they have a decisive influence on the mechanical behaviour and strength of a larger rock volume. So far, the use of upscaling techniques depending on the model scale is no common practice, presumably because for a given (and fixed) model size calibration of the models to in situ stress measurements is accomplished by adjusting displacement boundary conditions. However, if different model scales are combined in the submodelling manner envisaged in the present SpannEnD 2.0 project consideration of scale-dependent mechanical material properties is required. Up to now, three different methods have been investigated and compared for the determination of (rock mass) mechanical parameters adapted to the element size: Empirical correlations based on engineering geological rock mass classifications, Discrete Fracture Network (DFN) models and Synthetic Rock Mass (SRM) models. The aim of the work package is the development of tools that allow a flexible, i.e. suitable for arbitrarily large calculation cells, upscaling from rock to rock mass properties including the fracture network.

3.2.2 Estimates based on rock mass classification schemes

Empirical relationships based on rock mass classification schemes are established methods in engineering geology to estimate rock mass compressive strength and rock mass Young's modulus (deformation modulus), respectively. Widely used are classification schemes like the Rock Mass Rating (RMS; Bieniawski, 1973, 1989), the Geological Strength Index (GSI; Hoek, 1994) and the Tunnel Quality Index (Q, Barton et al., 1974). Strictly speaking, the classifications are not based on a concrete scale dependency, but the person in charge must decide on the basis of the local conditions and the task, how large the representative observation area has to be. Typically, the scale for which these rock mass classifications are used is in the range of a few tens of meters, i.e., similar to the computational cell size of local to regional geomechanical models.

The RMR system has six input variables, i.e., the unconfined compressive strength (UCS) of the intact rock, the Rock Quality Designation (RQD) parameter, the spacing and condition of the fracture, water inflow and the orientation of the geotechnical structure relative to the main fractures. Each parameter is scored using a point system, and the individual scores are summed to produce an RMR value that describes the quality of the rock mass between 0 (very poor) and 100 (very good). Rock mass classification by GSI uses the degree of fracturing and the condition of the fracture surfaces (roughness, alteration). The GSI value also varies between 0 and 100 and can be determined either using appropriate tables (Hoek et al., 2013) or computationally using a parameter from the RMR system and the RQD value. In addition to the RQD parameter, the Q-system uses data on the number of fracture sets, fracture roughness and alteration, and pore pressure and in situ stress state. Specific values are assigned to the individual variables using detailed tables, which are then incorporated into a calculation formula for the Q value. This value can range on a logarithmic scale from 0.001 (exceptionally poor) to 1000 (exceptionally good) for the rock quality.

For these three, more detailed rock mass classifications – or just for the RQD parameter – different empirical correlations are available to link the ratings with rock mass parameters (deformation modulus, rock mass compressive strength). A compilation of such empirical correlations which are derived from numerous tunnelling, open pit mining and rock slope projects can be found e.g. in Hoek and Diederichs (2006). All those empirical correlations that use the Young's modulus from laboratory measurements in addition to the value from the rock classification schemes show a significant reduction of the rock mass (deformation) modulus compared to the laboratory value for the intact rock. Application to sandstone and granite outcrops by Gottron (2022) shows that the deformation modulus of the rock mass is only about 40% of the Young's modulus of the rock (Fig. 3.7). However, although application of this upscaling technique is rather straightforward, the use of engineering geological classification schemes and related empirical correlations lacks a concrete scale reference and physical basis. In addition, it is also not possible to describe anisotropic material properties, e.g., due to layering and/or different degrees of fracturing.

3.2.3 Estimates from Discrete Fracture Network (DFN) models

DFN models (Fig. 3.8) use a combination of deterministic and stochastic description of inhomogeneities to characterise the rock mass. Large fractures and faults, as well as bedding planes, are implemented at their actual position in the model, while a statistically equivalent representation is used for the large number of small to medium sized fractures. The input variables required for this stochastic input are the orientation (dip direction and dip angle), size and intensity of the various fracture sets with corresponding probability density functions to represent the variability. This information can be determined in outcrops using manual measurements (compass and tape measure), laser scanning and/or photogrammetry, or in boreholes using oriented cores and imaging logs. In the stochastic part of the DFN model, a single fracture has no exact equivalent in reality, but the overall properties of the fracture network in a larger volume are the same. In addition to this geometric description of the fracture network, specific mechanical – and also hydraulic if desired – parameters are assigned to the rock matrix and the fractures. Corresponding values can be determined in standard laboratory tests, i.e. uniaxial, triaxial and direct shear tests.

This parameterised DFN model can then be used to calculate the hydraulic and mechanical properties of arbitrarily large element volumes. In practice, the same element grid which is subsequently

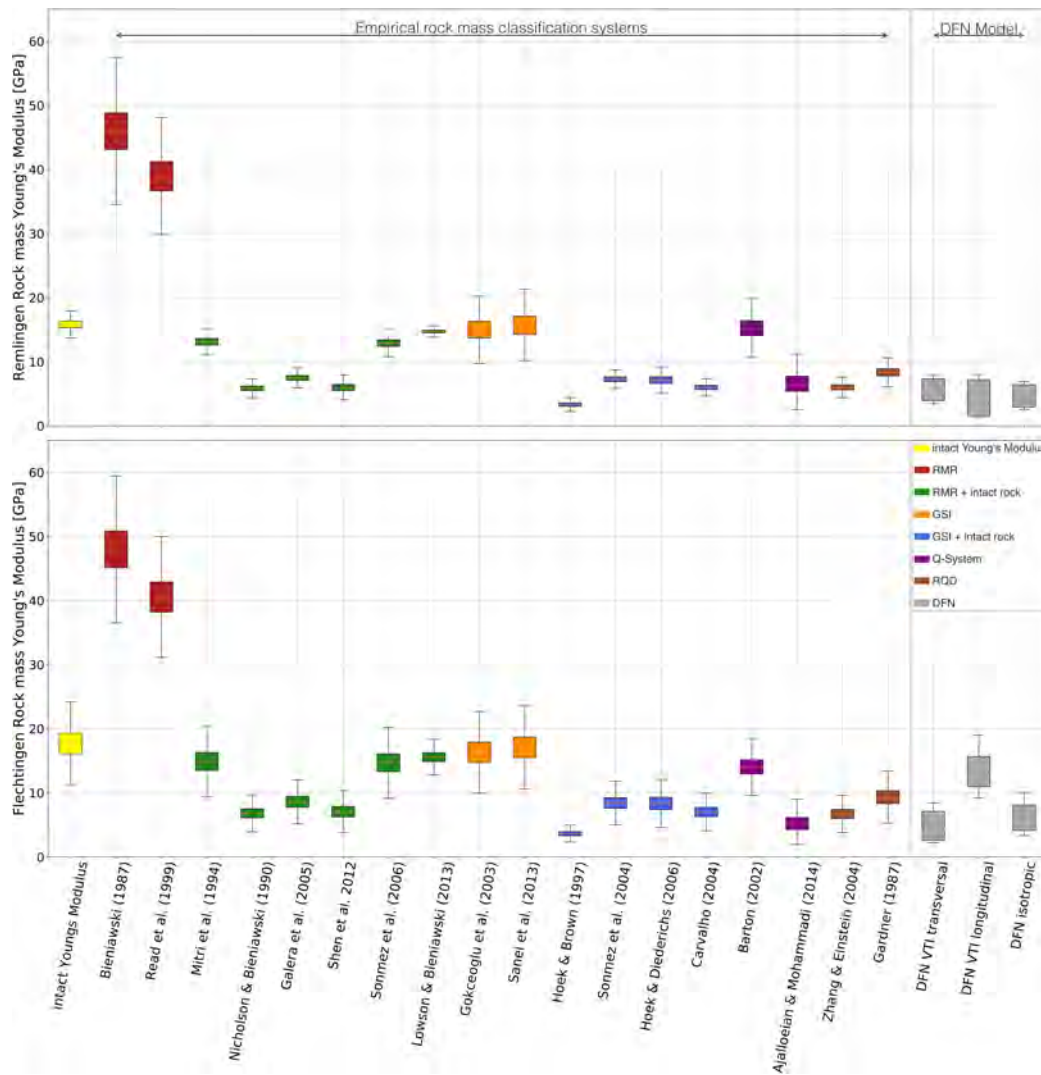


Figure 3.7: Comparison between Young's modulus of intact rock from laboratory measurements, rock mass (deformation) moduli determined with empirical correlations based on different rock mass classification schemes (Bieniawski, 1978; Read et al., 1999; Mitri et al., 1994; Nicholson and Bieniawski, 1990; Galera et al., 2007; Shen et al., 2012; Sonmez et al., 2006; Lawson and Bieniawski, 2013; Sanei et al., 2013; Hoek and Brown, 1997; Sonmez et al., 2004; Hoek and Diederichs, 2006; Carvalho, 2004; Barton, 2002; Ajalloeian and Mohammadi, 2014; Zhang and Einstein, 2004; Gardner, 1987) and rock mass (deformation) moduli determined from discrete fracture network (DFN) modelling using the Oda Geomechanics method (Gotttron and Henk, 2021). Shown are two case studies from sandstone outcrops of different stratigraphic ages (Buntsandstein above, Rotliegend below). The value for the Young's modulus of the intact rock is shown in yellow. The range of values shown for the empirical correlations results from the use of a Monte Carlo approach to account for uncertainties in the input parameters for the rock mass classification schemes.

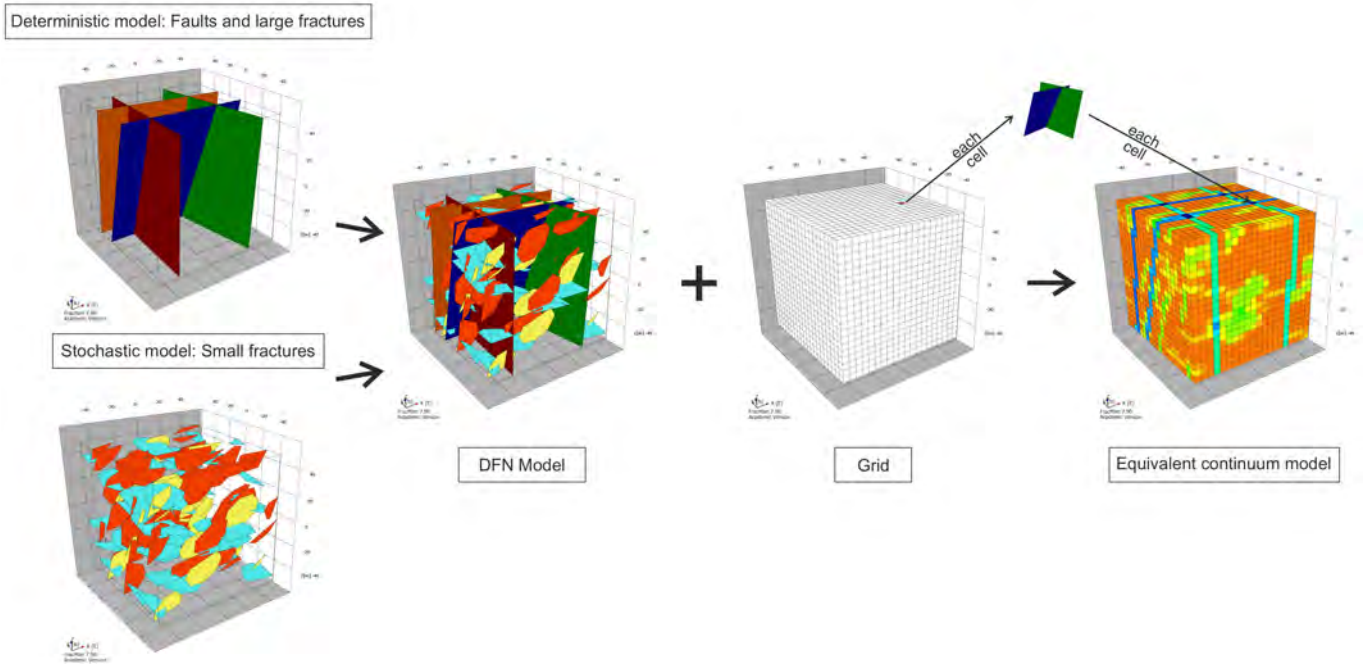


Figure 3.8: Schematic representation a DFN modelling work flow (Gotttron and Henk, 2021). Faults and large fractures are defined as deterministic structures, while the numerous small to medium fractures are included using a stochastic approach, i.e., a statistically equivalent description. The two approaches are combined into a deterministic-stochastic representation of the fracture network geometry. Hydraulic and mechanical properties are then assigned to the individual fracture sets and the rock matrix. Upscaling of material properties uses the Oda Permeability Method (Oda, 1985) for hydraulic calculations and the Oda Geomechanics Method (Oda, 1986) for mechanical calculations. Therefore, the same computational grid that is subsequently used for the numerical simulations is used. The approach provides tensors for Young's modulus, Poisson's ratio, and permeability for each cell. Thus, specific values can be determined which depend on the element size of the geomechanical (and hydraulic) model. This approach also allows for simulations with anisotropic and spatially varying material properties.

used for the numerical simulations, i.e. the geomechanical modelling, should be utilised. For the upscaling of mechanical parameters to this computational grid, the so-called Oda Geomechanics (Oda, 1986) method is used, which takes into account the specific spatial position of the fractures in each cell as well as the stiffness of the rock and the normal and shear stiffnesses of the fracture sets. The approach provides either isotropic values or anisotropic tensors for the rock mass Young's modulus (deformation modulus) and the rock mass Poisson ratio (Fig. 3.9). While this type of upscaling is routine for flow modelling to derive permeability tensors (Oda, 1985, e.g., modelling fracture aquifers), its application to mechanical parameters for large-scale geomechanical modelling is not yet established. However, the approach offers the possibility to calculate spatially variable and anisotropic rock mass properties which can be used to populate geomechanic numerical models. At the same time, the method offers flexibility, because based on the same DFN model, specific elastic

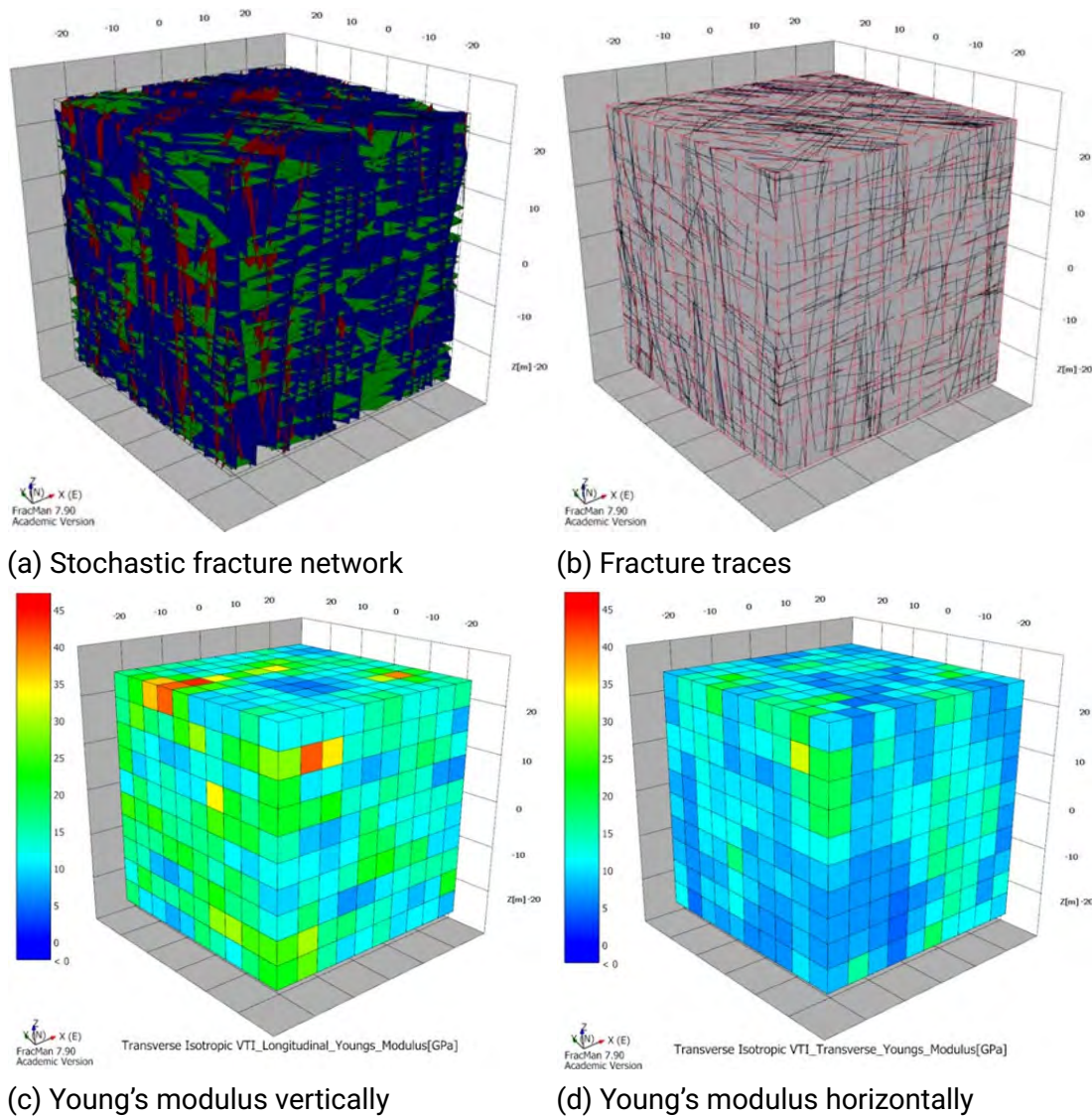


Figure 3.9: DFN modelling of a granite outcrop (Gottron, 2022). a) shows the stochastic fracture network with three nearly orthogonal fracture sets for a $50 \times 50 \times 50 \text{ m}^3$ rock volume. In b), the fracture traces on the outer sides of the model are shown, as well as the computational mesh with $10 \times 10 \times 10$ elements (in red) used for upscaling. The anisotropic Young's modulus values calculated for each cell in vertical and horizontal directions are shown in c) and d), respectively. On the basis of the DFN model, any calculation grid sizes are possible for upscaling, in extreme cases consisting of only one element.

parameters can be determined scale-dependently, i.e. for different sized calculation cells of a finite element model.

In order to check the plausibility of the geomechanical parameters calculated from the DFN workflow described above, in particular the rock mass Young's modulus, Gottron (2022) compared the results with estimates of the empirical correlations based on the rock mass classification schemes (Fig. 3.7). A very good agreement is shown for the investigated case studies, whereby the additional

effort in the creation of the DFN models compared to the use of engineering geological rock mass classifications or the corresponding empirical correlations allows for a real scale dependence and also provides anisotropic as well as laterally and vertically varying rock mass properties. Preliminary work with DFN models larger than the $50 \times 50 \times 50 \text{ m}^3$ presently used, i.e. for cell sizes typical for the stress model of Germany, indicate that the rock mass Young's modulus does not continue to decline continuously with increasing element size but reaches some kind of saturation value.

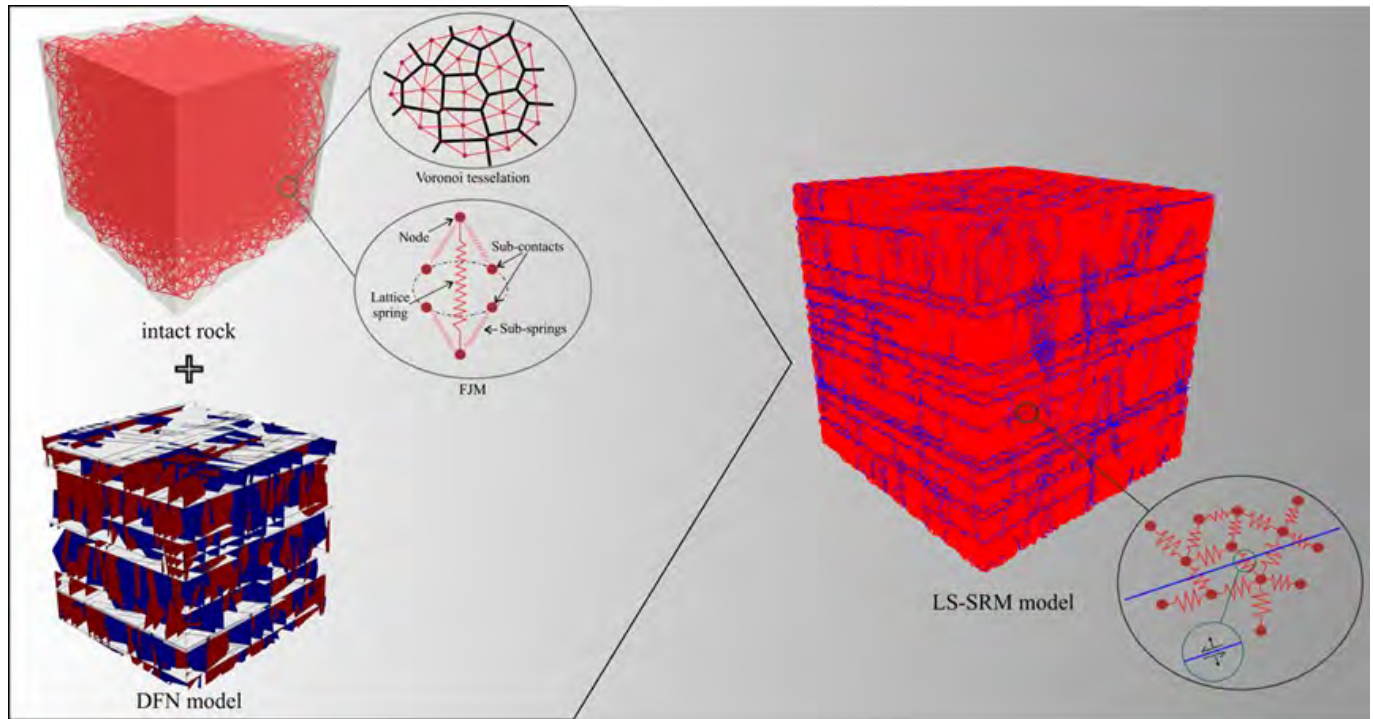


Figure 3.10: Schematic representation of a lattice-spring synthetic rock mass (LS-SRM) model (Gotton and Henk, 2022). The intact rock volume is intersected with the fracture network geometry of the DFN model, allowing for shearing/opening of the fractures as well as crack propagation, i.e. formation of new fractures. The LS-SRM model can be used to simulate arbitrary loading cycles, from which mechanical rock mass properties can be derived.

3.2.4 Estimates based on Synthetic Rock Mass (SRM) models

The SRM approach to describing fractured rock was introduced by Pierce et al. (2007). In general, SRM models consist of two components, the intact rock and the preexisting discontinuities, whereby various numerical techniques such as the Discrete Element Method (DEM) can be used to describe the mechanical behaviour of the entire system. In the present study, the lattice-spring synthetic rock mass (LS-SRM) approach is used (Cundall, 2011, Fig. 3.10). In this approach, the intact rock is described by a random array of point masses, each connected by springs to represent the normal and shear stiffnesses. When the applied forces exceed the strength of the springs, a microcrack is formed, which may coalesce with other cracks and lead to the formation of macroscopic fracture

surfaces. This also allows numerical experiments to analyse the fracture behaviour of intact rocks under loading conditions. However, the corresponding micromechanical model parameters for the springs must first be determined by reproducing laboratory experiments (e.g. uniaxial tests) with numerical models. A direct input of the Young's modulus or the Poisson's ratio is not possible. The pre-existing discontinuities are included in the LS-SRM model by intersection with a DFN model. Existing fractures are defined as contacts that break if the initial shear strength is exceeded and sliding under the residual friction angle occurs or that open if the tensile strength is exceeded. Thus, the modelling approach can describe both the reactivation of existing discontinuities and the formation of new fractures.

The use of LS-SRM models for upscaling purposes of mechanical material parameters requires several working steps. First, laboratory tests on intact rock must be reproduced to determine the micromechanical spring stiffnesses, which then needs to be transferred to the desired model scale. Subsequently, the intersection with the DFN model is performed to define the contacts. This combined rock mass model can then be used for numerical experiments, i.e., a hypothetical uniaxial test on a large rock volume. From the calculated stress-strain curve, the rock mass Young's modulus and the rock mass Poisson's ratio can be determined. SRM approach yields similar rock mass properties like the DFN approach applied to one element. However, spatial variations cannot be captured and the adaptation to different model scales is not very flexible, since the micromechanical parameters have to be recalibrated depending on the scale. The strengths of the LS-SRM approach lie primarily in the possibility of including fracture processes in the analysis. However, since the stresses in large-scale models are predominantly in the elastic range, this methodology offers potential especially for small-scale geomechanical simulations, e.g. in connection with the excavation of a repository.

3.2.5 Preliminary conclusions and next steps

Empirical correlations based on engineering geological rock mass classification schemes are comparatively easy to apply and can account for the impact of fractures on a general reduction of the rock mass deformation modulus and the rock mass compressive strength. However, this methodological approach is not based on a physical understanding and a true scale dependence, respectively. Furthermore, no anisotropy in the mechanical properties can be derived and the empirical correlations are lithology-dependent providing a considerable range of estimates due to uncertainties in the values used for the rock mass classifications.

In contrast, the DFN approach is much more complex and requires a deterministic-stochastic representation of the geometry of the fracture network. This information and the corresponding probability density functions can be determined on the basis of outcrop and borehole data. In addition, laboratory tests such as uniaxial, triaxial and direct shear tests are required to determine mechanical parameters for both the rock and the fractures.

While the DFN model itself has to be created only once, it can be applied to arbitrary element sizes of the computational mesh. The Oda Geomechanics approach applied to the DFN model provides scale-dependent values for rock mass Young's modulus (deformation modulus) and rock mass Poisson ratio. These values can be spatially varying, isotropic or anisotropic material properties that can be used for the parameterisation of geomechanical models. Based on the same geometric DFN model, hydraulic parameters (permeability tensor) can also be determined if the poro-perm properties of the rock and the aperture of the fracture are defined additionally. Thus, hydromechanically coupled

modelling based on the same fracture network geometry is possible without much additional effort.

SRM models are the most time-consuming to build because, in addition to the geometry of the fracture network from a DFN model, further steps are required to calibrate the intact rock properties and to evaluate the numerical experiments of a hypothetical rock mass. The strengths of this approach lie in the inclusion of fracture processes due to both damage of the intact rock and reactivation of existing discontinuities. Thus, this methodology seems to be better suited for detailed geotechnical applications related to the construction of the repository rather than large-scale geomechanical models.

As a preliminary result of this work package, different methods and tools are available for the parameterisation of geomechanical models depending on model scale and element size, respectively. Especially the DFN approach offers a great potential, so that the next step is the application to generic models of different size. This also includes a detailed analysis of how boundary conditions have to be selected depending on lithology-dependent rock mechanical properties and the degree of fracturing. The ultimate goal is the consistent integration of scale-dependent material properties into the submodelling technique. This is necessary not only to ensure that displacement and stress results of larger models can be transferred as boundary conditions to smaller models. It is also required to account for the differentiation of the mechanical properties to be considered with the increasing spatial resolution, i.e. on the way from the stress model of Germany to local geomechanical models of potential repository sites.

3.3 Preparation of the geomechanical model sub-area 001

3.3.1 Extent of sub-area 001 and available data for modelling

For the development of investigation methods, areas for method development have been defined by the BGE. This is not a predetermination of particularly promising investigation areas or preferred siting regions. Sub-area 001 is the area for the host rock claystone. It extends over the two federal states of Baden-Württemberg and Bavaria (Fig. 3.11). The area with a size of 4241 km² refers to the formation Opalinus Clay, the stratigraphic unit Jurassic with a thick mudstone unit of maximum thickness of 300 m.

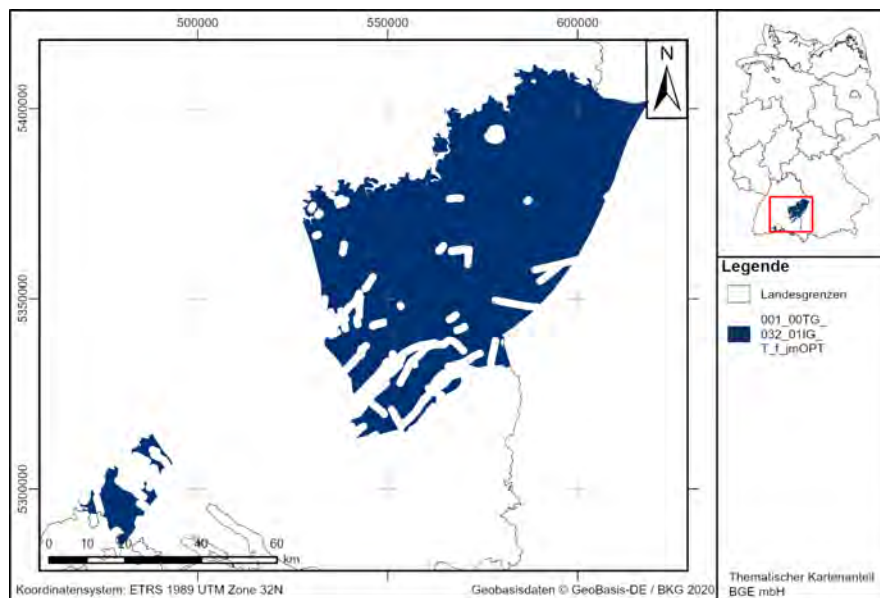


Figure 3.11: Extent and definition of the sighting region 001 (Gebiet zur Methodenentwicklung: Opalinuston BGE, 2021a) .

A geomechanical model is to be created for the region, which will receive the stress state from the Germany model via the sub-modelling technology. The focus of the model is mainly on a detailed resolution of the Opalinus Clay and the overlying and underlying units. Three freely available structural geological models are currently available for the region. These are the state model of Baden-Württemberg (Rupf and Nitsch, 2008) and the models of the Geo-Mol project. The Frame model Bavaria (2015) and the GeoMol pilot area Lake Constance - Allgäu (Bavaria; GeoMol LCA-Projectteam, 2015a) are available from this project. Furthermore, models for northern Switzerland were created by NAGRA, which exist for the siting regions Jura Ost (JO), Nördlich Lägern (NL) and Zürich Nordost (ZNO). Fig. 3.12 shows a summary of the models in the context of sub-area 001.

Geomechanical models are preferably geometrically aligned parallel or perpendicular to significant geological structures (layer inclusions, material contrasts, faults, but also topography) and usually even more essential the orientation of the stress field. Fig. 3.13 shows a compilation of various data on the map, based on the analysis of existing data of the World Stress Map (WSM, Heidbach et al., 2018). This analysis of the stress orientations in the region shows that the model is optimally aligned



Figure 3.12: Map of south-western Germany with sub-area 001 (purple), the extent of the models of Badem Württemberg, (Landesmodell Baden-Württemberg, black; Rupf and Nitsch, 2008)), GeoMol Framework model Bavaria (blue; GeoMol Team, 2015), GeoMol pilot area Lake Constance – Allgäu, Bavaria (red; GeoMol LCA-Projectteam, 2015b) and the model regions Jura Ost (JO), Nördlich Lägern (NL) and Zürich Nordost (ZNO) in northern Switzerland. (Background map: World Topographic Map, arcgis.com)

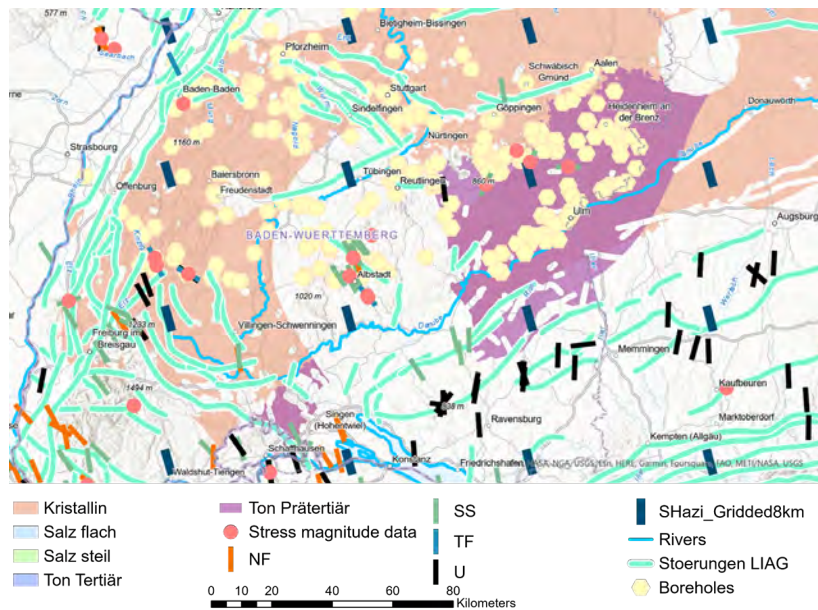


Figure 3.13: Map of south-western Germany showing the main geological units, rivers, faults and orientation of S_{Hmax} (Heidbach et al., 2018) and sub-area 001. (Background map: World Topographic Map, arcgis.com)

when model boundaries edges are exactly W-E or N-S aligned.

3.3.2 Subsidence Analysis of the sub-area 001

3.3.2.1 Method

Stress prediction is performed incorporating changes in material properties during basin subsidence and uplift and changes in regional stress fields over geological time. Concerning the analogy with full physics numerical basin modelling, PetroMod™ Software of Schlumberger was selected to test stress prediction.

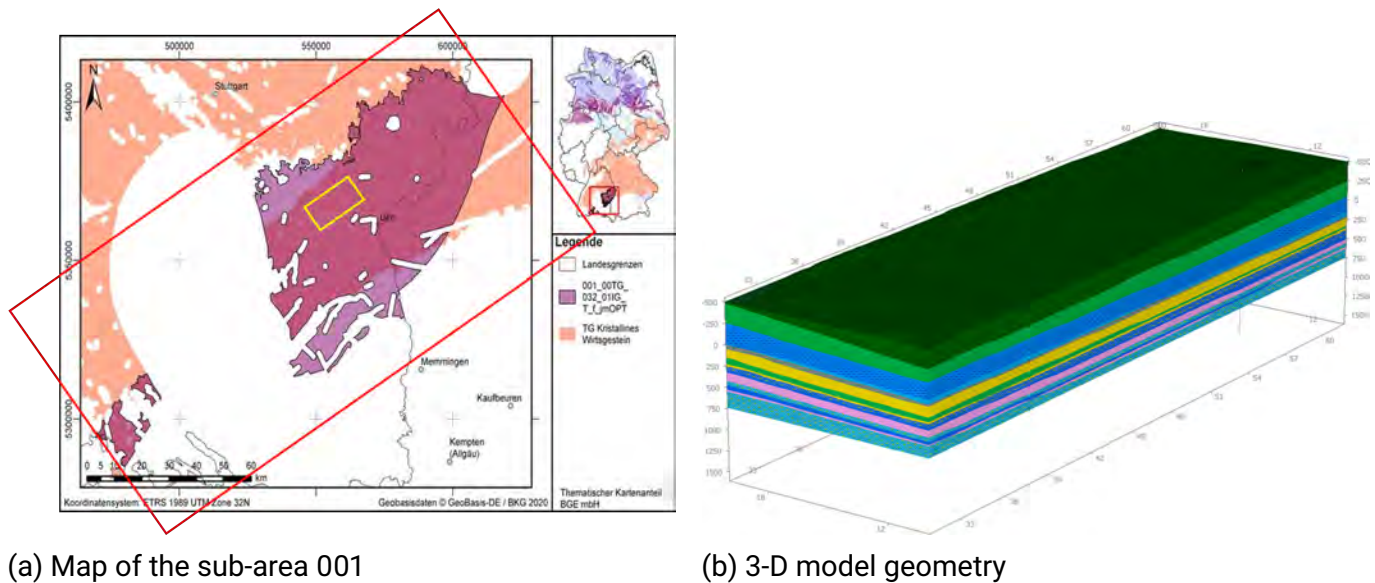


Figure 3.14: Model region of sub-area 001 (BGE, 2021c) with the location of the subsidence model in yellow. The 3-D model used for the immersion analysis consists of 17 stratigraphic units.

3.3.2.2 Input data

Different conceptual 1-D and 3-D models were constructed using Schlumberger PetroMod™ 2023 (Fig. 3.14). The input data includes present-day geological models, paleo-geometries, and thermal boundary conditions calibrated against measured parameters in the study area, e.g., vitrinite reflectance and corrected bottom hole temperature. The study area is located between the federal states of Baden-Württemberg and Bavaria, covering approximately 120 km². Thereby, the nested models (Fig. 3.14) maximum extent is around 15 km from southwest to northeast and 8 km from northwest to southeast. The 3-D model comprises 17 stratigraphic units from the crystalline basement to the Quaternary.

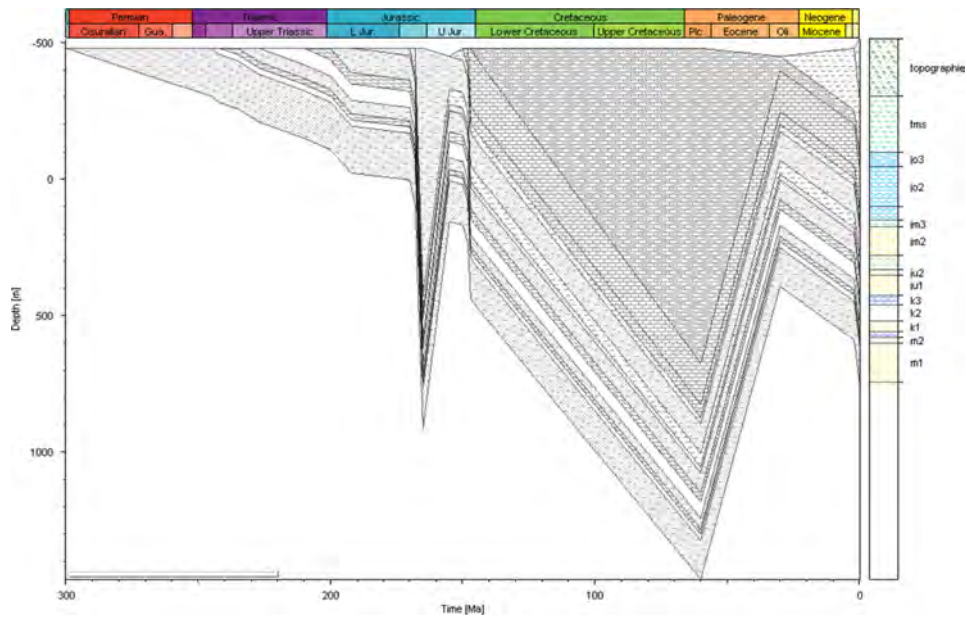
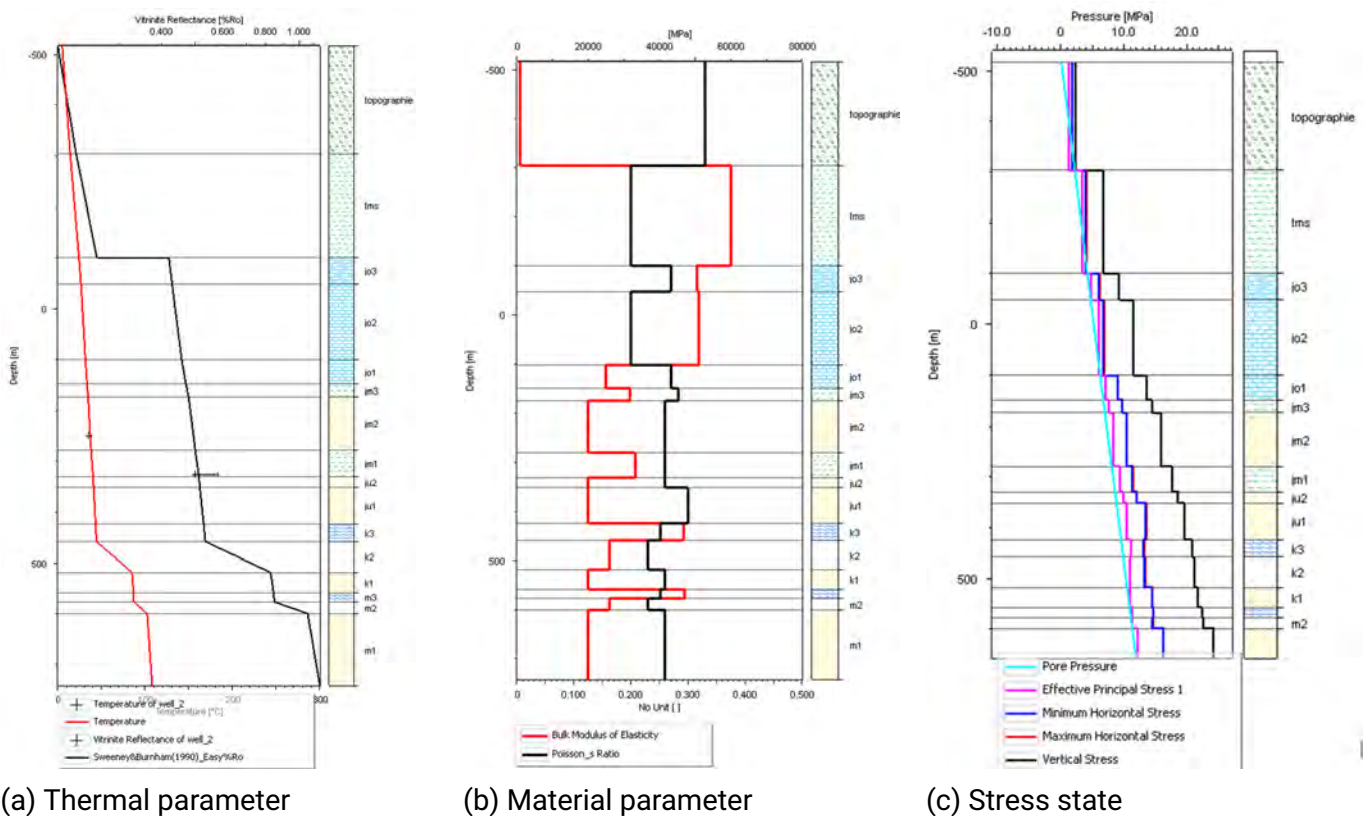


Figure 3.15: Reconstruction of the basin immersion from Permian to Quaternary within the 3-D model in the centre of sub-area 001 showing multiple phases of depth immersion.



(a) Thermal parameter

(b) Material parameter

(c) Stress state

Figure 3.16: Plot of definitions and results along a virtual well.

Table 3.1: Boundary conditions for thermal model based on the paleo-water depth, the sediment water interface temperature (SWIFT) and the heat flow.

Time Ma	Depth m	Temperature °C	Heat flow mW/m ²
0	-500	5.00	70
2	-480	6.40	70
30	-480	17.10	65
60	-480	18.76	65
145	-480	20.36	65
147	-480	20.20	65
148	-480	20.20	65
150	-480	20.20	65
155	-480	20.14	65
165	-480	18.73	65
168	-480	18.32	65
170	-480	18.13	65
192	-480	16.86	65
200	-480	17.63	65
210	-480	19.23	65
227	-480	21.52	65
235	-480	22.73	65
242	-480	22.80	65
245	-480	22.47	65
247	-480	22.18	65
300	-480	20.20	65

3.3.2.3 Boundary conditions

The basal palaeo-heat flow as the lower thermal boundary condition was set to 65 mW/m² (Tab. 3.1), close to the average heat flow in continental crust (Allen and Allen, 2013) and close to the average present-day heat flow in central Europe (Hurter and Haenel, 2002).

The Sediment Water Interface Temperature (SWIT) was calculated using the built-in PetroMod calculator including the palaeo-water depth and the palaeo-latitude (Wygrala, 1989). For this, a present-day latitude of 48° N was set, representing southern Germany (Tab. 3.1).

3.3.2.4 Calibration

The calibration data was implemented from the Benken well in Northern Switzerland, which has similar geological conditions. It shows good calibration in the 1-D models (Fig. 3.16). The resulting burial, erosion and temperature histories were used to build the 3D model.

3.3.2.5 Preliminary results

The mechanical parameters for each lithology are based on the PetroMod library. The Young's modulus and the Poisson ratio were implemented from the BGR report (Reinhold et al., 2013). The mechanical boundary conditions were not yet tested therefore there is a normal faulting regime

in the model ($S_v > S_{Hmax} > S_{hmin}$; Figs. 3.16). Preliminary results are from the Opalinus Clay jm1 unit at 800 m depth with a vertical stress of 19.10 MPa, maximum horizontal stress and minimum horizontal stress of 12.50 and 12.31 MPa, respectively. In the further work the stress prediction is needed to be compared and calibrated with measured stress data.

3.4 Preparation of the geomechanical model for sub-area 009

The model resolution of the geomechanical-numerical model for Germany (see AP 1) is usually not sufficient for assessment of the stress state in a siting region or even for a repository-scale assessment. Therefore, submodelling is used to transfer the stress state from the global Germany-model to a regional scale model of a siting area which has a regional-scale size. This regional-scale siting area model addresses crystalline host rock. As a contribution to method developments, the model is focused on a part of siting area 009 (Teilgebiet 009_00TG_194_00IG_K_g_SO, Fig. 3.17).

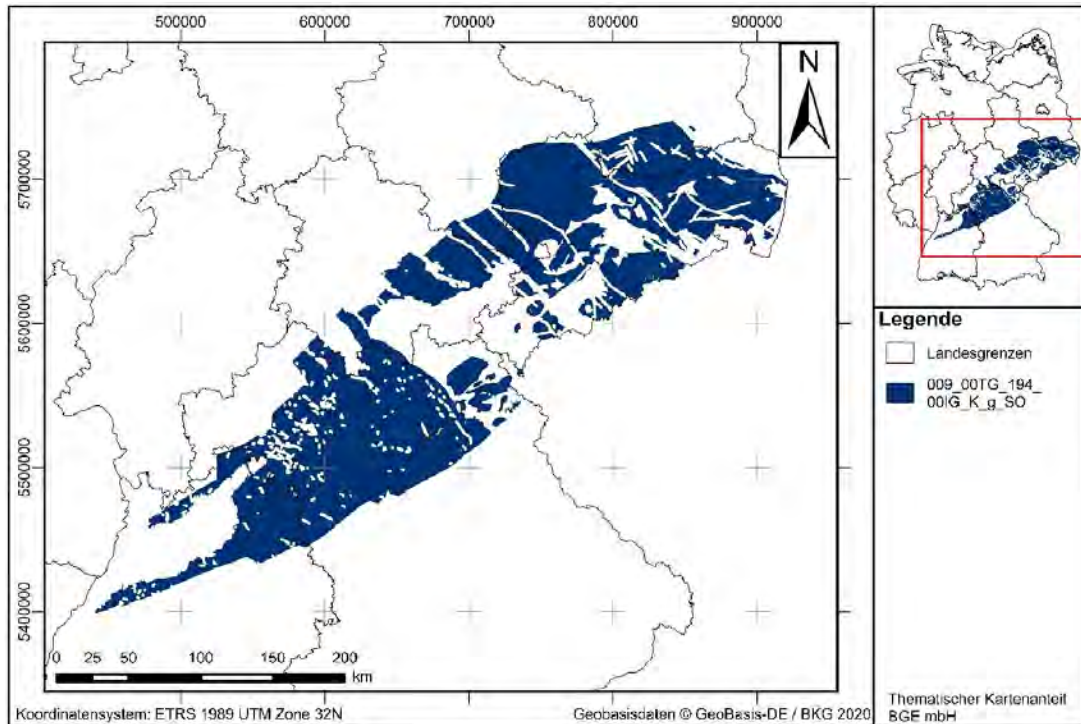


Figure 3.17: Extent and definition of the siting region 009 (Gebiet zur Methodenentwicklung: Saxothuringikum, BGE, 2021b).

Due to the vast area of siting area 009, the model area does not cover the entire region. Instead, only a fraction of the region is modelled. The model area is chosen in a way to contain the German Continental Deep Drilling Programme (German: Kontinentales Tiefbohrprogramm der Bundesrepublik Deutschland, KTB) site with a unique set of geoscientific data that is available. Furthermore, the model is extended towards the northeast in order to incorporate an existing geological model of the Ore Mountains (Erzgebirge). This results in a model with an area of $250 \times 110 \text{ km}^2$ (Fig. 3.18). The model extends vertically down below the Moho in order to be able to test potential influence of the Moho on the stress state.

The model geometry is based on the data collected in section 2.2 which in turn is based on different low- to high-resolution datasets, e.g. several 2-D seismic lines, a gravity model, local 3-D seismic surveys. Furthermore, major tectonic elements, such as the Eger Graben, the Mariánské Lázně fault and the Frankonian line are included in the model geometry. The faults are not implemented as active contact surfaces. Instead, they are used in order to allow a refined offset of lithologies and

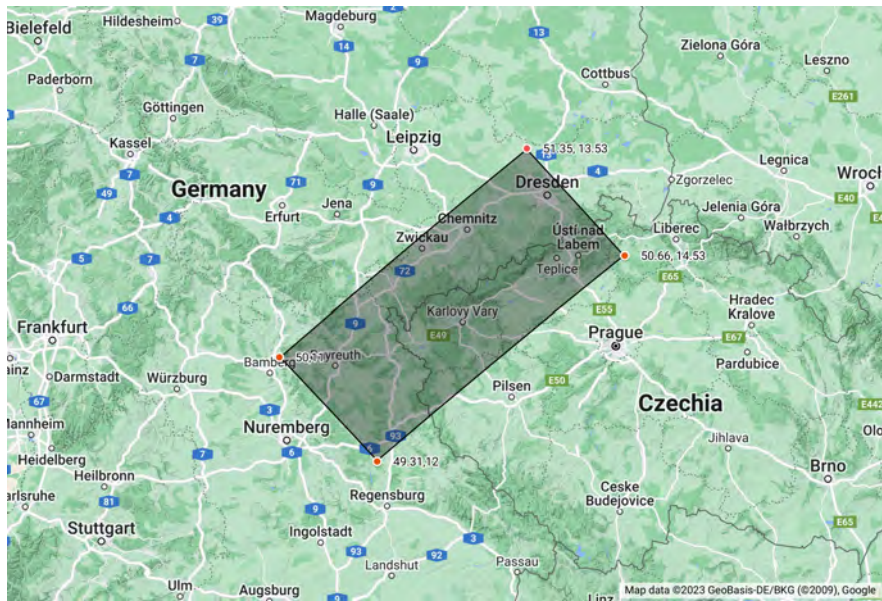


Figure 3.18: Extent of the regional scale geomechanical model of the siting area 009. The coordinates of the corners of the model are displayed. (Map: www.google.de/maps)

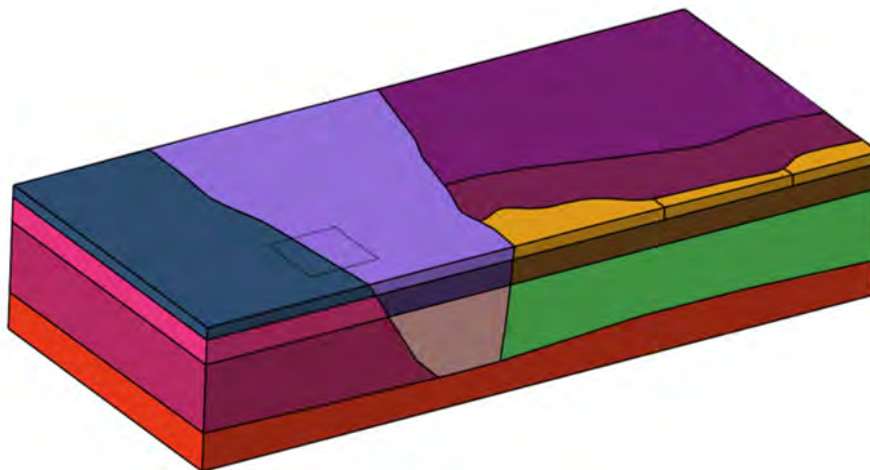


Figure 3.19: Model geometry before discretisation. The segmentation into different lateral and vertical volumes is colour coded. Clearly visible is the area of the German Continental Deep Drilling Programme as a square close to the lower left corner of the model (For a detailed view of the discretised area of the German Continental Deep Drilling Programme, see Fig. 3.20).

in order to segment the model into several laterally different regions (Figure 3.19). This allows to assign different rock properties based on laterally different areas.

In order to estimate the stress state, the model is discretized with approx. 3 Mio. elements of hexahedral (brick) and heptahedral (degenerated hexahedral/brick with a triangular base area) shape. The elements have a lateral resolution between 500 m and 2000 m. The highest lateral

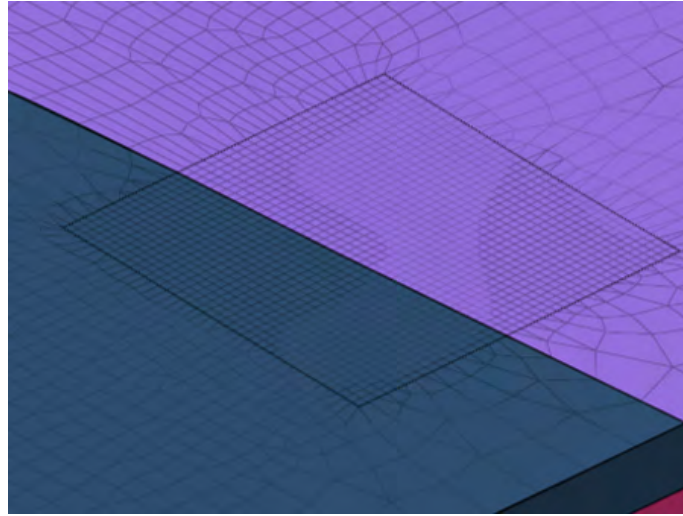


Figure 3.20: Discretized area around the German Continental Deep Drilling Programme with a refined lateral resolution of 500 m.

resolution of 500 m is around the area of the German Continental Deep Drilling Programme where most high-quality data are expected (Fig. 3.20). The vertical resolution is decreasing with depth. In the upper parts of the model that are relevant to be a potential host rock for a deep geological repository, the vertical resolution is as high as 10 m. The resolution gradually decreases towards the bottom of the model where a resolution of 500 m prevails. The vertical resolution does not vary laterally. The assignment of elements to the according lithological units is achieved using the Python tool ApplePy (Ziegler et al., 2020).

The underlying model assumptions are that a linear elastic rheology of the rock is sufficient to describe the present-day in-situ stress state. The model with correctly assigned lithologies is populated according with the rock properties. According to the model assumptions, the following three rock properties are required to be assigned to each lithological unit: 1) The rock stiffness in terms of the Young's modulus, 2) the Poisson ratio, and 3) the density of the rock that is decisive to model a reasonable overburden. The rock properties have been compiled from various literature sources, in particular relying on the German Continental Deep Drilling Programme with its extensive scientific output. The applied rock properties are listed in Table 3.2.

The model is calibrated using the Python software tool FAST Calibration (section 4.1). The reference stress data records required for the calibration procedure are taken exclusively from the stress magnitude database (section 2.1). The stress data records are weighted according to the stress magnitude quality ranking scheme (Morawietz et al., 2020). A successful calibration is performed and leads to a preliminary stress state that is shown in Figures 3.21 and 3.22.

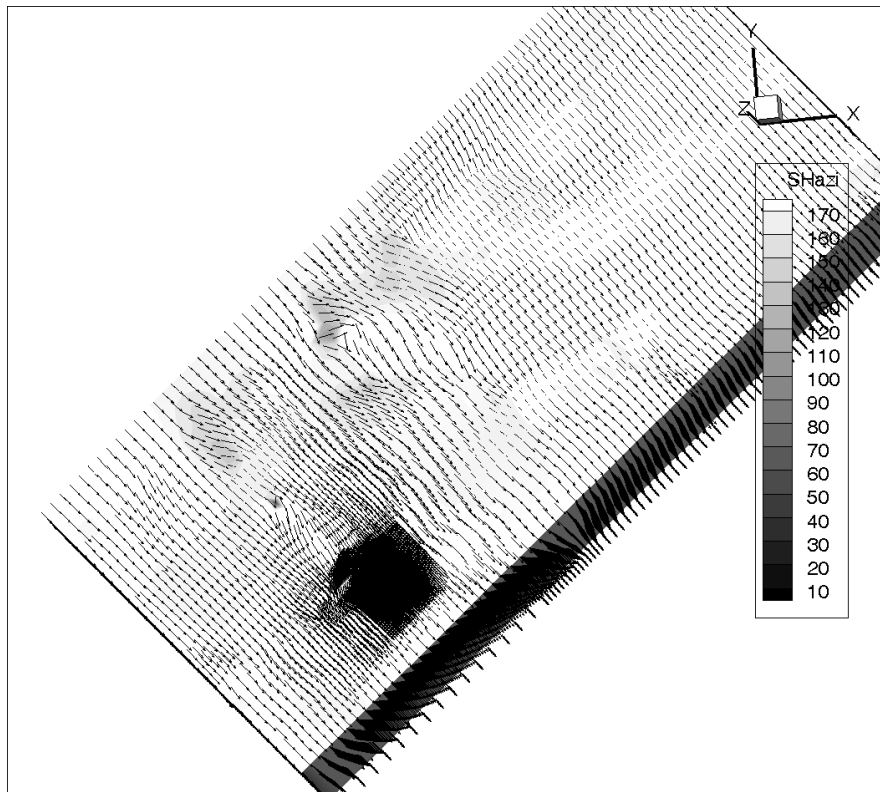


Figure 3.21: Preliminary orientation of the maximum horizontal stress component S_{Hmax} derived from the geomechanical model.

Outlook

The current status of the model is already far advanced and the works status is according to plan. The next anticipated steps for the modelling are:

- Estimation of a final best-fit stress state.
- Investigation of the model uncertainties due to stress magnitude data that are possibly contradicting.
- Comparison of the data-based calibration of the model with a submodelling approach using the geomechanical model of Germany (see section 2.2).
- Comparison of the stress state with a local-scale model of the area around the German Continental Deep Drilling Programme.

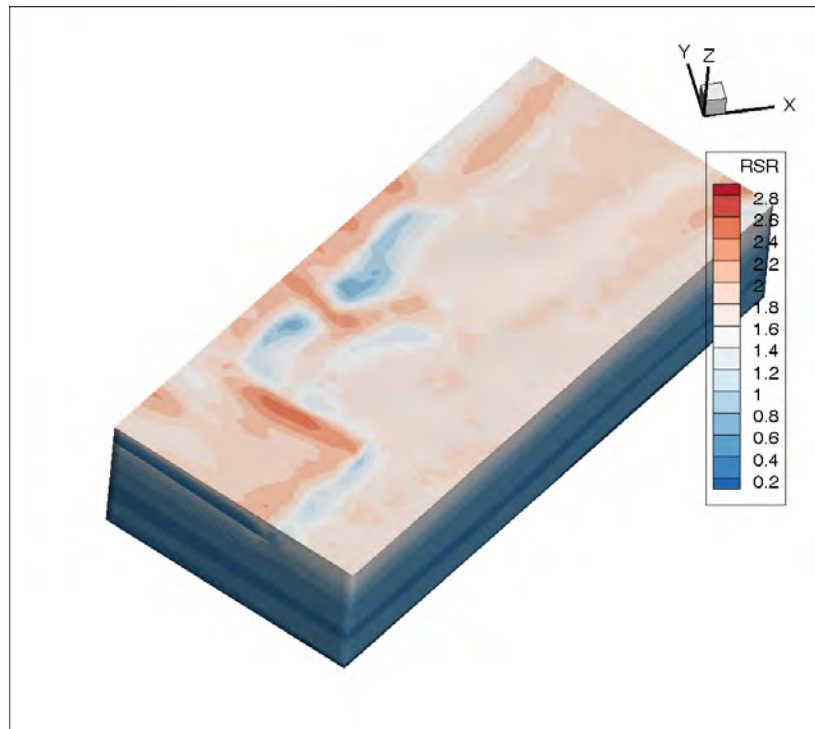


Figure 3.22: Preliminary Regime Stress Ratio (RSR) derived from the geomechanical model. The RSR is a value between 0 and 3 which indicates the tectonic stress regime from pure normal faulting (RSR = 0.5) via pure strike slip (RSR = 1.5) to pure thrust faulting (RSR = 2.5).

Table 3.2: Lithologies that are present in the model for siting region 009 and the according rock properties Young's modulus, Poisson ratio, and density.

Lithology	Young's modulus [GPa]	Poisson ratio [-]	Density [kg/m ³]
Cretaceous	20	0.25	2560
Jurassic	20	0.26	2650
Keuper	20	0.25	2700
Muschelkalk	40	0.25	2650
Buntsandstein	13	0.20	2660
Rotliegend Sediments	15	0.19	2600
Variscan Nappes	15	0.19	2650
Pre-Permian	40	0.25	2670
Upper Crust - Saxothuringian Zone	70	0.25	2730
Upper Crust - Moldanubian Zone	70	0.25	2690
Upper Crust - Bohemian granites	70	0.25	2670
Lower Crust - SE Germany	80	0.25	3000
Upper Mantle - Lithospheric	130	0.25	3300

4 Calibration data and exploration programmes (AP3)

4.1 Preparation of the tool FAST Calibration v2.0

Geomechanical-numerical modelling is widely used to predict the 3-D stress state in a confined volume. Such a modelling approach is based on the knowledge of the subsurface structure (geological layers, faults), rock density distribution and the elastic rock properties (Reiter and Heidbach, 2014; Hergert et al., 2015). Besides the volume forces due to gravity, the surface forces due to plate tectonics are introduced by Dirichlet displacement boundary conditions which are altered until the observed stress data at discrete points are fitted. Herein, this fitting process is referred to as model calibration. Once the displacement boundary conditions are found with which the model is best fitted to the stress data records the model is considered to be calibrated.

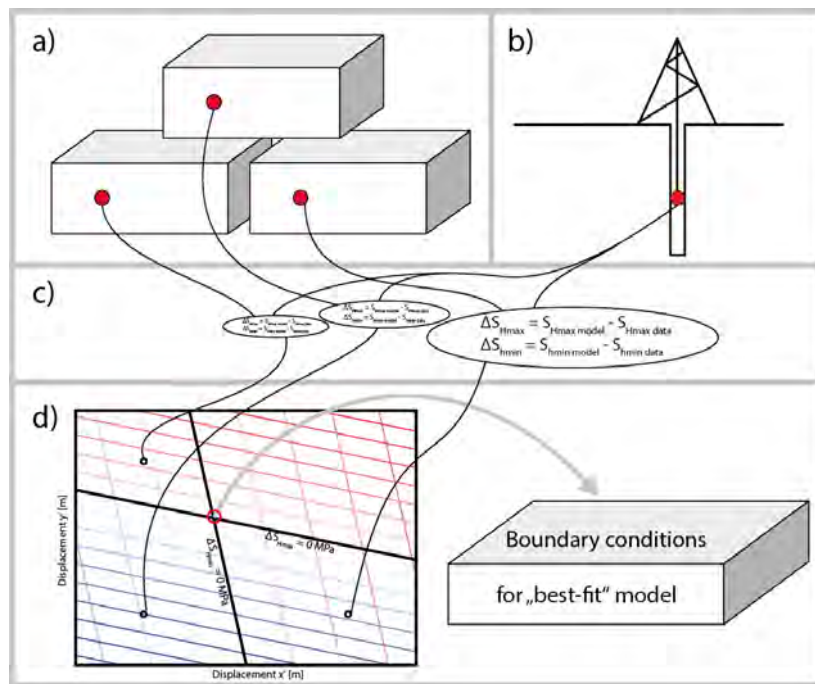


Figure 4.1: Basic workflow of the tool FAST Calibration. a) The stress state from three test model scenarios with arbitrary displacement boundary conditions and b) observed stress data records c) are compared. d) A set of linear equations is set up that provide the best-fit boundary conditions.

FAST Calibration (Fast Automatic Stress Tensor Calibration) is a Matlab and Python tool that controls the statistical calibration of a 3-D geomechanical-numerical model of the stress state following the approach described by Reiter and Heidbach (2014); Hergert et al. (2015); Ziegler et al. (2016); Ziegler and Heidbach (2020). Mainly it is used for the calibration of a single geomechanical-

numerical model. However, it also supports the multi-stage modelling procedure presented by Ziegler et al. (2016). The tools run in Matlab 2020a or Python 3.x and higher and are meant to work with the visualization software Tecplot 360 EX 2019 R1 and higher in conjunction with the Tecplot 360 Add-on GeoStress v2.0 (Heidbach et al., 2020). The user should be familiar with 3-D geomechanical-numerical modelling, Matlab/Python, Tecplot 360 EX, including a basic knowledge of Tecplot 360 EX macro functions, and the Tecplot 360 EX Add-on GeoStress v2.0 provided by Heidbach et al. (2020).

The calibration procedure is illustrated in Fig. 4.1. Three different test model scenarios with different arbitrary, but reasonable displacement boundary conditions are solved (Fig. 4.1 a). At several locations within the model volume stress data records are available (Fig. 4.1 b). For each test model scenario, the modelled stress state is compared with these stress data records. Each comparison provides a mean deviation for S_{Hmax} and S_{Hmin} , respectively (Fig. 4.1 c). A system of linear equations is set up in the domain of the displacement boundary conditions (x and y) and the deviations of observed and modelled data (z; Fig. 4.1 d). For the smallest deviation of each, S_{Hmax} or S_{Hmin} , an infinite number of corresponding displacement boundary conditions exist. However, only one set satisfies both the requirements for the smallest deviation in observed and modelled S_{Hmax} and S_{Hmin} . This set of displacement boundary conditions is applied to compute the best-fit model (see Ziegler et al., 2016).

While the Python tool is only designed for model calibration, the Matlab main script FAST_calibration.m not only controls the calibration of 3-D geomechanical-numerical models that use the Finite Element method. In addition, it provides the possibility for first order cross checking of the modelled stress state against other stress information that cannot be used for the calibration process, such as formation integrity tests, borehole breakouts, drilling induced tensile fractures, or the occurrence of seismicity (Figure 4.2). FAST Calibration evaluates if the model results agree with these observations. Based on the ratio of agreement vs. disagreement, an assessment on the predictive quality of the model is enabled.

The additional script (branch_calibration.m) is only required if a multistage-modelling approach is used as e.g., in a submodelling application. It controls the calibration of 3-D geomechanical-numerical models using the stress state retrieved from a larger stress model following the multi-stage procedure described by Ziegler et al. (2016). Basically, the script works in the same way as the script to calibrate the root model. The workflow is illustrated in Fig. 4.3. Three branch model scenarios with arbitrary but reasonable Dirichlet displacement boundary conditions are computed (Fig. 4.3 a). At defined locations within the best-fit root model which also lie within the branch models extent the modelled stress state is collected (Fig. 4.3 b). These synthetic stress data records need to be chosen with care (Ziegler et al., 2016). It is important to:

1. Only choose calibration points which are nodes in the model that provides the reference calibration points. Otherwise, the interpolation of the visualisation software from nodes into the volume may result in erroneous deviations.
2. The points used for calibration should be located at the border of the branch model. Otherwise, the stress field from the larger and less detailed root model is imposed everywhere in the branch model. Thereby no stress variations due to features that are only present in the branch model would be allowed. Suitable calibration points that adhere to these two rules are provided via subroutine.

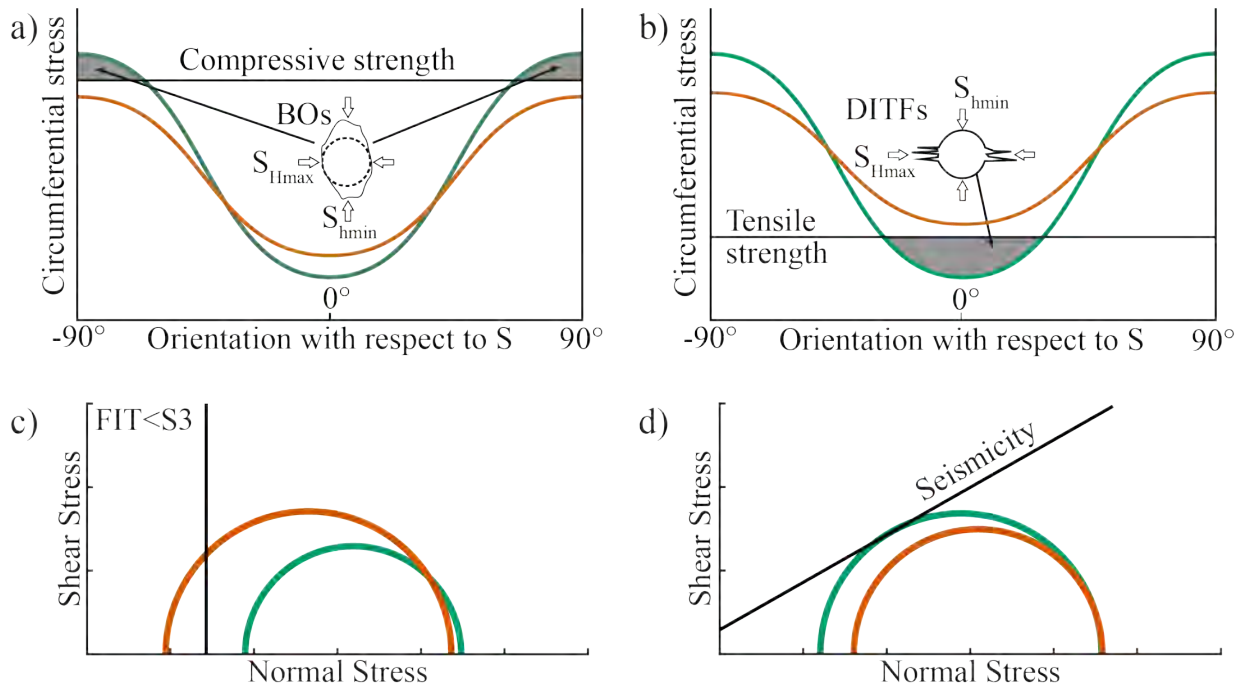


Figure 4.2: Two modelled stress states (red and green graphs) in comparison with four different types of indirect stress information. a) Borehole breakouts indicate that the maximum circumferential stress around the borehole wall exceeds the compressive strength of the rock. b) Drilling induced tensile fractures indicate that the minimum circumferential stress around the borehole wall is smaller than the tensile strength of the rock. c) Formation Integrity Tests provide a lower limit for the smallest stress component. d) Seismicity indicates that the failure envelope of a given criterion has been reached.

3. The material properties impose a restriction. Due to the modelling approach that uses displacement Dirichlet boundary conditions it is imperative that the synthetic data records locations in both models are in volumes characterised by the same material properties. The adherence of this rule needs to be enforced by the user, e.g., by using the root model geometry and rock materials at the boundaries of the branch model where synthetic data records are collected.

In the next step the stress state from the three branch test model scenarios is compared with the chosen calibration points from the best-fit root model and the deviation is computed for the S_{Hmax} and S_{Hmin} magnitudes in each test model scenario (Figure 4.3 c). A linear equation system is setup in the domain of the displacement boundary conditions and the deviations between the calibration points derived from the root stress state and the branch test model stress states (Fig. 4.3 d). The boundary conditions at this point are used to compute the best-fit branch model.

The manual of the Matlab script FAST Calibration v2.0 is published as a technical report (DOI: 10.48440/wsm.2021.002) and made available by the GFZ data service. The manual contains basic technical information on 3-D geomechanical-numerical modelling. Furthermore, the required and optional input data and the syntax are presented. It also includes the underlying concepts of the first order sanity-checks and quality assessment. The execution of the script FAST_calibration.m is explained in detail followed by a theoretical treatment of the multistage procedure and a detailed

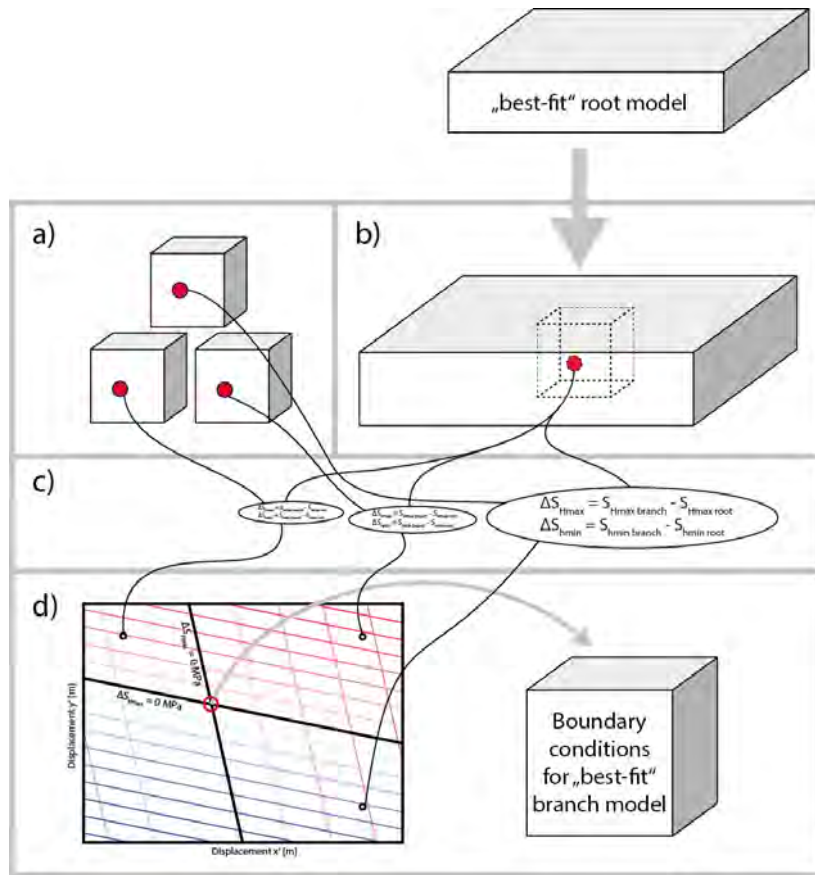


Figure 4.3: Workflow of the FAST Calibration multistage branch calibration. a) The stress state from three branch model scenarios with arbitrary boundary conditions and b) the modelled stress state from the root model c) are compared. d) A set of linear equations is set up that provide the best-fit boundary conditions for the branch model.

explanation of the execution of the `branch_calibration.m` script. Information on the individual Matlab functions that come with FAST Calibration are provided and mainly dedicated to advanced users. Eventually, two examples are provided – a basic geomechanical-numerical model calibration and an example for the application of the multistage approach.

The manual of the Python script `PyFAST Calibration` is published as a technical report (DOI: 10.48440/wsm.2021.003) and made available by the GFZ data service. The manual contains basic technical information on 3-D geomechanical-numerical modelling as well as information required for the successful application of the script. Furthermore, examples are provided.

Bibliography

- Aadnøy, B. S.: Inversion technique to determine the in-situ stress field from fracturing data, *Journal of Petroleum Science and Engineering*, 4, 127–141, [https://doi.org/10.1016/0920-4105\(90\)90021-T](https://doi.org/10.1016/0920-4105(90)90021-T), 1990.
- Abou-Sayed, A. S., Brechtel, C. E., and Clifton, R. J.: In situ stress determination by hydrofracturing: A fracture mechanics approach, *Journal of Geophysical Research*, 83, 2851, <https://doi.org/10.1029/jb083ib06p02851>, 1978.
- Addis, M., Hanssen, T., Yassir, N., Willoughby, D., and Enever, J.: A Comparison Of Leak-Off Test And Extended Leak-Off Test Data For Stress Estimation, in: *SPE/ISRM Rock Mechanics in Petroleum Engineering*, pp. 131–140, SPE, Trondheim, <https://doi.org/10.2118/47235-MS>, 1998.
- Ahlers, S., Henk, A., Hergert, T., Reiter, K., Müller, B., Röckel, L., Heidbach, O., Morawietz, S., Scheck-Wenderoth, M., and Anikiev, D.: 3D crustal stress state of Germany according to a data-calibrated geomechanical model, *Solid Earth*, 12, 1777–1799, <https://doi.org/10.5194/se-12-1777-2021>, 2021.
- Ahlers, S., Röckel, L., Hergert, T., Reiter, K., Heidbach, O., Henk, A., Müller, B., Morawietz, S., Scheck-Wenderoth, M., and Anikiev, D.: The crustal stress field of Germany: a refined prediction, *Geothermal Energy*, 10, <https://doi.org/10.1186/s40517-022-00222-6>, 2022.
- Ajalloeian, R. and Mohammadi, M.: Estimation of limestone rock mass deformation modulus using empirical equations, *Bulletin of Engineering Geology and the Environment*, 73, 541–550, 2014.
- Allen, P. A. and Allen, J. R.: *Basin analysis: Principles and application to petroleum play assessment*, John Wiley & Sons, 2013.
- Amadei, B. and Stephansson, O.: *Rock Stress and Its Measurement*, Chapman & Hall, London, 1997.
- Anikiev, D., Lechel, A., Laura Gomez Dacal, M., Bott, J., Cacace, M., and Scheck-Wenderoth, M.: A three-dimensional lithospheric-scale thermal model of Germany, *Advances in Geosciences*, 49, 225–234, <https://doi.org/10.5194/adgeo-49-225-2019>, 2019.
- Ask, D.: Evaluation of measurement-related uncertainties in the analysis of overcoring rock stress data from Äspö HRL, Sweden: a case study, *International Journal of Rock Mechanics and Mining Sciences*, 40, 1173–1187, 2003.
- Ask, D.: Methodology for determination of the complete stress tensor and its variation versus depth based on overcoring rock stress data, in: *Rock Mechanics and Engineering Volume 1: Principles*, edited by Feng, X.-T., pp. 245–265, CRC Press, <https://doi.org/10.1201/9781315364261-9>, 2017.
- Bachmann, G. H., Bayer, U., Duerbaum, H. J., Hoffmann, N., Krawczyk, C. M., Lueck, E., McCann, T., Meissner, R., Meyer, H., Oncken, O., Polom, U., Prochnow, U., Rabbel, W., Scheck, M., and

-
- Stiller, M.: Deep crustal structure of the Northeast German Basin; new DEKORP-BASIN '96 deep-profiling results, *Geology*, 27, 55–58, [https://doi.org/10.1130/0091-7613\(1999\)027<0055:DCSOTN>2.3.CO;2](https://doi.org/10.1130/0091-7613(1999)027<0055:DCSOTN>2.3.CO;2), 1999.
- Bär, K., Schäffer, R., Weinert, S., and Sass, I.: Verbundprojekt „Hessen 3D 2.0“ 3D-Modell der geothermischen Tiefenpotenziale von Hessen - Petrothermale Potenziale und Mitteltiefe Potenziale zur Wärmenutzung und Wärmespeicherung (Teilvorhaben A): Schlussbericht zum BMWi-geförderten Verbundprojekt „Hessen 3D 2.0“ (FKZ 0325944A), visited on 28.07.2022, 2021.
- Barton, C. A., Zoback, M. D., and Burns, K. L.: In-Situ Stress Orientation and Magnitude at the Fenton geothermal site, New Mexico, determined from wellbore breakouts, *Geophysical Research Letters*, 15, 467–470, 1988.
- Barton, N.: Some new Q-value correlations to assist in site characterisation and tunnel design, *International Journal of Rock Mechanics and Mining Sciences*, 39, 185–216, 2002.
- Barton, N., Lien, R., and Lunde, J.: Engineering classification of rock masses for the design of tunnel support, *Rock Mechanics Felsmechanik Mécanique des Roches*, 6, 189–236, <https://doi.org/10.1007/BF01239496>, 1974.
- Bayerisches Landesamt für Umwelt: Bayerischer Geothermieatlas, URL https://www.lfu.bayern.de/geologie/geothermie/geothermie_tief/geothermie_atlas/index.htm, 2022.
- Becker, a. and Werner, D.: Strain measurements with the borehole slotter, *Terra Nova*, 6, 608–617, <https://doi.org/10.1111/j.1365-3121.1994.tb00527.x>, 1994.
- Bell, J. S.: In situ stresses in sedimentary rocks (part 1); Measurement techniques, *Geoscience Canada*, 23, 85–100, 1996.
- Bertilsson, R.: Temperature effects in overcoring stress measurements, Ph.D. thesis, Luleå University of Technology, 2007.
- BGE: Gebiet zur Methodenentwicklung: Opalinuston, URL https://www.bge.de/fileadmin/user_upload/Standortsuche/Wesentliche_Unterlagen/Methodik/Phase_I_Schritt_2/04_Steckbrief_Gebiet_zur_Methodenentwicklung_Opalinuston_TG_001_00_barrierefrei.pdf, visited on 04.10.2023, 2021a.
- BGE: Gebiet zur Methodenentwicklung: Saxothuringikum, URL www.bge.de/fileadmin/user_upload/Standortsuche/Wesentliche_Unterlagen/Methodik/Phase_I_Schritt_2/03_Steckbriefe_Gebiete_zur_Methodenentwicklung_Saxothuringikum_TG_009_00_REV01_barrierefrei.pdf, visited on 04.10.2023, 2021b.
- BGE: Teilgebiet 001_00TG_032_01IG_T_f_jmOPT, URL <https://www.bge.de/de/endlagersuche/zwischenbericht-teilgebiete/001-00tg-032-01ig-t-f-jmopt>, visited on 04.10.2023, 2021c.
- BGR, LAGB, LBEG, LBGR, LLUR, and LUNG: 3D-Modell des geologischen Untergrundes des Norddeutschen Beckens (Projekt TUNB): Erstveröffentlichung 2021, Version 2022, URL <https://gst.bgr.de>, visited on 15.06.2022, 2022.

-
- Bieniawski, Z. T.: Engineering classification of jointed rock masses, Transactions of the South African Institution of Civil Engineers, 15, 335–343, 1973.
- Bieniawski, Z. T.: Determining rock mass deformability: experience from case histories, International Journal of Rock Mechanics and Mining Sciences & Geomechanics abstracts, 15, 237–247, 1978.
- Bieniawski, Z. T.: Engineering rock mass classifications, John Wiley & Sons, 1989.
- Blanton, T.: The relation between recovery deformation and in-situ stress magnitudes, in: SPE Rocky Mountain Petroleum Technology Conference/Low-Permeability Reservoirs Symposium, pp. SPE-11 624, SPE, 1983.
- Blundell, D., Freeman, R., and Mueller, S.: A continent revealed: the European Geotraverse, Cambridge Univ. Pr, Cambridge [u.a.], [https://doi.org/10.1016/0301-9268\(94\)90025-6](https://doi.org/10.1016/0301-9268(94)90025-6), 1992.
- Bock, H. and Foruria, V.: A recoverable borehole slotting instrument for in situ stress measurements in rocks not requiring overcoring, in: Field measurements in geomechanics. International symposium, pp. 15–29, 1984.
- Bock, H. F.: Measuring in situ rock stress by borehole slotting, in: Rock testing and site characterization, pp. 433–443, Elsevier, 1993.
- Brady, B. H. and Brown, E. T.: Rock mechanics: for underground mining, Springer science & business media, 2006.
- Braun, R., Jahns, E., and Stromeyer, D.: Determination of in-situ stress magnitudes and orientations with RACOS, Euroconference on Earth Stress and Industry. The World Stress Map and Beyond. Heidelberg, Germany, 1998.
- Breckels, I. and van Eekelen, H.: Relationship Between Horizontal Stress and Depth in Sedimentary Basins, Journal of Petroleum Technology, 34, 2191–2199, <https://doi.org/10.2118/10336-PA>, 1982.
- Bredehoeft, J. D., Wolff, R. G., Keys, W. S., and Shuter, E.: Hydraulic fracturing to determine the regional in situ stress field, Piceance Basin, Colorado, Geological Society of America Bulletin, 87, 250–258, [https://doi.org/10.1130/0016-7606\(1976\)87<250:HFTDTR>2.0.CO;2](https://doi.org/10.1130/0016-7606(1976)87<250:HFTDTR>2.0.CO;2), 1976.
- Carvalho, J.: Estimation of rock mass modulus, Personal communication, see Hoek & Diederichs (2006), 2004.
- Castillo, J. L.: Modified fracture pressure decline analysis including pressure-dependent leakoff, in: Society of Petroleum Engineers of AIME, (Paper) SPE, pp. 273–281, SPE, <https://doi.org/10.2118/16417-ms>, 1987.
- Cazes, M., Torreilles, G., Bois, C., Damotte, B., Galdeano, A., Hirn, A., Mascle, A., Matte, P., Van Ngoc, P., and Raoult, J. F.: Structure de la croûte hercynienne du Nord de la France; premiers résultats du profil ECORS, Bulletin de la Société Géologique de France, I, 925–941, <https://doi.org/10.2113/gssgfbull.I.6.925>, 1985.

-
- Chan, A., Hauser, M., Couzens-Schultz, B., and Gray, G.: The role of shear failure on stress characterization, *Rock mechanics and rock engineering*, 47, 1641–1646, 2014.
- Cornet, F.: Stress determination from hydraulic tests on preexisting fractures-the HTPF method, in: *ISRM International Symposium*, pp. ISRM-IS, ISRM, 1986.
- Cornet, F. H.: *Elements of Crustal Geomechanics*, Cambridge University Press, <https://doi.org/10.1017/CBO9781139034050>, 2015.
- Couzens-Schultz, B. a. and Chan, A. W.: Stress determination in active thrust belts: An alternative leak-off pressure interpretation, *Journal of Structural Geology*, 32, 1061–1069, <https://doi.org/10.1016/j.jsg.2010.06.013>, 2010.
- Cundall, P.: Lattice method for modeling brittle, jointed rock, in: *Continuum and Distinct Element Numerical Modeling in Geomechanics*, Proceedings of the 2nd International FLAC/DEM Symposium, Melbourne, Australia, pp. 14–16, 2011.
- Danielson, J. J. and Gesch, D. B.: Global multi-resolution terrain elevation data 2010 (GMTED2010): Mean Statistic, 30 arc-seconds, <https://doi.org/10.3133/ofr20111073>, 2011.
- Deckers J., De Koninck R., Bos S., Broothaers M., Dirix K., Hamsch L., Lagrou, D., and Lanckacker T.: Geologisch (G3Dv3) en hydrogeologisch (H3D) 3D-lagenmodel van Vlaanderen, URL <https://www.dov.vlaanderen.be/page/geologisch-3d-model-g3dv3>, visited on 16.12.2022, 2019.
- DEKORP Research Group: Results of deep reflection seismic profiling in the Oberpfalz (Bavaria), *Geophysical Journal International*, 89, 353–360, <https://doi.org/10.1111/j.1365-246X.1987.tb04430.x>, 1987.
- DEKORP Research Group, Behr, H.-J., Dürbaum, H.-J., Bankwitz, P., Bankwitz, E., Benek, R., Berger, H.-J., Brause, H., Conrad, W., Förste, K., Frischbutter, A., Gebrande, H., Giese, P., Göthe, W., Gürtler, J., Hänig, D., Haupt, M., Heinrichs, T., Horst, W., Hurtig, E., Kämpf, H., Kramer, W., Krentz, O., Lang, M., Lorenz, W., Lück, E., Müller, H. J., Raab, S., Rabbel, W., Rauche, H., Ritter, E., Schulze, A., Schwarz, G., Seifert, W., Springer, M., Tauber, S., and Trzebski, R.: Crustal structure of the Saxothuringian Zone: Results of the deep seismic profile MVE-90(East), *Z. Geol. Wiss.*, 22, 647–769, 1994.
- Desroches, J. and Kurkjian, A. L.: Applications of wireline stress measurements, *SPE Reservoir Evaluation and Engineering*, 2, 451–461, <https://doi.org/10.2118/58086-PA>, 1999.
- Desroches, J., Peyret, E., Gisolf, A., Wilcox, A., Di Giovanni, M., de Jong, A. S., Sepehri, S., Garrard, R., and Giger, S.: Stress Measurement Campaign in Scientific Deep Boreholes: Focus on Tool and Methods, in: *SPWLA 62nd*, <https://doi.org/10.30632/spwla-2021-0056>, 2021.
- Detournay, E. and Carbonell, R.: Fracture-mechanics analysis of the breakdown process in minifracture or leakoff test, *SPE Production and Facilities*, 12, 195–199, <https://doi.org/10.2118/28076-PA>, 1997.

-
- Diepolder, G., Allenbach, R., Baumberger, R., Bottig, M., Brenot, A., Brüstle, A., Cagnoni, A., Laure, C., Coueffe, R., D'Ambrogi, C., Dezayes, C., Stucki, M., Fehn, C., Ferri, F., Gabalda, S., Gabriel, P., Gietzel, J., Goetzl, G., Koren, K., and Zumsprekel, H.: GeoMol – Assessing subsurface potentials of the Alpine Foreland Basins for sustainable planning and use of natural resources. Project Report, <https://doi.org/10.13140/RG.2.2.15693.36328>, 2015.
- Domínguez-Gonzalez, L. and Andreani, L.: Geologisches 3D Modell des Zittauer Beckens, Tech. rep., Technische Universität Bergakademie Freiberg, 2013.
- Domínguez-Gonzalez, L. and Andreani, L.: Geologisches 3D Modell von Zittau, Tech. rep., Technische Universität Bergakademie Freiberg, 2015a.
- Domínguez-Gonzalez, L. and Andreani, L.: Geologisches 3D Modell von Oderwitz, Tech. rep., Technische Universität Bergakademie Freiberg, 2015b.
- Domínguez-Gonzalez, L. and Andreani, L.: Geologisches 3D Modell von Nochten, Tech. rep., Technische Universität Bergakademie Freiberg, 2015c.
- Domínguez-Gonzalez, L. and Andreani, L.: Geologisches 3D Modell von Berzdorf, Tech. rep., Technische Universität Bergakademie Freiberg, 2015d.
- Donner, E.: Geologisches 3D Modell Niederbayern, URL <https://www.3dportal.lfu.bayern.de/>, visited on 04.10.2022, 2020.
- Enderle, Schuster, Prodehl, Schulze, and Bribach: The refraction seismic experiment GRANU95 in the Saxothuringian belt, southeastern Germany, *Geophysical Journal International*, 133, 245–259, <https://doi.org/10.1046/j.1365-246X.1998.00462.x>, 1998.
- Enever, J. and Chopra, P.: Experience with hydraulic fracture stress measurements in granite, in: *ISRM International Symposium*, pp. ISRM–IS, ISRM, 1986.
- Enever, J., Yassir, N., Willoughby, D., and Addis, M.: Recent experience with extended leak-off tests for in-situ stress measurements in Australia, *The APPEA Journal*, 36, 528–535, 1996.
- English, J. M., Finkbeiner, T., English, K. L., and Cherif, R. Y.: State of stress in exhumed basins and implications for fluid flow: Insights from the Illizi Basin, Algeria, *Geological Society Special Publication*, 458, 89–111, <https://doi.org/10.1144/SP458.6>, 2017.
- Evans, K. F., Engelder, T., and Plumb, R. A.: Appalachian Stress Study: 1. A detailed description of in situ stress variations in Devonian shales of the Appalachian Plateau, *Journal of Geophysical Research*, 94, 7129, <https://doi.org/10.1029/JB094iB06p07129>, 1989.
- Fairhurst, C.: Measurement of in-situ rock stresses. With particular reference to hydraulic fracturing, *Rock Mech. Eng. Geol.*, 2, 1964.
- Fazlikhani, H., Bauer, W., and Stollhofen, H.: Variscan structures and their control on latest to post-Variscan basin architecture: insights from the westernmost Bohemian Massif and southeastern Germany, *Solid Earth*, 13, 393–416, <https://doi.org/10.5194/se-13-393-2022>, 2022.

-
- Figueiredo, B., Cornet, F., Lamas, L., and Muralha, J.: Determination of the stress field in a mountainous granite rock mass, *International Journal of Rock Mechanics and Mining Sciences*, 72, 37–48, 2014.
- Funato, A. and Ito, T.: A new method of diametrical core deformation analysis for in-situ stress measurements, *International Journal of Rock Mechanics and Mining Sciences*, 91, 112–118, <https://doi.org/10.1016/j.ijrmms.2016.11.002>, 2017.
- Gajewski, D., Holbrook, W. S., and Prodehl, C.: A three-dimensional crustal model of southwest Germany derived from seismic refraction data, *Tectonophysics*, 142, 49–70, 1987.
- Galera, J. M., Álvarez, M., and Bieniawski, Z. T.: Evaluation of the deformation modulus of rock masses using RMR. Comparison with dilatometer tests., in: *Workshop: Underground Works under Special Conditions*, 2007.
- Gardner, W. S.: Design of drilled piers in the Atlantic Piedmont, in: *Foundations and Excavations in Decomposed Rock of the Piedmont Province*, pp. 62–86, ASCE, 1987.
- GEBCO Bathymetric Compilation Group: The GEBCO_2022 Grid - a continuous terrain model of the global oceans and land, <https://doi.org/10.5285/e0f0bb80-ab44-2739-e053-6c86abc0289c>, 2022.
- Geological Survey of the Netherlands: Digital Geological Model (DGM) deep V5 on- and offshore, URL <https://www.nlog.nl/en/dgm-deep-v5-and-offshore>, visited on 24.10.2022, 2019.
- Geologischer Dienst Nordrhein-Westfalen: Landesmodell NRW, URL https://www.gd.nrw.de/ge_eb_3d_modelle.htm, visited on 15.09.2022, 2014.
- GeoMol LCA-Projectteam: GeoMol pilot area Lake Constance - Allgäu (Bavaria), URL <https://www.3dportal.lfu.bayern.de/>, visited on 04.10.2022, 2015a.
- GeoMol LCA-Projectteam: GeoMol pilot area Lake Constance - Allgäu (Baden-Wuerttemberg), URL <http://maps.geomol.eu/>, visited on 10.10.2022, 2015b.
- GeoMol Team: GeoMol framework model (Bavaria), URL <https://www.3dportal.lfu.bayern.de/>, visited on 04.10.2022, 2015.
- GeoMol UA-UB-Projectteam: GeoMol pilot area Upper Austria – Upper Bavaria (Bavaria), URL <https://www.3dportal.lfu.bayern.de/>, visited on 04.10.2022, 2015.
- GeORG-Projektteam: Geopotentiale des tieferen Untergrundes im Oberrheingraben. Fachlich-Technischer Abschlussbericht des INTERREG-Projekts GeORG, Tech. rep., Teil 4, Freiburg i. Br., 2013.
- Görne, S.: Geologisches 3D Modell Aue, Tech. rep., Sächsisches Landesamt für Umwelt, Landwirtschaft und Geologie, 2010a.
- Görne, S.: Geologisches 3D Modell Annaberg, Tech. rep., Sächsisches Landesamt für Umwelt, Landwirtschaft und Geologie, 2010b.

-
- Görne, S.: Geologisches 3D Modell NW-Sachsen, Tech. rep., Sächsisches Landesamt für Umwelt, Landwirtschaft und Geologie, URL <http://lsnq.de/3dnwsachsen>, 2011.
- Görne, S.: Geologisches 3D Modell des "Zwischengebietes", Tech. rep., Sächsisches Landesamt für Umwelt, Landwirtschaft und Geologie, URL <http://lsnq.de/3dzwischen>, visited on 10.08.2022, 2012a.
- Görne, S.: Geologisches 3D Modell der Elbtalzone, Tech. rep., Sächsisches Landesamt für Umwelt, Landwirtschaft und Geologie, 2012b.
- Görne, S. and Geißler, V.: Geologisches 3D Modell der Niederlausitz, Tech. rep., Sächsisches Landesamt für Umwelt, Landwirtschaft und Geologie, URL <http://lsnq.de/3dniedlau>, 2015.
- Görne, S. and Steinborn, H.: Geologisches 3D Modell Lugau-Oelsnitz (Erzgebirge), Tech. rep., Sächsisches Landesamt für Umwelt, Landwirtschaft und Geologie, 2007.
- Görne, S. and Steinborn, H.: Geologisches 3D Modell der Vorerzgebirgssenke (VES), Tech. rep., Sächsisches Landesamt für Umwelt, Landwirtschaft und Geologie, 2014.
- Görne, S. and Wener, D.: Geologisches 3D Modell Kohlberg, Tech. rep., Sächsisches Landesamt für Umwelt, Landwirtschaft und Geologie and Technische Universität Bergakademie Freiberg, 2015.
- Gottron, D.: Concepts for upscaling hydromechanical properties of fractured rock masses - a comparison of classification schemes, discrete fracture network and synthetic rock mass models, Ph.D. thesis, Technische Universität Darmstadt, Darmstadt, <https://doi.org/https://doi.org/10.26083/tuprints-00022459>, 2022.
- Gottron, D. and Henk, A.: Upscaling of fractured rock mass properties—An example comparing Discrete Fracture Network (DFN) modeling and empirical relations based on engineering rock mass classifications, *Engineering Geology*, 294, 106–382, <https://doi.org/10.1016/j.enggeo.2021.106382>, 2021.
- Gottron, D. and Henk, A.: Upscaling the Mechanical Properties of a Fractured Rock Mass Using the Lattice-Spring-Based Synthetic Rock Mass (LS-SRM) Modeling Approach — Comparison of Discontinuum, Continuum and Empirical Approaches, *Geosciences*, 12, <https://doi.org/10.3390/geosciences12090343>, 2022.
- Grad, M., Brückl, E., Majdański, M., Behm, M., and Guterch, A.: Crustal structure of the Eastern Alps and their foreland: seismic model beneath the CEL10/Alp04 profile and tectonic implications, *Geophys. J. Int.*, 177, 279–295, <https://doi.org/10.1111/j.1365-246X.2008.04074.x>, 2009a.
- Grad, M., Tiira, T., and Group, E. W.: The Moho depth map of the European Plate, *Geophysical Journal International*, 176, 279–292, <https://doi.org/10.1111/j.1365-246X.2008.03919.x>, 2009b.
- Guo, F., Morgenstern, N. R., and Scott, J. D.: Interpretation of hydraulic fracturing breakdown pressure, *International Journal of Rock Mechanics and Mining Sciences* and, 30, 617–626, [https://doi.org/10.1016/0148-9062\(93\)91221-4](https://doi.org/10.1016/0148-9062(93)91221-4), 1993.

-
- Guy, A., Edel, J.-B., Schulmann, K., Tomek, Ā., and Lexa, O.: A geophysical model of the Variscan orogenic root (Bohemian Massif): Implications for modern collisional orogens, *Lithos*, 124, 144–157, <https://doi.org/10.1016/j.lithos.2010.08.008>, 2011.
- Haimson, B.: Hydraulic fracturing in porous and nonporous rock and its potential for determining in-situ stresses at great depth, University of Minnesota, 1968.
- Haimson, B. and Fairhurst, C.: Initiation and Extension of Hydraulic Fractures in Rocks, *Society of Petroleum Engineers Journal*, 7, 310–318, <https://doi.org/10.2118/1710-pa>, 1967.
- Haimson, B. C. and Cornet, F. H.: ISRM suggested methods for rock stress estimation-part 3: Hydraulic fracturing (HF) and/or hydraulic testing of pre-existing fractures (HTPF), *International Journal of Rock Mechanics and Mining Sciences*, 40, 1011–1020, <https://doi.org/10.1016/j.ijrmms.2003.08.002>, 2003.
- Haimson, B. C. and Fairhurst, C.: In-situ stress determination at great depth by means of hydraulic fracturing, in: *The 11th U.S. Symposium on Rock Mechanics (USRMS)*, 16-19 June, Berkeley, California, pp. 559–584, American Rock Mechanics Association, 1969.
- Haimson, B. C. and Song, I.: Laboratory study of borehole breakouts in Cordova Cream: a case of shear failure mechanism, *International Journal of Rock Mechanics and Mining Sciences & Geomechanics Abstracts*, 30, 1047–1056, [https://doi.org/10.1016/0148-9062\(93\)90070-T](https://doi.org/10.1016/0148-9062(93)90070-T), 1993.
- Hakala, M.: Quality Controll for Overcoring Stress Measurement Data – POSIVA 2006-03, Tech. rep., Gridpoint Finland Oy, 2007.
- Hakala, M., Hudson, J. A., and Christiansson, R.: Quality control of overcoring stress measurement data, *International Journal of Rock Mechanics and Mining Sciences*, 40, 1141–1159, <https://doi.org/10.1016/j.ijrmms.2003.07.005>, 2003.
- Hast, N.: The measurement of rock pressure in mines, *Sveriges Geol. Undersokn. Arsbok*, C, Avhandl. Uppsat., 52, 1958.
- Heidbach, O., Rajabi, M., Cui, X., Fuchs, K., Müller, B., Reinecker, J., Reiter, K., Tingay, M., Wenzel, F., Xie, F., Ziegler, M. O., Zoback, M.-L., and Zoback, M. D.: The World Stress Map database release 2016: Crustal stress pattern across scales, *Tectonophysics*, 744, 484–498, <https://doi.org/10.1016/j.tecto.2018.07.007>, 2018.
- Heidbach, O., Ziegler, M. O., and Stromeyer, D.: Manual of the Tecplot 360 Add-on GeoStress v2.0, Tech. rep., GFZ Data Service, <https://doi.org/10.2312/wsm.2020.001>, 2020.
- Heinrichs, T., Giese, P., Bankwitz, P., and Bankwitz, E.: DEKORP 3 / MVE-90 (West) - preliminary geological interpretation of a deep near-vertical reflection profile between the Rhenish and the Bohemian Massifs , Germany, *Z. Geol. Wiss.*, 22, 771–801, 1994.
- Hergert, T. and Heidbach, O.: Slip-rate variability and distributed deformation in the Marmara Sea fault system, *Nature Geoscience*, 3, 132–135, <https://doi.org/10.1038/ngeo739>, 2010.

-
- Hergert, T. and Heidbach, O.: Geomechanical model of the Marmara Sea region-II. 3-D contemporary background stress field, *Geophysical Journal International*, 185, 1090–1102, <https://doi.org/10.1111/j.1365-246X.2011.04992.x>, 2011.
- Hergert, T., Heidbach, O., Reiter, K., Giger, S. B., and Marschall, P.: Stress Field Sensitivity Analysis at a Reservoir Scale (Northern Switzerland) Using Numerical Geomechanical Modelling, *Solid Earth*, 6, 533–552, <https://doi.org/10.5194/se-6-533-2015>, 2015.
- Hergert, T., Ahlers, S., Röckel, L., Morawietz, S., Reiter, K., Ziegler, M., Müller, B., Heidbach, O., Schilling, F., and Henk, A.: On the influence of initial stress on final stress in data-calibrated numerical geomechanical models, *Safety of Nuclear Waste Disposal*, 2, 65–64, 2023.
- Hickman, S. H. and Zoback, M. D.: The interpretation of hydraulic fracturing pressure-time data for in situ stress determination, in: *Hydraulic Fracturing Stress Measurements*, edited by Hickman, S. H. and Zoback, M. D., chap. 1.4, pp. 44–54, Office of Earthquakes, Volcanoes, and Engineering, 1983.
- Hoek, E.: Strength of rock and rock masses, *International Society of Rock Mechanics New Journal*, 2, 4–16, 1994.
- Hoek, E. and Brown, E.: Practical estimates of rock mass strength, *International Journal of Rock Mechanics and Mining Sciences*, 34, 1165–1186, [https://doi.org/https://doi.org/10.1016/S1365-1609\(97\)80069-X](https://doi.org/10.1016/S1365-1609(97)80069-X), 1997.
- Hoek, E. and Diederichs, M. S.: Empirical estimation of rock mass modulus, *International Journal of Rock Mechanics and Mining Sciences*, 43, 203–215, <https://doi.org/10.1016/j.ijrmms.2005.06.005>, 2006.
- Hoek, E., Carter, T., and Diederichs, M.: Quantification of the geological strength index chart, in: *47th US rock mechanics/geomechanics symposium*, OnePetro, 2013.
- Hrubcová, P., Šroda, P., Špicák, A., Guterch, A., Grad, M., Keller, G. R., Brueckl, E., and Thybo, H.: Crustal and uppermost mantle structure of the Bohemian Massif based on CELEBRATION 2000 data, *Journal of Geophysical Research: Solid Earth*, 110, <https://doi.org/10.1029/2004JB003080>, 2005.
- Hubbert, K. M. and Willis, D. G.: Mechanics of hydraulic fracturing, *AIME Petroleum Transactions*, 210, 153–168, [https://doi.org/10.1016/S0376-7361\(07\)53011-6](https://doi.org/10.1016/S0376-7361(07)53011-6), 1957.
- Hurter, S. and Haenel, R.: Atlas of geothermal resources in the European Community, Austria and Switzerland, European Commission, Publ. EUR, 17811, 2002.
- Hurtig, E., Cermak, V., Haenel, R., and Zui, V.: Geothermal Atlas of Europe, Haack, Gotha, 1992.
- Irvin, R., Garritty, P., and Farmer, I.: The effect of boundary yield on the results of in situ stress measurements using overcoring techniques, *International Journal of Rock Mechanics and Mining Sciences & Geomechanics Abstracts*, 24, 89–93, 1987.

-
- Ito, T., Evans, K. F., Kawai, K., and Hayashi, K.: Hydraulic fracture reopening pressure and the estimation of maximum horizontal stress, *International Journal of Rock Mechanics and Mining Sciences*, 36, 811–826, [https://doi.org/10.1016/S0148-9062\(99\)00053-4](https://doi.org/10.1016/S0148-9062(99)00053-4), 1999.
- Jaeger, J. C., Cook, N., and Zimmerman, R.: *Fundamentals of rock mechanics*, Blackwell, Hoboken, New Jersey, 4th edn., 2011.
- Jamshidi, A.: Investigating the effect of specimen diameter size on uniaxial compressive strength and elastic properties of travertines, *Journal of Sciences, Islamic Republic of Iran*, 25, 133–141, 2014.
- Janik, T., Grad, M., Guterch, A., Vozár, J., Bielik, M., Vozárova, A., Hegedus, E., Kovács, C. A., Kovács, I., and Keller, G. R.: Crustal structure of the Western Carpathians and Pannonian Basin: Seismic models from CELEBRATION 2000 data and geological implications, *Journal of Geodynamics*, 52, 97–113, <https://doi.org/10.1016/j.jog.2010.12.002>, 2011.
- Kehle, R. O.: The Determination of Tectonic Stresses through Analysis of Hydraulic Well Fracturing, *Journal of Geophysical Research*, 69, 259–273, <https://doi.org/10.1029/JZ069i002p00259>, 1964.
- Kirsch, M., Kroner, U., Hallas, P., and Stephan, T.: 3D Model of the Erzgebirge - Crustal-Scale 3D Modelling of the Allochthonous Domain of the Saxo-Thuringian Zone, URL <https://tu-freiberg.de/geo/tectono/3d-erzgebirge>, visited on 09.12.2022, 2017.
- Kogan, I., Sattler, S., and Görne, S.: *Geologisches 3D Modell der Mügelner Senke*, Tech. rep., Sächsisches Landesamt für Umwelt, Landwirtschaft und Geologie and Technische Universität Bergakademie Freiberg, 2009.
- Korsch, R. and Schäfer, A.: The Permo-Carboniferous Saar-Nahe Basin, south-west Germany and north-east France: basin formation and deformation in a strike-slip regime, *Geologische Rundschau*, 84, <https://doi.org/10.1007/BF00260442>, 1995.
- Kruszewski, M., Klee, G., Niederhuber, T., and Heidbach, O.: In situ stress database of the greater Ruhr region (Germany) derived from hydrofracturing tests and borehole logs, *Earth System Science Data*, 14, 5367–5385, <https://doi.org/10.5194/essd-14-5367-2022>, 2022.
- Kunze, K. R. and Steiger, R. P.: Extended leakoff tests to measure in situ stress during drilling, in: *ARMA US Rock Mechanics/Geomechanics Symposium*, pp. ARMA–91, ARMA, 1991.
- Lee, M. and Haimson, B.: Laboratory study of borehole breakouts in Lac du Bonnet granite: a case of extensile failure mechanism, *International Journal of Rock Mechanics and Mining Sciences & Geomechanics abstracts*, 30, 1039–1045, [https://doi.org/10.1016/0148-9062\(93\)90069-P](https://doi.org/10.1016/0148-9062(93)90069-P), 1993.
- Leeman, E.: The Measurement of Stress in Rock: Part I, II and II, *Journal of South African Institute of Mining and Metallurgy*, 65, 45–114, 1964.
- Leeman, E.: The determination of the complete state of stress in rock in a single borehole—Laboratory and underground measurements, *International Journal of Rock Mechanics and Mining Sciences & Geomechanics Abstracts*, 5, 31–56, [https://doi.org/10.1016/0148-9062\(68\)90021-1](https://doi.org/10.1016/0148-9062(68)90021-1), 1968.

-
- Leijon, B.: Relevance of pointwise rock stress measurements—an analysis of overcoring data, *International Journal of Rock Mechanics and Mining Sciences & Geomechanics Abstracts*, 26, 61–68, 1989.
- Li, G., Lorwongngam, A., and Roegiers, J.-C.: Critical Review Of Leak-Off Test As A Practice For Determination Of In-Situ Stresses, in: 43rd US Rock Mechanics Symposium and 4th U.S.-Canada Rock Mechanics Symposium, p. 5, American Rock Mechanics Association, Asheville, 2009.
- Li, X., Hergert, T., Henk, A., and Zeng, Z.: Contemporary kinematics in the eastern Tibetan Plateau: Insights from 3D geomechanical modeling, *Tectonophysics*, 819, 229–109, <https://doi.org/10.1016/j.tecto.2021.229109>, 2021.
- Lindner, H., Scheibe, R., Seidel, K., and Hoffmann, N.: Berechnung von Relief, Tiefenlage und Magnetisierung des magnetisch wirksamen Kristallins für das Norddeutsche Becken, *Zeitschrift für Angewandte Geologie*, 50, 65–73, 2004.
- Linnemann, U. and Romer, R. L., eds.: Pre-Mesozoic geology of Saxo-Thuringia: From the Cadomian active margin to the Variscan orogen, Schweizerbart, Stuttgart, 2010.
- Liu, L., Li, L., Elsworth, D., Zhi, S., and Yu, Y.: The impact of oriented perforations on fracture propagation and complexity in hydraulic fracturing, *Processes*, 6, <https://doi.org/10.3390/pr6110213>, 2018.
- Ljunggren, C., Chang, Y., Janson, T., and Christiansson, R.: An overview of rock stress measurement methods, *International Journal of Rock Mechanics and Mining Sciences*, 40, 975–989, <https://doi.org/10.1016/j.ijrmms.2003.07.003>, 2003.
- Lowson, A. and Bieniawski, Z. T.: Critical assessment of RMR based tunnel design practices: a practical engineer's approach, in: *Proceedings of the SME, rapid excavation and tunnelling conference*, Washington, DC, pp. 180–198, 2013.
- Maystrenko, Y. P. and Scheck-Wenderoth, M.: 3D lithosphere-scale density model of the Central European Basin System and adjacent areas, *Tectonophysics*, 601, 53–77, <https://doi.org/10.1016/j.tecto.2013.04.023>, 2013.
- McGarr, A.: On the State of Lithospheric Stress in the Absence of Applied Tectonic Forces, *Journal of Geophysical Research*, 93, 13 609, <https://doi.org/10.1029/JB093iB11p13609>, 1988.
- Meschede, M. and Warr, L. N.: *The Geology of Germany*, Springer, <https://doi.org/10.1007/978-3-319-76102-2>, 2019.
- Mishra, V. K., Lywood, P., and Ayan, C.: Application of wireline stress testing for SAGD caprock integrity, *Society of Petroleum Engineers - Canadian Unconventional Resources Conference 2011, CURC 2011*, 3, 2184–2195, <https://doi.org/10.2118/149456-ms>, 2011.
- Mitri, H., Edrissi, R., and Henning, J.: Finite element modeling of cable-bolted stopes in hard rock underground mines Presented at the SME annual meeting, Albuquerque, New Mexico, 4, 1994.

-
- Moos, D. and Zoback, M. D.: Utilization of observations of well bore failure to constrain the orientation and magnitude of crustal stresses: Application to continental, Deep Sea Drilling Project, and Ocean Drilling Program boreholes, *Journal of Geophysical Research*, 95, 9305, <https://doi.org/10.1029/JB095iB06p09305>, 1990.
- Morawietz, S., Heidbach, O., Reiter, K., Ziegler, M. O., Rajabi, M., Zimmermann, G., Müller, B. B., and Tingay, M.: An open - access stress magnitude database for Germany and adjacent regions, *Geothermal Energy*, 8, 39, <https://doi.org/10.1186/s40517-020-00178-5>, 2020.
- NAGRA: Sondierbohrung Benken: Technical Report NTB 00-01, Tech. rep., Nationale Genossenschaft für die Lagerung radioaktiver Abfälle, Wettingen, 2001.
- Nicholson, G. and Bieniawski, Z. T.: A nonlinear deformation modulus based on rock mass classification, *International Journal of Mining and geological engineering*, 8, 181–202, 1990.
- Oda, M.: Permeability tensor for discontinuous rock masses, *Géotechnique*, 35, 483–495, <https://doi.org/10.1680/geot.1985.35.4.483>, 1985.
- Oda, M.: An equivalent continuum model for coupled stress and fluid flow analysis in jointed rock masses, *Water resources research*, 22, 1845–1856, <https://doi.org/10.1029/WR022i013p01845>, 1986.
- Oncken, O., Plesch, A., Weber, J., Ricken, W., and Schrader, S.: Passive margin detachment during arc-continent collision (Central European Variscides), *Geological Society Special Publication*, 179, 199–216, <https://doi.org/10.1144/GSL.SP.2000.179.01.13>, 2000.
- Peška, P., , and Zoback, M. D.: Compressive and tensile failure of inclined well bores and determination of in situ stress and rock strength, *Journal of Geophysical Research*, 100, 12 791–12 811, <https://doi.org/10.1029/95JB00319>, 1995.
- Pierce, M., Cundall, P., Potyondy, D., and Ivars, D. M.: A Synthetic Rock Mass Model For Jointed Rock, in: *ARMA Canada-US Rock Mechanics Symposium*, vol. *All Days of Canada - U.S. Rock Mechanics Symposium*, pp. ARMA–07, ARMA, URL <https://onepetro.org/ARMACUSRMS/proceedings-pdf/ARMA07/All-ARMA07/ARMA-07-042/1800894/arma-07-042.pdf>, aRMA-07-042, 2007.
- Prijac, C., Doin, M., Gaulier, J., and Guillocheau, F.: Subsidence of the Paris Basin and its bearing on the late Variscan lithosphere evolution: a comparison between Plate and Chablis models, *Tectonophysics*, 323, 1–38, [https://doi.org/10.1016/S0040-1951\(00\)00100-1](https://doi.org/10.1016/S0040-1951(00)00100-1), 2000.
- Raaen, A. M., Horsrud, P., Kjørholt, H., and Økland, D.: Improved routine estimation of the minimum horizontal stress component from extended leak-off tests, *International Journal of Rock Mechanics and Mining Sciences*, 43, 37–48, <https://doi.org/10.1016/j.ijrmms.2005.04.005>, 2006.
- Ratigan, J. L.: The use of the fracture reopening pressure in hydraulic fracturing stress measurements, *Rock Mechanics and Rock Engineering*, 25, 225–236, <https://doi.org/10.1007/BF01041805>, 1992.
- Read, S., Perrin, N., and Richards, L.: Applicability of the Hoek-Brown failure criterion to New Zealand greywacke rocks, in: *ISRM Congress*, pp. ISRM–9CONGRESS, ISRM, 1999.

-
- Reichert, C.: DEKORP – Deutsches kontinentales reflexionsseismisches Programm – Vorgeschichte, Verlauf und Ergebnisse der bisherigen Arbeiten., in: Festschrift zum 60. Geburtstag von Hans-Jürgen Dürbaum, edited by Beisser, M., Bosum, W., and Brüning, H., Geologisches Jahrbuch - Reihe E, pp. 143–165, Schweizerbart Science Publishers, Stuttgart, Germany, 1988.
- Reinhold, K.: Tiefenlage der” Kristallin-Oberfläche” in Deutschland–Abschlussbericht, Tech. rep., Bundesanstalt für Geowissenschaften und Rohstoffe, Hannover, 2005.
- Reinhold, K., Jahn, S., Kühnlenz, T., Ptock, L., and Sönnke, J.: Methodenentwicklung und Anwendung eines Sicherheitsnachweiskonzeptes für einen generischen HAW-Endlagerstandort im Tonstein (AnSichT) Endlagerstandortmodell Nord (AnSichT) - Teil I: Beschreibung des geologischen Endlagerstandortmodells, Tech. rep., Bundesanstalt für Geowissenschaften und Rohstoffe, Hannover, 2013.
- Reiter, K. and Heidbach, O.: 3-D geomechanical-numerical model of the contemporary crustal stress state in the Alberta Basin (Canada), *Solid Earth*, 5, 1123–1149, <https://doi.org/10.5194/se-5-1123-2014>, 2014.
- Reiter, K., Heidbach, O., Reinecker, J., Müller, B., and Röckel, T.: Spannungskarte Deutschland 2015, *Erdöl, Erdgas, Kohle*, 131, 437–442, 2015.
- Reiter, K., Heidbach, O., Müller, B., Reinecker, J., and Röckel, T.: Stress Map Germany, <https://doi.org/10.1029/98EO00426>, 2016.
- Reiter, K., Ahlers, S., Röckel, L., Morawietz, S., Henk, A., Hergert, T., Heidbach, O., Müller, B., and Schilling, F.: SpannEnD — Abschlussbericht, Tech. rep., TU Darmstadt, Darmstadt, 2022.
- Ren, N. and Hudson, P.: Predicting the in-situ of stress using differential wave velocity analysis, in: *US symposium on rock mechanics*. 26, pp. 1235–1244, 1985.
- Ringseis, H., Doppler, G., and Meyer, R. K.: Geologisches 3D-Modell Region Ingolstadt, URL <https://www.3dportal.lfu.bayern.de/>, visited on 04.10.2022, 2020.
- Röckel, L., Ahlers, S., Müller, B., Reiter, K., Heidbach, O., Henk, A., Hergert, T., and Schilling, F.: The analysis of slip tendency of major tectonic faults in Germany, *Solid Earth*, 13, 1087–1105, <https://doi.org/10.5194/se-13-1087-2022>, 2022.
- Rummel, F., Möhring-Erdmann, G., and Baumgärtner, J.: Stress constraints and hydrofracturing stress data for the continental crust, *Pure and Applied Geophysics PAGEOPH*, 124, 875–895, <https://doi.org/10.1007/BF00879616>, 1986.
- Rupf, I. and Nitsch, E.: Das Geologische Landesmodell von Baden-Württemberg: Datengrundlagen, technische Umsetzung und erste geologische Ergebnisse, *LGRB-Informationen*, 21, 2008.
- Rutqvist, J., Tsang, C.-F., and Stephansson, O.: Uncertainty in the maximum principal stress estimated from hydraulic fracturing measurements due to the presence of the induced fracture, *International Journal of Rock Mechanics and Mining Sciences*, 37, 107–120, [https://doi.org/10.1016/S1365-1609\(99\)00097-0](https://doi.org/10.1016/S1365-1609(99)00097-0), 2000.

-
- Sanei, M., Rahmati, A., Faramarzi, L., Goli, S., and Mehinrad, A.: Estimation of rock mass deformation modulus in Bakhtiary Dam Project in Iran, in: ISRM SINOROCK, pp. ISRM–SINOROCK, ISRM, 2013.
- Savage, W., Swolfs, H., and Powers, P.: Gravitational stresses in long symmetric ridges and valleys, in: International Journal of Rock Mechanics and Mining Sciences & Geomechanics Abstracts, no. 5 in 22, pp. 291–302, Elsevier, 1985.
- Scheidegger, A. E.: Stress in Earth's crust as determined from hydraulic fracturing data, *Geologie und Bauwesen*, 27, 45–53, 1962.
- Schintgen, T. V.: The Geothermal Potential of Luxembourg : Geological and thermal exploration for deep geothermal reservoirs in Luxembourg and the surroundings, Ph. d. thesis, Universität Potsdam, Potsdam, 2015.
- Schmitt, D. R. and Haimson, B.: Rock Mechanics and Engineering Volume 1, CRC Press, <https://doi.org/10.1201/9781315364261>, 2017.
- Schmitt, D. R. and Zoback, M. D.: Poroelastic effects in the determination of the maximum horizontal principal stress in hydraulic fracturing tests—A proposed breakdown equation employing a modified effective stress relation for tensile failure, *International Journal of Rock Mechanics and Mining Sciences & Geomechanics Abstracts*, 26, 499–506, [https://doi.org/10.1016/0148-9062\(89\)91427-7](https://doi.org/10.1016/0148-9062(89)91427-7), 1989.
- Schmitt, D. R., Currie, C. A., and Zhang, L.: Crustal stress determination from boreholes and rock cores: Fundamental principles, *Tectonophysics*, 580, 1–26, <https://doi.org/10.1016/j.tecto.2012.08.029>, 2012.
- Schoenball, M. and Davatzes, N. C.: Quantifying the heterogeneity of the tectonic stress field using borehole data, *Journal of Geophysical Research: Solid Earth*, 122, 6737–6756, <https://doi.org/10.1002/2017JB014370>, 2017.
- Schoenball, M., Walsh, F. R., Weingarten, M., and Ellsworth, W. L.: How faults wake up: The Guthrie-Langston, Oklahoma earthquakes, *Leading Edge*, 37, 100–106, <https://doi.org/10.1190/tle37020100.1>, 2018.
- Shen, B.: Borehole breakouts and in situ stresses, in: SHIRMS 2008: Proceedings of the First Southern Hemisphere International Rock Mechanics Symposium, pp. 407–418, Australian Centre for Geomechanics, 2008.
- Shen, J., Karakus, M., and Xu, C.: A comparative study for empirical equations in estimating deformation modulus of rock masses, *Tunnelling and Underground Space Technology*, 32, 245–250, 2012.
- Sibson, R. H.: Frictional constraints on thrust, wrench and normal faults, *Nature*, 249, 542–544, <https://doi.org/10.1038/249542a0>, 1974.

-
- Sjöberg, J. and Klasson, H.: Stress measurements in deep boreholes using the Borre (SSPB) probe, *International Journal of Rock Mechanics and Mining Sciences*, 40, 1205–1223, 2003.
- Sjöberg, J., Christiansson, R., and Hudson, J. A.: ISRM suggested methods for rock stress estimation-part 2: Overcoring methods, *International Journal of Rock Mechanics and Mining Sciences*, 40, 999–1010, <https://doi.org/10.1016/j.ijrmms.2003.07.012>, 2003.
- SLULG: Sächsisches Landesamt für Umwelt, Landwirtschaft und Geologie – Geologisches 3D Modell der Elbtalzone, URL <http://lsnq.de/3delbezone>, visited on 10.08.2022, 2012.
- Sommaruga, A.: Décollement tectonics in the Jura forelandfold-and-thrust belt, *Marine and Petroleum Geology*, 16, 111–134, [https://doi.org/10.1016/S0264-8172\(98\)00068-3](https://doi.org/10.1016/S0264-8172(98)00068-3), 1999.
- Sonmez, H., Gokceoglu, C., and Ulusay, R.: Indirect determination of the modulus of deformation of rock masses based on the GSI system, *International Journal of Rock Mechanics and Mining Sciences*, 41, 849–857, 2004.
- Sonmez, H., Gokceoglu, C., Nefeslioglu, H., and Kayabasi, A.: Estimation of rock modulus: for intact rocks with an artificial neural network and for rock masses with a new empirical equation, *International Journal of Rock Mechanics and Mining Sciences*, 43, 224–235, 2006.
- Stephansson, O.: Rock stress measurement by sleeve fracturing, 5th ISRM Congress, p. 9, 1983.
- Strickland, F. and Ren, N.-K.: Use of differential strain curve analysis in predicting in-situ stress state for deep wells, in: *ARMA US Rock Mechanics/Geomechanics Symposium*, pp. ARMA–80, ARMA, 1980.
- Swisstopo: GeoMol Geological Model 2019, URL <https://viewer.swissgeol.ch>, visited on 08.09.2023, 2019.
- Tašárová, Z. A., Fullea, J., Bielik, M., and Šroda, P.: Lithospheric structure of Central Europe: Puzzle pieces from Pannonian Basin to Trans-European Suture Zone resolved by geophysical-petrological modeling, *Tectonics*, 35, 722–753, <https://doi.org/10.1002/2015TC003935>, 2016.
- Teufel, L.: Determination of in-situ stress from anelastic strain recovery measurements of oriented core, in: *SPE Rocky Mountain Petroleum Technology Conference/Low-Permeability Reservoirs Symposium*, pp. SPE–11 649, SPE, 1983.
- Teufel, L. W. and Warpinski, N. R.: Determination Of In Situ Stress From An Elastic Strain Recovery Measurements Of Oriented Core: Comparison To Hydraulic Fracture Stress Measurements In The Rollins Sandstone, Piceance Basin, Colorado, in: *ARMA US Rock Mechanics/Geomechanics Symposium*, pp. ARMA–84, ARMA, 1984.
- TLUBN: Thüringer Landesamt für Umwelt Bergbau und Naturschutz – Geologisches 3D-Modell „Thüringer Becken“, URL <https://viewer.bge.de/webgui/gui2.php?moma=Thueringen.INFLUINS>, visited on 29.07.2022, 2014.
- TNO: Pressure Southern North Sea (PSNS) database, URL <https://www.nlog.nl/pressure-southern-north-sea-psns-database>, visited on 28.09.2023, 2014.

-
- Unger, G. and Rommel, A.: Geologisches 3D Modell der Sächsisch-Tschechischen Grenzregion (Projekt ResiBil), Tech. rep., Sächsisches Landesamt für Umwelt, Landwirtschaft und Geologie, 2020.
- Unger, G. and Thiele, L.: Geologisches 3D Modell Neubaustrecke Dresden-Prag 2020, Tech. rep., Sächsisches Landesamt für Umwelt, Landwirtschaft und Geologie, 2020.
- Ustaszewski, K. M.: Reactivation of pre-existing crustal discontinuities: the southern Upper Rhine Graben and the northern Jura Mountains : a natural laboratory, Dissertation, University of Basel, <https://doi.org/10.5451/unibas-003789512>, 2004.
- Valasek, P. and Mueller, S.: A 3D tectonic model of the Central Alps based on an integrated interpretation of seismic refraction and NRP 20 reflection data, in: Deep structure of the Swiss alps: results of NRP 20, edited by Pfiffner, O. A., Lehner, P., Heitzmann, P., Mueller, S., and Steck, A., pp. 302–325, Birkhauser Verlag, Basel, 1997.
- Valley, B. and Evans, K. F.: Stress state at Soultz to 5 km depth from wellbore failure and hydraulic observations, Proceedings EHDRA Scientific Conference, Soultz, 15, 15, 2007.
- Valley, B. and Evans, K. F.: Stress magnitudes in the Basel enhanced geothermal system, International Journal of Rock Mechanics and Mining Sciences, 118, 1–20, 2019.
- Vernik, L. and Zoback, M. D.: Estimation of maximum horizontal principal stress magnitude from stress-induced well bore breakouts in the Cajon Pass Scientific Research borehole, Journal of Geophysical Research, 97, 5109–5119, <https://doi.org/10.1029/91JB01673>, 1992.
- Wagner, M., Kissling, E., and Husen, S.: Combining controlled-source seismology and local earthquake tomography to derive a 3-D crustal model of the western Alpine region, Geophysical Journal International, 191, 789–802, <https://doi.org/10.1111/j.1365-246X.2012.05655.x>, 2012.
- Wang, H. and Sharma, M. M.: New variable compliance method for estimating in-situ stress and leak-off from DFIT data, in: SPE Annual Technical Conference and Exhibition, p. D011S006R008, SPE, 2017.
- Warpinski, N. R. and Teufel, L. W.: In situ stress measurements at Rainier Mesa, Nevada test site-Influence of topography and lithology on the stress state in tuff, International Journal of Rock Mechanics and Mining Sciences and, 28, 143–161, [https://doi.org/10.1016/0148-9062\(91\)92163-S](https://doi.org/10.1016/0148-9062(91)92163-S), 1991.
- Warren, W. E. and Smith, C. W.: In situ stress estimates from hydraulic fracturing and direct observation of crack orientation, Journal of Geophysical Research, 90, 6829, <https://doi.org/10.1029/jb090ib08p06829>, 1985.
- White, A. J., Traugott, M. O., and Swarbrick, R. E.: The use of leak-off tests as means of predicting minimum in-situ stress, Petroleum Geoscience, 8, 189–193, <https://doi.org/10.1144/petgeo.8.2.189>, 2002.

-
- Widarsono, B., Marsden, J., and King, M.: In situ stress prediction using differential strain analysis and ultrasonic shear-wave splitting, Geological Society, London, Special Publications, 136, 185–195, 1998.
- Wygrala, B. P.: Integrated study of an oil field in the southern Po basin, northern Italy, Ph.D. thesis, University of Cologne, 1989.
- Yamamoto, K., Kuwahara, Y., Kato, N., and Hirasawa, T.: Deformation rate analysis: A new method for in situ stress estimation from inelastic deformation of rock samples under uni-axial compressions, Tohoku Geophysical Journal, 33, 127–47, 1990.
- Zang, A. and Stephansson, O.: Stress Field of the Earth's Crust, Springer Netherlands, Dordrecht, <https://doi.org/10.1007/978-1-4020-8444-7>, 2010.
- Zhang, L. and Einstein, H.: Using RQD to estimate the deformation modulus of rock masses, International Journal of Rock Mechanics and Mining Sciences, 41, 337–341, 2004.
- Zhang, X., Jeffrey, R. G., Bunger, A. P., and Thiercelin, M.: Initiation and growth of a hydraulic fracture from a circular wellbore, International Journal of Rock Mechanics and Mining Sciences, 48, 984–995, <https://doi.org/10.1016/j.ijrmms.2011.06.005>, 2011.
- Ziegler, M. O. and Heidbach, O.: The 3D stress state from geomechanical–numerical modelling and its uncertainties: a case study in the Bavarian Molasse Basin, Geothermal Energy, 8, <https://doi.org/10.1186/s40517-020-00162-z>, 2020.
- Ziegler, M. O. and Heidbach, O.: Manual of the Matlab Script FAST Calibration v2.0, <https://doi.org/10.48440/wsm.2021.002>, 2021.
- Ziegler, M. O., Heidbach, O., Reinecker, J., Przybycin, A. M., and Scheck-Wenderoth, M.: A multi-stage 3-D stress field modelling approach exemplified in the Bavarian Molasse Basin, Solid Earth, 7, 1365–1382, <https://doi.org/10.5194/se-7-1365-2016>, 2016.
- Ziegler, M. O., Ziebarth, M., and Reiter, K.: Manual of the Python Script Apple PY v1.3, Tech. rep., GFZ Data Service, <https://doi.org/10.5880/wsm.2020.002>, 2020.
- Zoback, M. D.: Reservoir geomechanics, Cambridge University Press, <https://doi.org/10.1017/CBO9780511586477>, 2007.
- Zoback, M. D., Barton, C. A., Brudy, M., Castillo, D. A., Finkbeiner, T., Grollimund, B. R., Moos, D. B., Peska, P., Ward, C. D., and Wiprut, D. J.: Determination of stress orientation and magnitude in deep wells, International Journal of Rock Mechanics and Mining Sciences, 40, 1049–1076, <https://doi.org/10.1016/j.ijrmms.2003.07.001>, 2003.
-

List of Figures

2.1	Definition of the stress tensor and the tectonic stress regime.	4
2.2	Stress magnitude indicators.	5
2.3	Hydraulic pressure curves.	6
2.5	Principle of the overcoring method	13
2.6	General workflow of 3-D geomechanical-numerical modelling	19
2.7	Overview of 3-D geological models implemented in the new geomechanical model .	20
2.8	Data used for construction of the top of the crystalline basement	21
2.9	Sketch: Definition of four units by three formation interfaces	22
2.10	Concept of a 'point cloud model'	23
2.11	Map of available faults of Germany	25
2.12	Workflow of geometry transfer	28
2.13	Fault Map of Germany displaying the subregions	29
2.14	Slip tendency analysis of the Upper Rhine Valley	30
2.15	Slip tendency analysis of the North German Basin	31
2.16	Slip tendency analysis of Saxony and the Ore Mountains	32
2.17	Slip tendency analysis of the Molasse Basin	33
2.18	Stereoplots of slip tendency for different depths	34
3.1	Sketch on root model, branch model and the competing calibration approaches . .	38
3.2	Comparison of vertical stress profiles	39
3.3	Sketch showing a two-step approach to model absolute stresses	41
3.4	Depth profiles of final stress matching the calibration data at 5 km depth	42
3.5	Depth of calibration data	43
3.6	Depth-dependent boundary conditions for four different initial stresses	44
3.7	Comparison between Young's modulus of intact rock from laboratory measurements	47
3.8	Schematic representation a DFN modelling work flow	48
3.9	DFN modelling of a granite outcrop	49
3.10	Schematic representation of a lattice-spring synthetic rock mass (LS-SRM) model .	50
3.11	Extent and definition of the siting region 001	53
3.12	Map of south-western Germany with sub-area 001 and existing models	54
3.13	Map of south-western German with geological units and stress data	54
3.14	Map of the sub-area 001 and the 3-D model geometry	55
3.15	Reconstruction of the basin immersion for sub-area 001	56
3.16	Plot of used thermal and mechanical properties with stress prediction	56
3.17	Extent and definition of the siting region 009	59
3.18	Extent of the regional scale geomechanical model of the siting area 009	60
3.19	Model geometry for investigation region 009	60
3.20	Discretised area around the KTB region	61
3.21	Preliminary stress orientation derived from the geomechanical model	62
3.22	Preliminary Regime Stress Ratio derived from the geomechanical model	63

4.1	Basic workflow of the tool FAST Calibration	65
4.2	Four different ways to assess the reliability of a stress state	67
4.3	Workflow of the FAST Calibration multistage branch calibration	68

List of Tables

2.1	Planned model dimensions.	24
2.2	List of available geological models	26
3.1	Used Parameter for the thermal model sub-area 001	57
3.2	Rock properties of the units used for region 009	63